Application of advanced seismic techniques for archaeological investigations

Liu, J.

DOI
10.4233/uuid:9d70c96d-7a7e-4b8d-98d6-d7b0ffaf6812

Publication date
2022

Document Version
Final published version

Citation (APA)
Liu, J. (2022). *Application of advanced seismic techniques for archaeological investigations*. [Dissertation (TU Delft), Delft University of Technology]. https://doi.org/10.4233/uuid:9d70c96d-7a7e-4b8d-98d6-d7b0ffaf6812

Application of advanced seismic techniques for archaeological investigations

$$\rho\partial_t^2 u_i = f_i + \partial_j \sigma_{ij}$$

Jianhuan Liu

APPLICATION OF ADVANCED SEISMIC TECHNIQUES FOR ARCHAEOLOGICAL INVESTIGATIONS

APPLICATION OF ADVANCED SEISMIC TECHNIQUES FOR ARCHAEOLOGICAL INVESTIGATIONS

Dissertation

for the purpose of obtaining the degree of doctor
at Delft University of Technology,
by the authority of Rector Magnificus Prof. dr. ir. T.H.J.J. van der Hagen,
chair of the Board of Doctorates,
to be defended publicly on
Thursday 23 June 2022 at 10.00 hours

by

Jianhuan LIU

Master of Science in Solid Geophysics,
University of Chinese Academy of Sciences, Beijing, China,
Born in Jiangxi, China.

This dissertation has been approved by the

Promotor: Dr. R. Ghose
Promotor: Dr. ir. D. S. Draganov

Composition of the doctoral committee:

Rector Magnificus	Chairman
Dr. R. Ghose	Delft University of Technology
Dr. ir. D. S. Draganov	Delft University of Technology
Independent members:	
Prof. dr. ir. C. P. A. Wapenaar	Delft University of Technology
Prof. dr. rer. nat. W. Rabbel	University of Kiel, Germany
Prof. dr. L. G. Evers	Delft University of Technology
Dr. ir. D. J. Verschuur	Delft University of Technology
Prof. dr. W. A. Mulder	Delft University of Technology, reserve member
Other member:	
Dr. Q. P. J. Bourgeois	Leiden University

The work presented in this thesis was conducted at Delft University of Technology, Delft, The Netherlands. The research was mainly funded by TU Delft and the China Scholarship Council (CSC) (file no. 201604910851).

ISBN 978-94-6423-855-6

Published by: Uitgeverij BOX Press, Oisterwijk, The Netherlands
Printed by: Proefschriftmaken.nl

An electronic version of this dissertation is available at
http://repository.tudelft.nl/.

To my father and mother.

CONTENTS

SUMMARY

At different places in the world, the local climate conditions have helped the preservation of archaeological sites to a very high degree. This has helped us understand better our history. This situation, however, is quickly changing due to the climate change we are now facing. The condition at an increasing number of ancient sites around the world is now deteriorating due to the warming climate. Obtaining high-resolution images of the subsurface of the archaeological sites without excavation can help us make better strategies for conserving these sites. Such possibilities are provided by the application of geophysical exploration methods.

Among all available geophysical approaches, high-resolution reflection seismic using transverse (S-) waves is one of the few options that can provide detailed information regarding the subsurface structure beneath archaeological sites for depths up to several meters. However, most unexcavated sites are covered by soil. Near-surface seismic data acquired in such soil-covered sites are dominated by source-generated, dispersive surface waves, and sometimes surface waves caused by other anthropogenic sources, e.g., traffic and human activities in the vicinity of the seismic line. Both of these strong events can camouflage the very shallow reflections. The conventional techniques for suppression of surface waves, e.g., muting or spatial filtering, are ineffective or even detrimental to the target reflections, especially at near offsets. This is especially challenging in surveys where the available source-receiver offset range is often quite limited, and the velocity and frequency content of the surface waves largely overlap with those of the target S-wave reflections. In chapter 2, we aim to develop a data-driven way to suppress surface-wave noise and thus reveal the very shallow reflections. We make use of seismic interferometry (SI) to retrieve both source-coherent and source-incoherent surface-wave parts of the data. The retrieved surface waves are then adaptively subtracted (AS) from the recorded data, thereby exposing the hidden reflections. We apply our schemes to both synthetic and field seismic data. We show that artifacts caused by stacking surface-wave noise are greatly reduced and that reflectors, especially at very shallow depth, can be much better imaged and interpreted.

The dominance of surface waves also make it impossible to identify weak diffraction signals, which is the seismic response of buried objects of small size. The diffraction events can be used to detect and locate the distribution of shallow objects. Revealing the hidden diffraction signals from under the dominant surface waves and using them for locating objects constitute another goal of this thesis. In chapters 3 and 4, we introduce an interferometric workflow for imaging subsurface objects using masked diffractions. This workflow includes three main steps. We first reveal masked diffractions by suppression of the dominant surface waves through a combination of SI and nonstationary AS. The revealed weak diffraction signal is then enhanced by crosscoherence-based supervirtual interferometry (SVI). Finally, we produce a diffraction image by a multipath summation approach, which can be used to interpret the locations of subsurface diffractors.

We apply our method to field data acquired at an archaeological site using two different active sources. Two shallow anomalies were detected in our sections, whose locations agree well with burial burnt stones. These burnt stones have also been detected in an independent magnetic survey and in corings. The limitation of our workflow is that it can only be applied with desired resolution to S-wave data when seismic sources and receivers polarized in the cross-line direction.

In the first part of this thesis (chapter 2 ~ chapter 4), we mainly focus on extracting signals (reflections and diffractions) from under dominant surface waves, and then use them for imaging structures of our interests. However, the surface waves travel along the surface of the Earth, so they sample the shallow part of the subsurface. Thus, surface waves can be used to constrain the subsurface structures at shallow depths. In the second part of this thesis (chapter 5 ~ chapter 6), we mainly focus on how to use surface waves for obtaining high-resolution images of the shallow subsurface.

We make use of 2D elastic full-waveform inversion (FWI) to deduce the velocity structures from shallow seismic data dominated by surface waves. The challenge that limits the potential application of FWI in the context of near-surface experiments is the notorious cycle-skipping problem. Besides, recorded wavefields are often characterized by amplitude errors due to coupling variation at different source and receiver positions. The phase information of the recordings contains the kinematic information of the wavefields, and thus has a great potential to tackle the above-mentioned challenges. In chapter 5, we propose an amplitude-unbiased coherency measure as a misfit function that can be incorporated into FWI. We give the details on how to calculate efficiently the gradient of this new misfit function using the adjoint-state method. The benefit of this new misfit function is that it can extract information uniformly over seismic signals (surface waves, reflections, and diffractions), and that it is robust for field-data application of FWI. We apply the new FWI approach to a field dataset recorded at an archaeological site located in Ostia, Italy. A known tumulus is identified in our FWI results. Our results also establish that the shallow subsurface under the survey lines is quite heterogeneous.

In this thesis, the field data were acquired along 2D seismic lines. For a 2D seismic survey, seismic incoherent noise and events scattered from out-of-plane objects may lead to additional artifacts in the inverted results from FWI. To tackle this problem, in chapter 6, we aim to develop a complete workflow that can determine subsurface S-wave velocity (V_S) models inverted from 2D near-surface seismic data in a more stable way. We make use of a combination of SVI and matching filters to accurately retrieve the dominant surface waves from the inline direction, while the incoherent noise and 3D scattering events get significantly suppressed. The subsurface structures obtained from inverting the retrieved data can be interpreted together with the sections resulting from FWI of the original data, with the aim to mitigate the potential misinterpretation of artifacts. With initial models provided by multichannel analysis of surface waves (MASW), our results demonstrate that it is possible to accurately invert high-resolution S-wave velocity structures from shallow seismic data, even when the data quality is partly compensated by strong noise and presence of 3D seismic events scattered by objects located in the crossline direction.

The technologies that we develop and implement in this research have been successfully tested at three archaeological sites, addressing different goals.

SAMENVATTING

Op verschillende plekken in de wereld heeft het lokale klimaat ertoe bijgedragen dat archeologische vindplaatsen zeer goed bewaard zijn gebleven. Het onderzoeken van deze vindplaatsen heeft ons geholpen om een beter begrip te krijgen van onze geschiedenis. De situatie is echter snel aan het veranderen door de huidige trend van klimaatverandering. Door een warmer klimaat verslechtert de toestand van historische plekken. Het verkrijgen van beelden van de ondergrond met hoge resolutie op archeologische plaatsen kan ons helpen betere strategieën te ontwikkelen om deze te conserveren. Deze beelden van de ondergrond worden geleverd door geofysische onderzoeksmethodes.

Van alle beschikbare geofysische methodes is hogeresolutiereflectieseismiek, gebruikmakend van transversale of S-golven, één van de weinige opties die gedetailleerde informatie, tot een aantal meters diepte, geeft over de ondergrondse structuur onder archeologische vindplaatsen. De meeste niet-opgegraven plaatsen zijn bedekt met aarde. Seismische gegevens nabij het oppervlak worden gedomineerd door dispersieve oppervlaktegolven, gegenereerd door aktieve bronnen en soms door andere antropogene bronnen, bijv. verkeer en menselijke activiteit in de nabijheid van de seismische lijn. Beide effecten zijn sterk en kunnen zeer ondiepe reflecties camoufleren. De conventionele technieken om deze oppervlaktegolven te onderdrukken, bijv. door ze te dempen of ruimtelijke filters toe te passen, zijn niet effectief en kunnen ook de beoogde reflecties onderdrukken, in het bijzonder bij kleinere meetafstanden. Dit is vooral een uitdaging in onderzoeksprojecten waar de afstand tussen bron en ontvanger erg beperkt is, en de snelheid en frequentieinhoud van de oppervlaktegolven grotendeels overeenkomen met die van de beoogde S-golfreflecties. In hoofdstuk 2 hebben wij een datagedreven methode ontwikkeld die ruis van oppervlaktegolven onderdrukt en zo de zeer ondiepe reflecties zichtbaar maakt. We maken gebruik van seismische interferometrie (SI) om zowel de broncoherente als bronincoherente oppervlaktegolven in de data te verkrijgen. Deze oppervlaktegolven worden dan adaptief afgetrokken (adaptive subtraction, AS) van de opgenomen data, waardoor de verborgen reflecties zichtbaar worden. We passen on schema toe op zowel synthetische als in het veld opgenomen seismische data. We laten zien dat artefacten, veroorzaakt door de invloed van oppervlaktegolven, sterk verminderd worden en dat met name ondiepe reflectoren veel beter in beeld gebracht en geïnterpreteerd kunnen worden.

De dominantie van oppervlaktegolven maakt het ook onmogelijk om zwakke diffractiesignalen die de seismische signatuur van kleine, begraven objecten vertonen, te identificeren. Deze diffracties kunnen gebruikt worden om ondiepe voorwerpen te detecteren en lokaliseren. Een tweede doel van dit proefschrift behelst het tevoorschijn halen van verborgen diffractiesignalen vanuit de dominante oppervlaktegolven en het gebruiken van dit signaal om objecten te lokaliseren. In hoofstukken 3 en 4 introduceren we een interferometrische methode om ondergrondse objecten in beeld te brengen, gebruikmakend van de verscholen diffracties. Deze methode omvat drie hoofdstappen. Eerste

maken we de verborgen diffracties zichtbaar door de dominante oppervlaktegolven te onderdrukken via een combinatie van SI en niet-stationaire AS. Het zichtbaar gemaakte, zwakke diffractiesignaal wordt dan versterkt door super-virtuele interferometrie (SVI) gebaseerd op kruiscoherentie. Tot slot produceren we een diffractiebeeld door middel van multipadsommatie. Dit beeld kan gebruikt worden om de locatie van ondergrondse diffractoren te interpreteren. We passen onze methode toe op velddata, verkregen op een archeologische vindplaats met behulp van twee verschillende actieve bronnen. In onze dwarsdoorsnedes van de ondergrond werden twee ondiepe afwijkingen gedetecteerd waarvan de locaties goed overeenkomen met die van verbrande grafstenen. Deze verbrande stenen zijn ook gedetecteerd in een onafhankelijk magnetisch onderzoek en in boringen. De beperking van onze methode is dat deze alleen met de gewenste resolutie toegepast kan worden op S-golfdata als de seismische bronnen en ontvanger gepolariseerd zijn in de richting loodrecht op de lijn.

In het eerste deel van dit proefschrift (hoofdstuk 2–4), concentreren we ons voornamelijk op het bepalen van signaal (reflecties en diffracties) vanuit dominante oppervlaktegolven. We gebruiken dan dit signaal om de door ons gezochte structuren in beeld te brengen. Oppervlaktegolven reizen nabij het oppervlak van de aarde, waarmee ze informatie van de ondiepe delen van de ondergrond bevatten. Dus kunnen oppervlaktegolven gebruikt worden om ondiepe ondergrondse structuren te bepalen. In het tweede deel van dit proefschrift (hoofdstuk 5–6) houden we ons voornamelijk bezig met hoe we oppervlaktegolven kunnen gebruiken om een scherp beeld van de ondiepe ondergrond te krijgen.

We maken gebruik van 2D elastische inversie van de volledige golf (full-waveform inversion, FWI) om de snelheidsstructuren van ondiepe seismische data, gedomineerd door oppervlaktegolven, af te leiden. Een probleem dat de mogelijke toepassing van FWI in de weg staat bij experimenten aan het nabije oppervlakt, is het beruchte probleem van misindentificatie van golfvormen (cycle-skipping). Daarnaast hebben de opgenomen golfvelden vaak last van fouten in de amplitudes, veroorzaakt door plaatselijke verschillen in de koppeling van bronnen en ontvangers met de ondergrond. De fase-informatie van de opnames bevat de kinetische informatie van de golfvelden en heeft dus een groot potentieel om bovenstaand probleem aan te pakken. In hoofdstuk 5 stellen we een coherentiemaat voor als foutenfunctie die ongevoelig is voor amplitudes en die meegenomen kan worden bij FWI. We beschrijven in detail hoe de gradiënt van de nieuwe afwijkfunctie efficiënt berekend kan worden met de adjoint-state methode. Het voordeel van deze nieuwe foutenfunctie is dat hij op uniforme wijze informatie uit seismische signalen kan halen (oppervlaktegolven, reflecties en diffracties), en dat hij robuust is bij toepassingen van FWI op velddata. We passen de nieuwe FWI methode toe op een velddataset, opgenomen op een archeologische vindplaats in Ostia, Italië. In onze FWI resultaten is een bekende grafheuvel geïdentificeerd. Onze resultaten laten ook zien dat de ondiepe ondergrond onder de lijnen relatief heterogeen is.

In dit proefschrift werden de velddata verkregen langs 2D seismische lijnen. Voor een 2D seismisch onderzoek kan incoherente seismische ruis en verstrooid signaal van objecten buiten het vertikale vlak van de lijn, leiden tot additionele artefacten in de inversieresultaten van FWI. Om dit probleem aan te pakken, trachten we in hoofdstuk 6 een complete stabiele methode te ontwikkelen, die een model van de ondergrondse S-

golfsnelheid (V_S) kan bepalen door inversie van 2D seismische data nabij het oppervlak. We maken gebruik van een combinatie van SVI en coherentiefilters om de dominante oppervlaktegolf in de parallelle lijn nauwkeurig te reconstrueren, terwijl de incoherente ruis en de 3D verstrooiingen significant worden onderdrukt. De ondergrondse structuren, verkregen uit de inversie van de gemeten data, kan tegelijk geïnterpreteerd worden met de secties verkregen met behulp van FWI toegepast op de originele data, met het doel om een mogelijke foute interpretatie door artefacten te verkleinen. Met initiële modellen verkregen door meerkanaalsanalyse van oppervlaktegolven (multichannel analysis of surface waves, MASW), laten onze resultaten zien dat het mogelijk is om snelheidsstructuren voor S-golven met hoge resolutie nauwkeurig te bepalen door inversie van ondiepe seismische data, zelfs wanneer de datakwaliteit deels te lijden heeft onder sterke ruis en de aanwezigheid van 3D seismische verstrooiing van objecten liggend in de richting loodrect op de lijn.

De technologieën die we ontworpen en geïmplementeerd hebben in dit onderzoek, zijn met succes uitgeprobeerd op drie verschillende archeologische vindplaatsen, waarbij aan de verschillende doelstellingen werd beantwoord.

LIST OF ACRONYMS

In this thesis, we use a series of acronyms to simplify the description of the text. The full names of each acronym are listed below:

Acronyms	Full names
AGC	Automatic gain control
AS	Adaptive subtraction
CMP	Common midpoint
C-PML	Convolutional perfectly matched layers
CVS	Constant velocity stack
D-section	Diffraction-point-section
ERT	Electrical resistivity tomography
FD	Finite-difference
$f-k$	Frequency-wavenumber
FWI	Full-waveform inversion
GF	Green's function
GPR	Ground-penetrating radar
LMON	Linear moveout noises
MASW	Multichannel analysis of surface waves
NAP	*Normaal Amsterdams Peil*
PWS	Phase-weighted stacking
SI	Seisimc interferometry
S/N	Signal-to-noise ratio
SVD	Singular value decomposition
SVI	Super-virtual interferometry
SWs	Surface waves

1

INTRODUCTION

1.1. BACKGROUND OF GEOPHYSICAL METHODS FOR ARCHAEOLOGICAL INVESTIGATIONS

Geophysical methods can provide non-invasive ways to see underneath the archaeological sites, much like medical imaging can let us see inside the human body. By using certain types of instruments, geophysical methods records physical fields related to the Earth and then uses this information to infer the details of structures in the subsurface. Well-established geophysical methods have been employed in the past for archaeological site investigation, like magnetic surveys, electrical resistivity tomography (ERT), ground-penetrating radar (GPR), and seismic methods. The basic principles of these methods are described in the following.

1.1.1. MAGNETIC METHOD

The Earth is wrapped in a magnetic field, which is mainly caused by outer core convection and solar storms. Every kind of subsurface material has unique magnetic properties, even those that we do not think of as being "magnetic". Many archaeological objects (e.g., iron, steel, burnt stone, pottery) show distinctive magnetic properties than those of the surroundings due to the effects of additional induced and/or remanent magnetization [Sternberg, 1987]. The magnetic method (Figure 1.1) is sensitive to these magnetic susceptibility contrasts and thus can be used to detect these potential objects efficiently. One of the first successful applications of the magnetic survey for archaeological prospecting was reported in the late 1950s [Wynn, 1986]. Later, it was used to detect archaeological remains such as pottery [Gibson, 1986], ancient harbour structures [Boyce et al., 2004] and burnt stone [Lambers et al., 2017]. However, for objects of interest with low magnetic strength, their magnetic field will be probably obscured by that of highly magnetic surrounding materials and thus they become undetectable.

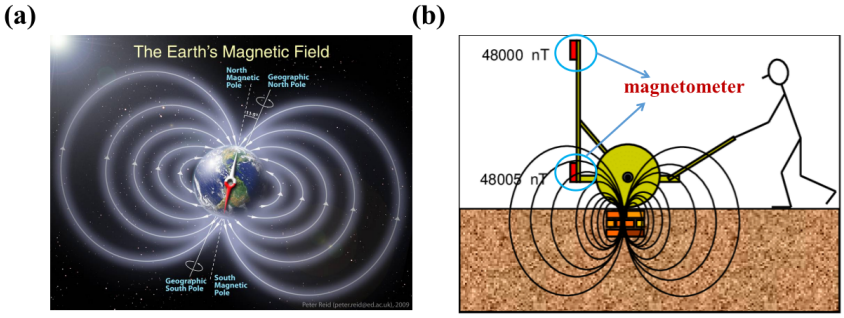

Figure 1.1: (a) Schematic illustration of the invisible magnetic field surrounded by the Earth, which is represented as a dipole magnet field. Due to the solar wind, the magnetic shield is squeezed in closer to Earth on the Sun-facing side and extremely elongated on the night-side [Peter, 2017]. (b) A sketch of a magnetic survey using a gradiometer array with an upper and a lower magnetometer (indicated by blue circles) mounted on a cart. Both sensors measure the Earth's magnetic field, but only the lower sensor is affected by the magnetic anomaly, caused by "magnetic" objects (e.g., burnt stone) in the ground. By computing the gradient (difference) between the values measured at the upper and lower sensors, the very weak magnetic anomaly in the subsurface can be detected (modified from [Trinks and Karlsson, 2007]).

1.1.2. ERT METHOD

ERT (Figure 1.2) is also widely used in the investigation and detection of shallow targets in archaeological sites. With ERT, an electric current, generated by man-made electrical sources, is injected in the subsurface, where the current interacts with subsurface structures to create potential differences. The potential difference is measured at the surface with electrodes inserted into the ground. Using the recordings of the potential difference and the injected current, local electrical apparent resistivity is calculated. Archaeological features can be mapped when they have distinct resistivity compared to their surroundings. The ERT has been successfully applied to map, e.g., ancient walls in the underground [Dogan and Papamarinopoulos, 2003]. However, most of the Earth materials have a range of resistivities similar to each other, which makes unambiguous interpretation difficult.

1.1.3. GPR METHOD

Contrary to the above-mentioned methods, which show only limited subsurface resolution, GPR (Figure 1.3) is a non-invasive geophysical method that can provide high-resolution images of shallow targets based on changes in the electromagnetic properties [Bailey et al., 1964]. Similar to the well-known concept of radar, GPR sends "radar" signal (high-frequency electromagnetic pulse) into the ground. Subsurface structures and objects with certain electromagnetic contrasts will cause reflection and/or diffraction of signals that can be picked up by a receiver antennae. The subsurface targets of interest can then be detected, localized, and characterized after minimal signal processing steps. GPR has been used in archaeological investigations since the 1970s, and its successful examples include historic cellars detection [Vickers and Dolphin, 1975], burial mounds imaging [Goodman and Nishimura, 1993], buried walls location [Ngan-Tillard et al., 2020], etc. However, the penetration depth of GPR signals is severely limited in a

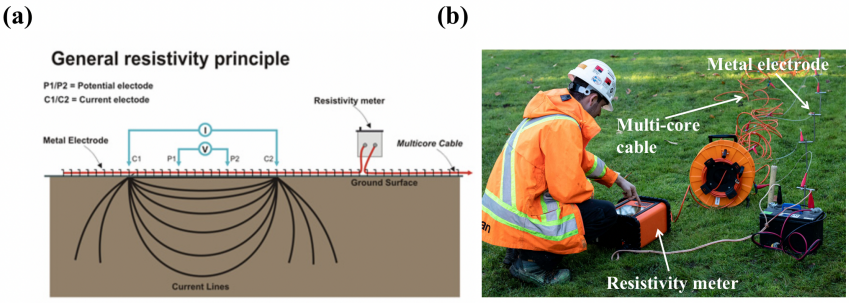

Figure 1.2: (a) Illustration of the principle of the ERT method. The acquisition of ERT data involves the injection of current into the ground via a pair of electrodes. The resulting potential field is then measured by a corresponding pair of potential electrodes. (b) The field set-up of a typical ERT survey. It consists of the deployment of an array of regularly spaced electrodes, which are connected to a central control unit via multicore cables. Measurements of resistivity are then recorded via complex combinations of current and potential electrode pairs to build up a pseudo cross-section of apparent resistivity beneath the survey line. The depth of investigation depends on the electrode separation and geometry, with greater electrode separations yielding bulk resistivity measurements from greater depths (modified from [GeoScan, 2022; TerraDat, 2022]).

medium with very low electrical resistivity (such as in a electrically conductive, water-saturated subsurface). Thus, GPR is generally not suitable to detect objects below the ground-water level or objects filled with water or objects located in electrically conductive clayey environment.

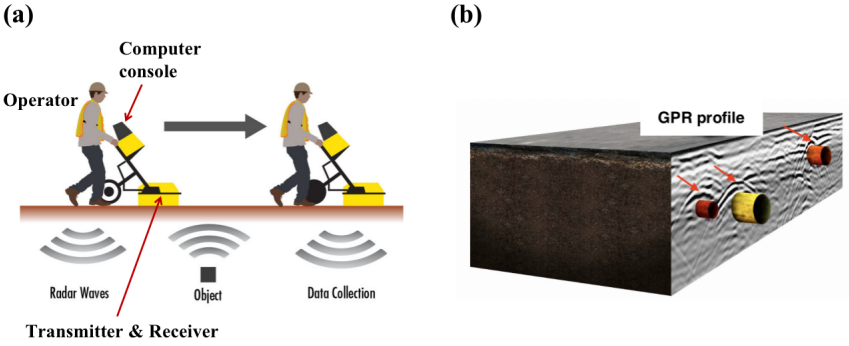

Figure 1.3: (a) Illustration of the principle of the GPR method. The GPR survey is led by an operator while the transmitter antenna emits repetitive short-duration electromagnetic signals into the ground. Electromagnetic waves are then reflected to the receiver when they hit a buried object. The collected traces form a GPR profile (b), which are then processed to detect/locate the location of buried objects (modified from [Angelo, 2016]).

1.1.4. SEISMIC METHODS AND THEIR LIMITATIONS

Seismic methods (Figure 1.4) have also been used in the past for characterizing archaeological sites. The seismic energy is usually excited by active sources (e.g., hammer, vibrator). The seismic wave propagates through the subsurface medium, scattered by sub-

surface heterogeneities, and is then in part recorded by sensors (usually geophones) positioned at the surface. The recorded wavefield includes the seismic response of buried structures and can be used to infer details of the subsurface medium. Body (primarily reflected and refracted) waves and surface waves have been used in the past for imaging the heterogeneities in the near-surface. The high-resolution reflection seismic method has been quite successful over the years in imaging the precise location and geometry of shallow subsurface structures using mainly reflections and/or diffractions (e.g., [Jongerius and Helbig, 1988; Miller and Steeples, 1994; Steeples and Miller, 1988]). One main challenge for the near-surface application of seismic methods, especially using seismic shear waves, is that the useful reflections and diffractions signals are often camouflaged by strong surface waves.

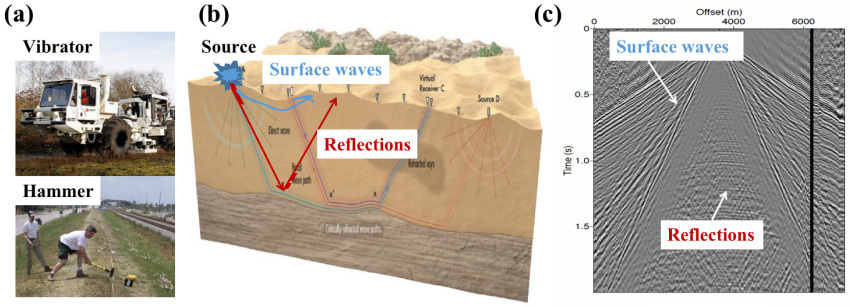

Figure 1.4: Illustration of seismic methods for subsurface imaging. (a) Examples of active sources (e.g., vibrator, hammer) used to excite seismic energy; (b) a cartoon showing the propagation of seismic waves through the subsurface medium (modified from [Li, 2020]). The geophones deployed at the surface record seismic response from the buried structures, which can further be used to infer the structures of the subsurface medium; (c) a typical seismic common-source gather [Dong et al., 2006] acquired during a field survey, where surface waves and body-wave reflections can be identified. These wavetypes can be used to image specific subsurface structures.

Also, powered by the early works done by Lailly [1983] and Tarantola [1984], the full-waveform inversion (FWI) technology has now evolved to be a promising tool that can provide high-resolution images of the subsurface. It can delineate subsurface structures directly from the recorded waveforms by minimizing the difference between measured and synthetic data. However, one challenge in FWI is the notorious cycle-skipping problem [Solano et al., 2014; Virieux and Operto, 2009; Yuan et al., 2015] caused by inaccurate initial models. Besides, the recorded wavefields are often characterized by amplitude errors [Kamei et al., 2015; Maurer et al., 2012] due to different coupling at different source and receiver positions. In 2D seismic surveys, which are common in archaeological prospecting, the recorded wavefield contains also scattered events from the crossline directions [Groos et al., 2017]. In the procedure of FWI, the algorithm tries to mimic these events, and hence it may lead to artificial structures in the resulting models.

1.2. THESIS OBJECTIVE AND OUTLINE

The aim of this thesis is to address the above-mentioned challenges in the application of high-resolution seismic methods in the context of the near-surface application, especially for archaeological site investigations. In the following, the content of the thesis is outlined in a step-by-step manner.

In chapter 2, we concentrate on the possibility of revealing hidden reflection signals from under other dominant seismic events. These dominant events may include source-coherent surface waves and other linear moveout noises (LMON). Our goal is to suppress such surface-wave noise and LMON while preserving shallow reflections, which are of great interest for near-surface imaging. We make use of seismic interferometry (SI) to retrieve source-coherent surface waves and LMON in a data-driven way. This retrieved energy is then adaptively subtracted from the recorded seismic data. Using synthetic data, we show that our scheme is robust in separating shallow reflections from source-coherent surface waves and LMON, even when they share very similar velocity and frequency contents. We apply our schemes to a field dataset characterized by the presence of overwhelming surface waves and LMON. The field data were acquired in Dreumel, located in the central part of the Netherlands. Our results show that the reflectors at a very shallow depth can be imaged, thanks to the significant suppression of the surface waves and LMON by the algorithm we developed.

In chapters 3 and 4, we focus on using masked diffractions for locating/detecting subsurface heterogeneities. The masked diffractions are firstly revealed by a combination of SI and nonstationary adaptive subtraction (AS), and then they are further enhanced through crosscoherence-based super-virtual interferometry (SVI). We compute the final diffraction image by a spatial summation of the revealed diffractions; a phase-weighted stacking (PWS) is introduced to enhance the coherent summation of weak diffraction signals. In the final diffraction image, the locations of the subsurface scatters can be interpreted. We apply our method to field data acquired at an archaeological site located in Veluwe, the Netherlands. In the resulting diffraction images, two potential anomalies are identified, which might correspond to the locations of suspected burial burnt stones. Such objects are confirmed by an independent magnetic survey and corings.

In chapter 5, we focus on delineating subsurface properties from the surface waves, which are mostly regarded as noise in the previous chapters. We employ 2D elastic FWI to characterize the near-surface structures using shallow seismic data. We propose an amplitude-unbiased coherency measure as a misfit function that can be incorporated into FWI. Such coherency measure is inspired by the PWS technique that is used in chapters 2 and 3 for weak but coherent diffraction stacking. In the PWS, an amplitude-unbiased coherency is estimated from the exponential phase, which is then used to enhance the stacking of signals with a similar instantaneous phase. The benefit of our new FWI approach is that it can extract information uniformly over seismic signals (surface waves, reflections, and diffractions). In this chapter, we present the details on how to calculate efficiently the gradients of this new misfit function using the adjoint-state method. We apply our new FWI approach to data recorded at an archaeological site located in Ostia, Italy. The goal of this survey was to characterize a buried tumulus and investigate the possible presence of other buried structures of archaeological significance.

The tumulus, known to be buried under a shallow soil cover, can be identified in our FWI results. Our results also show that the subsurface of this unexcavated part of the archaeological site of Ostia has a high degree of heterogeneity, with the likely presence of small objects in the shallow subsurface.

In chapter 6, we focus on developing a complete workflow that can determine subsurface S-wave velocity models inverted from 2D near-surface seismic data in a stable way. We make use of a combination of SVI and matching filters to accurately retrieve the dominant surface waves from the inline direction. The retrieved surface waves are then input into the FWI algorithm, with starting models obtained from multichannel analysis of surface waves (MASW). The subsurface structures derived from inverting the retrieved data can be interpreted together with the sections resulting from the FWI of the original data, with the aim to mitigate the potential misinterpretation of artifacts caused by noise and 3D scattered events from the crossline direction. We apply our method to data acquired at an archaeological site to characterize the near-surface structures. Our result shows that it is possible to invert 2D near-surface seismic data even when the data quality is lowered by strong noise and presence of 3D scattered events from objects located in the crossline direction. We demonstrate that 2D elastic FWI can be an efficient geophysical tool for archaeological site investigation in a non-invasive way.

2

SEISMIC INTERFEROMETRY FACILITATING THE IMAGING OF HIDDEN REFLECTORS

High-resolution reflection seismics is a powerful tool that can provide the required resolution for subsurface imaging and monitoring in archaeological settings. Shallow seismic reflection data acquired in soil-covered sites are often contaminated by source-coherent surface waves (SWs) and other linear moveout noises (LMON) that might be caused by, e.g., anthropogenic sources or harmonic distortion in vibroseis data. In the case of shear-wave seismic reflection data, such noises are particularly problematic as they overlap the useful shallow reflections. In this chapter, we propose new schemes for suppressing such surface-wave noise and LMON while still preserving shallow reflections, which are of great interest to high-resolution near-surface imaging. We do this by making use of two techniques. First, we make use of seismic interferometry (SI) to retrieve predominantly source-coherent SWs and LMON. We then adaptively subtract these dominant source-coherent SWs and LMON from the seismic data in a separate step. We illustrate our proposed method using synthetic and field data. We compare results from our method with results from frequency-wavenumber ($f-k$) filtering. Using synthetic data, we show that our schemes are robust in separating shallow reflections from source-coherent SWs and LMON even when they share very similar velocity and frequency contents, whereas $f-k$ filtering might cause undesirable artefacts. Using a field shear-wave reflection dataset characterised by the presence of overwhelming LMON, we show that the reflectors at a very shallow depth can be imaged because of significant suppression of the LMON due to the application of the scheme that we have developed.

The main contents of this chapter have been published in *Near surface Geophysics*, 2018, **16(3)**: 372-382 [Liu et al., 2018]. For consistency, minor changes have been made.

2.1. INTRODUCTION

For archaeological site investigation, highly detailed information about the subsurface structure in depth to a few meters is often required. Among all available geophysical methods, for soil-covered areas, high-resolution reflection seismics using shear or S-waves (e.g., [Ghose et al., 1996; Ghose and Goudswaard, 2004; Hasbrouck, 1991; Konstantaki et al., 2015b; Krawczyk et al., 2013; Pugin et al., 2004; Pullan et al., 1990]) is one of the few options to accomplish the target resolution of the subsurface in an archaeological setting. For example, using specialised seismic vibratory sources and shear waves, it has been possible in the past to achieve decimetre-scale seismic resolution in the near-surface soils [Brouwer et al., 1997; Ghose, 2002; Ghose et al., 1996; Ghose and Goudswaard, 2004; Ghose et al., 1998].

However, most archaeological sites are soil-covered. Shallow shear-wave reflection data acquired in such soil-covered sites are characterised by a large amount of (dispersive) surface waves (SWs), which generally camouflage the very shallow reflections. The conventional techniques for suppression of SWs, e.g., muting or spatial filtering [Yilmaz, 2001], are ineffective or even detrimental to the target reflections in suppressing this source-generated noise, especially at near offsets. This is especially challenging in archaeological settings where the available source-receiver offset is often quite limited, and the velocity and frequency content of the SWs largely overlap with those of the target shear-wave reflections (unlike compressional wave reflections, which usually have much higher velocities than the SWs). The first goal of the present chapter is, therefore, to reduce the SWs due to the active source (source-coherent SWs) and reveal the very shallow reflections in the recorded data using seismic interferometry (SI) and adaptive subtraction (AS).

Also, human activities (e.g., nearby traffic, construction works, or movement of people) are common during archaeological seismic surveys. When many such noise sources are excited simultaneously in the crossline direction, the traveltime from these noise sources to all receivers depends on the distance between these sources and the receivers. In this setting, such noise sources are mainly linearly distributed (such as in construction works or for moving vehicles), which means that the traveltime of such noise recorded in the shot gather has a linear moveout. These arrivals exacerbate the already difficult problem of removing the SWs generated by the active source used in the seismic survey. The source-incoherent SWs can result in lower resolution in the imaging results and even lead to wrong seismic interpretation. The second motivation of the present study is to remove such source-incoherent SWs using new processing schemes that we developed.

In this chapter, we first present the steps for the implementation of our method. We then demonstrate the feasibility of our method in suppressing SWs (from both inline and crossline directions) through modelling studies. Finally, we implement this method on a field dataset that is heavily contaminated by such noises.

2.2. METHODOLOGY

In our proposed method, we make use of SI to retrieve, at first, the dominant SWs. The retrieved surface-wave energy is then adaptively subtracted from the data. For the horizontal arrivals (or dipping arrivals), they are retrieved at both causal and acausal times.

Hence, they need to be isolated from the retrieved data in order to be further shifted back to the position of the physical arrivals; this is done by using singular value decomposition (SVD) filtering (for dipping arrivals, this involves linear moveout correlation, SVD, and then inverse linear moveout). In this section, we first state how to implement SI, AS, and SVD filtering separately. Then, a workflow is presented to describe how to assemble the separate operations to suppress different types of SWs.

2.2.1. SEISMIC INTERFEROMETRY

SI refers to the process of estimating the full Green's function (GF) between two receivers, by cross-correlating the recordings at the two receivers and stacking the cross-correlations for all the sources [Snieder, 2004; Wapenaar and Fokkema, 2006]. For the near-surface seismic survey using active sources, the retrieved GF ($\hat{\mathbf{G}}(X_A, X_B, \omega)$) between two receivers at X_A and X_B can be determined by [Halliday et al., 2007]:

$$\hat{\mathbf{G}}(X_A, X_B, \omega) + \hat{\mathbf{G}}^*(X_A, X_B, \omega) = \sum_{i=1}^{N} \hat{\mathbf{G}}^*(X_B, X_i, \omega)\hat{\mathbf{G}}(X_A, X_i, \omega)\Delta X_i, \tag{2.1}$$

where $\hat{\mathbf{G}}(X_B, X_i, \omega)$ is a recording at X_B from a source at X_i represented in the frequency domain as indicated by the hat above $\mathbf{G}$; the asterisk $(*)$ denotes the complex conjugation in the frequency domain, which corresponds to time reversal in the time domain. N represents the number of active sources. If the sources were impulses, $\hat{\mathbf{G}}$ would have represented an impulse response. For transient sources, $\hat{\mathbf{G}}$ on the left-hand side of equation 2.1 would represent a pressure or a particle-velocity recording convolved with the autocorrelation of the source's time function. Via equation 2.1, we can turn the receiver at X_B into a virtual source. If we keep the receiver at X_B fixed and repeat the correlation and summation process for all the other receivers, the resulting retrieved result can approximate a virtual common-source gather with a virtual source located at X_B. The theory of SI requires that the sources effectively surround the receivers and illuminate them homogeneously [Wapenaar and Fokkema, 2006]. When the receivers are at the free surface, i.e., $\hat{\mathbf{G}}$ represents a particle-velocity recording, active sources are required only in the subsurface [Wapenaar and Fokkema, 2006]. For the usual seismic exploration, e.g., for near-surface imaging, the active sources are present at the free surface, where they are not required for the application of equation 2.1. Because of that, the retrieved result would contain not only physical arrivals, the direct and SWs, but also pseudo-physical reflections and non-physical arrivals [Draganov et al., 2012a,b; King and Curtis, 2012; Mikesell et al., 2009]. For a line survey, as all active sources are at the surface, they all will contribute to the retrieval of the direct and SWs because all of them fall into the so-called stationary phase region [Snieder, 2004]. This way, the result retrieved by SI will be dominated by SWs, as they are the most energetic arrivals in a recording from active sources at the surface.

2.2.2. ADAPTIVE SUBTRACTION

We use Figure 2.1 to illustrate the basic principles of AS. Figure 2.1(a) can be considered as a simple seismic data that consist of four events: one weak reflection at 100 ms and another three high-amplitude surface-wave arrivals at 200, 300, and 400 ms, respectively.

Figure 2.1(b) corresponds exactly to the surface-wave part of Figure 2.1(a). By minimising the difference between Figure 2.1(a) and Figure 2.1(b), the SWs in Figure 2.1(a) can be suppressed. This is done by estimating a shaping filter **f** that can minimise the following objective function:

$$\mathbf{D}^{refl} = |\mathbf{D} - \mathbf{f} * \mathbf{D}^{sw}|_{min}, \tag{2.2}$$

where **D** is the raw data (Figure 2.1(a)), $\mathbf{D}^{sw}$ contains the surface-wave part of **D** (Figure 2.1(b)), and $\mathbf{D}^{refl}$ (Figure 2.1(d)) represents the data after suppression of the SWs. We obtain this shaping filter **f** using the **L1**-norm, which follows the approach proposed by Guitton and Verschuur [2004]. The convolution between the estimated shaping filter **f** and $\mathbf{D}^{sw}$ (Figure 2.1(b)) leads to $\mathbf{f} * \mathbf{D}^{sw}$ (Figure 2.1(c)), which will then be directly subtracted from **D** (Figure 2.1(a)), giving $\mathbf{D}^{refl}$ following equation 2.2, see Figure 2.1(d). Comparing Figure 2.1(a) and Figure 2.1(d), we can see that the strong SWs have been greatly reduced in Figure 2.1(d), while the weak reflection at 100 ms is preserved.

In a field seismic reflection experiment, the exact location of SWs in the shot gather (see Figure 2.1(b)) are unknown. However, SI has proven to be a robust tool for estimating the surface-wave energy between receivers under certain survey geometry [Dong et al., 2006; Halliday et al., 2007; Konstantaki et al., 2015a]. This means that the retrieved SWs can then be regarded as an input for AS (as in Figure 2.1(b)), which will be adaptively subtracted from the data (as in Figure 2.1(a)).

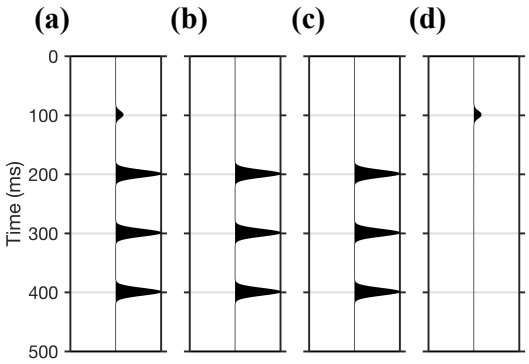

Figure 2.1: Illustration of the basic steps involved in AS: (a) **D** is seismic data with one weak reflection and three high-amplitude SWs; (b) $\mathbf{D}^{sw}$ is the SWs part of Figure 2.1(a); (c) $\mathbf{f} * \mathbf{D}^{sw}$ results from convoluting the estimated shaping filter **f** with Figure 2.1(b); (d) $\mathbf{D}^{refl}$ is data after surface-wave suppression.

2.2.3. SVD FILTERING

Multi-trace seismic data can be represented as a matrix **C** of size $(m \times n)$, where m denotes the trace number and n denotes time samples. The SVD of matrix **C** is the factorisation of **C** into the product of three matrices [Eckart and Young, 1936], which is $\mathbf{C} = \mathbf{USV}^{\mathbf{T}}$, where **U** and **V** are the orthonormal left and right singular vectors, and matrix **S** is a diagonal matrix composed of the singular values of the original matrix **C**, in

descending order. By taking only the contribution of the first **j** singular values from **C**, a lower-rank approximation of **C** is obtained as: $\mathbf{C_j} = \mathbf{US_jV^T}$. Figure 2.2 illustrates how matrix **C** is approximated by its lower-rank matrix $\mathbf{C_j}$. Since SVD is a coherency-based technique [Bekara and van der Baan, 2007], for the horizontal arrivals in Figure 2.2(a), which show a high degree of coherency across the traces, they can be nicely isolated from the data by setting **j** to 2 (Figure 2.2(d)).

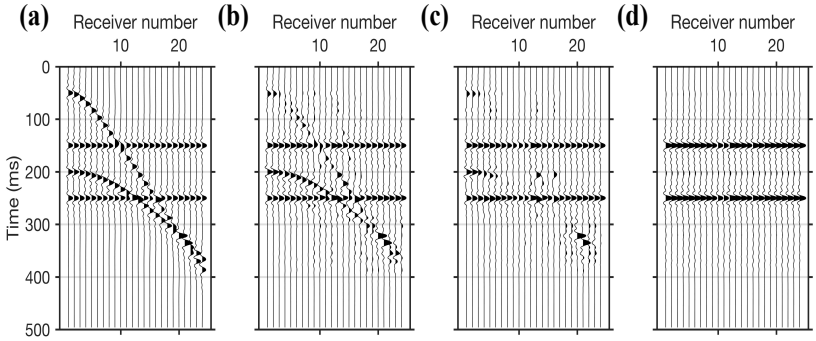

Figure 2.2: Illustration of the steps necessary to isolate horizontal arrivals from the seismic reflection shot gather using singular value decomposition filtering: (a) synthetic seismic data (representing matrix **C**) with two horizontal noise events; (b–d) the low-rank matrix $\mathbf{C_j}$, by setting **j** to 12, 6, and 2, respectively.

2.3. MODELLING STUDIES FOR SURFACE-WAVE SUPPRESSION

2.3.1. SOURCE-COHERENT SWS

In Figure 2.3, we present the flowchart of the scheme for implementing SI + AS. Next, to demonstrate the effectiveness of SI + AS in the removal of different types of SWs, which we typically confront in data from archaeological sites (where high-resolution seismic imaging is often of great value), we perform synthetic modelling studies. We consider a four-layer model (Figure 2.4). A three-layered partially saturated top soil with a total thickness of 12 m overlies the fully saturated soil below. We use an elastic finite-difference (FD) modelling scheme to generate synthetic common-source gathers [Thorbecke and Draganov, 2011]. The first source is positioned at 0 m and the last one at 30 m; the source spacing is 1 m. The array of receivers starts at 6 m and ends at 23.5 m, with a 0.5 m spacing between the receivers. Following the criteria of stability and numerical dispersion, we set the spatial grid of the model at 0.1 m and the time step of the modelling at 0.02 ms. To model the shear wave, which we generated and recorded in the field data, the sources are excited along the inline direction, and the vertical components of the data are used. The source signature is a 90-Hz Ricker wavelet. To suppress the reflections from the bottom and the side boundaries during the numerical modelling, we implement absorbing boundary conditions for these boundaries with a taper of 100 points.

Figure 2.5(a) shows an example of synthetic shot gathers for the source positioned at 15 m along the horizontal direction of the survey line. The SWs, especially at a far

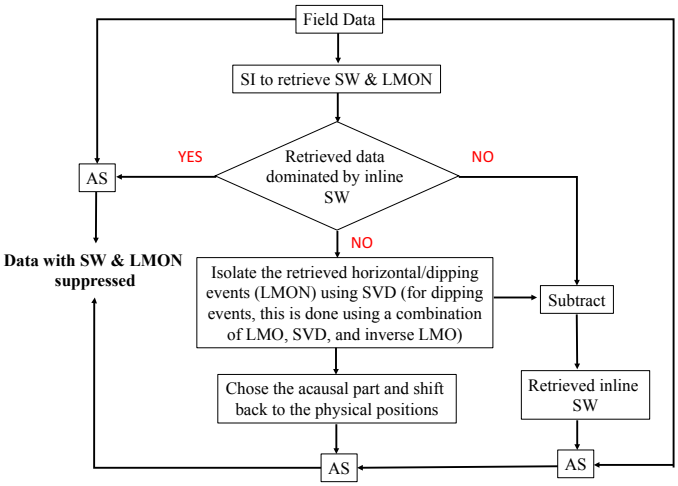

Figure 2.3: Flowchart for the implementation of SI + AS schemes to suppress source-coherent SWs and linear moveout noises (LMON).

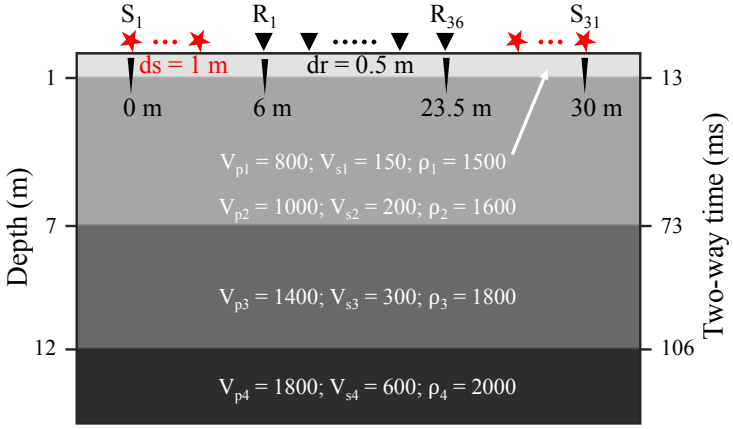

Figure 2.4: Model used to generate synthetic shot gathers. The units of V_P, V_S, and ρ are m/s, m/s, and kg/m^3, respectively. The acquisition geometry used for the synthetic studies is illustrated at the top of the model. The red stars represent sources, whereas the black triangles are receivers. The depth of each interface and its corresponding shear-wave reflection two-way time are shown on the left and right vertical axes, respectively.

offset (see red ellipse in Figure 2.5(a)), mask the useful reflections. To reveal these reflections, we first make use of SI to retrieve a virtual common-source gather for a receiver located at 15 m (this receiver becomes the virtual source), following the steps described earlier in the Methodology section 2.2. As shown in Figure 2.5(b), the dominant SWs in Figure 2.5(a) are retrieved well, whereas the retrieved reflections are significantly suppressed. We then adaptively subtract Figure 2.5(b) from Figure 2.5(a), which results in

Figure 2.5(c). We analyse this result in Figure 2.6(c), by comparing it with the data after conventional $f-k$ filtering (Figure 2.6(b)). We also show a reference shot gather (Figure 2.6(d)) without the SWs, modelled by replacing the free surface with a homogeneous half space, to verify the effectiveness of these two techniques. As can be seen in Figure 2.6(c), SI + AS does well in suppressing SWs, and hence, two reflections with moveouts similar to the true reflections in Figure 2.6(d) can now be easily identified. For the used simple model, $f-k$ filtering also delivers good results, and these two reflections can also be identified in Figure 2.6(b); however, to avoid filtering out the reflection from the interface at 7 m, some surface-wave energy still leaked through the filter, as can be seen above that reflection.

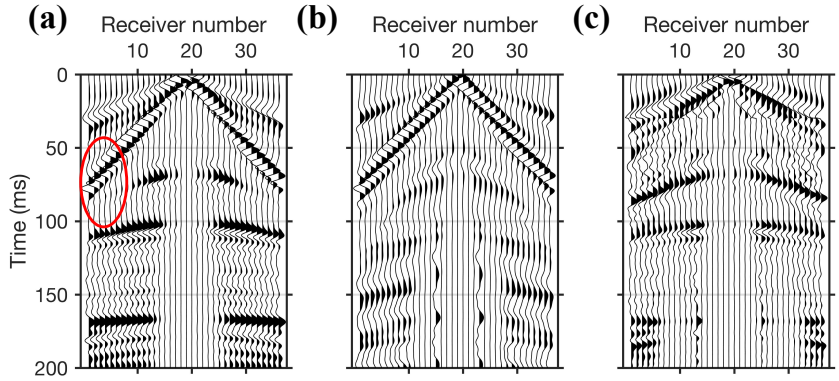

Figure 2.5: Steps for the implementation of the SI + AS scheme to suppress source-coherent SWs: (a) a synthetic shot gather from the source located at 15 m; (b) retrieved virtual common-source gather using SI, with a virtual source positioned at 15 m; (c) result after AS of the data in Figure 2.5(b) from the data in Figure 2.5(a). The red ellipse highlights the area where the SWs overlap the reflection. For a better visualisation of events, an automatic gain control (AGC) with a window length of 50 ms is applied to the shot gathers. This same AGC is also applied to all other synthetic shot gathers presented in the following illustrations.

To pick root-mean-square velocities for stacking, we then carry out an analysis using constant velocity stack (CVS) in the common midpoint (CMP) domain for the raw data, for the data after $f-k$ filtering, and for the data after SI + AS. A selected representative part of the constant velocity stacked section is displayed in Figure 2.7. Because the SWs present in the modelled data are characterised by moveout velocities similar to those of the useful reflection events, the alignment in the panels in Figure 2.7(a) is ambiguous, making the picking of velocities inaccurate. Such ambiguity is significantly reduced in Figure 2.7(b), which shows CVS of the same data after $f-k$ filtering. As is shown in Figure 2.7(b), the first event is flat in the first panel, whereas the second event is in the third panel. Figure 2.7(c) is the CVS of these data after SI + AS. Comparing Figure 2.7(b) and Figure 2.7(c), we find that they both offer the same ease for picking the root-mean-square velocity (0 ms – 170 m/s; 68 ms – 210 m/s); these velocities will be used in the following stacking procedure. However, Figure 2.7(c) shows a higher signal-to-noise ratio (S/N), when inspected carefully (e.g., the blue ellipse). We will further compare in the stacked section this effectiveness of suppressing different types of SWs using $f-k$ filtering and

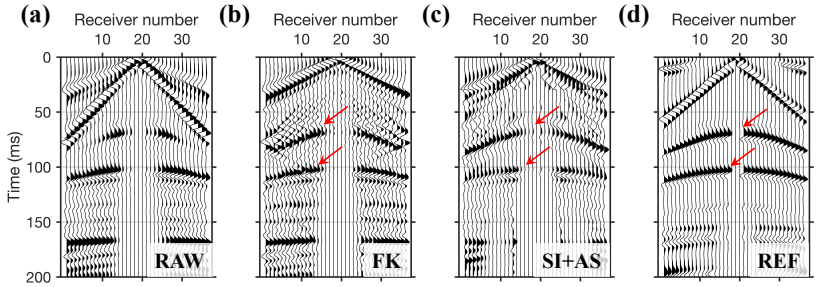

Figure 2.6: Comparison between the shot gather as in Figure 2.5(a) and the results after the application of $f-k$ filtering and after SI + AS: (a) raw data as in Figure 2.5(a); (b) result after $f-k$ filtering; (c) result after SI + AS; (d) corresponding reference gather modelled without the surface wave. The red arrows mark the primary shear-wave reflections from the interfaces of the model (at depths of 7 and 12 m), shown in Figure 2.4.

SI + AS schemes.

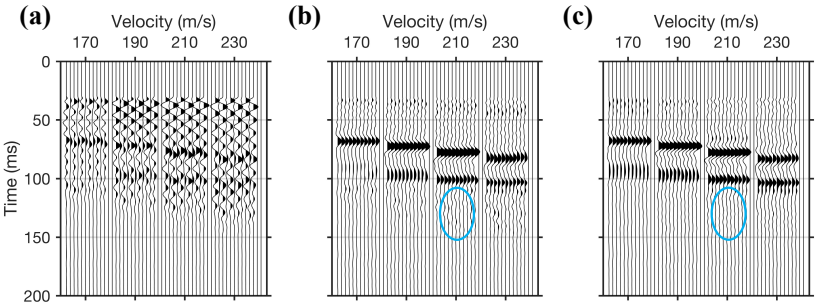

Figure 2.7: Comparison between CVS from the raw data, data after $f-k$ filtering, and data after SI + AS: (a) CVS section from the data as in Figure 2.6(a) without the removal of SWs; (b) CVS section after $f-k$ filtering; (c) CVS section after SI + AS. For the CVS sections (e.g., Figure 2.7(a)), each subpanel shows a part of the stacked section, located from 14 to 16.5 m in the model, obtained from stacking with different velocities labelled above the x-axis. The CVS sections (also the stacked sections in the following synthetic studies) are displayed without automatic gain control, but after top muting the part above 30 ms. The blue ellipse highlights noise in Figure 2.7(b) that has a higher amplitude than in Figure 2.7(c).

Figure 2.8(a) shows the stacked section obtained from the raw (unfiltered) active-source data. In this stacked section, the inclined high-amplitude SWs (as the one marked by the red ellipse) overlap the shallow shear-wave reflectors, making it difficult to identify the latter in this area. However, due to the effective removal of the SWs by the application of SI + AS, in the resulting stacked section, shown in Figure 2.8(c), these same reflectors (red arrows) are much more continuous and clearer, and thus quite easy to interpret. These reflectors are also correctly imaged in the stacked section after $f-k$ filtering, as is shown in Figure 2.8(b). However, due to the close overlap between SWs and reflections in the $f-k$ domain, it is difficult to design the $f-k$ filtering parameters to suppress sufficiently the SWs. This leads to some leakage of SWs at certain shots. The artefacts

in Figure 2.8(b) (see the red ellipse) are caused by the stacking of such leaked surface-wave energy. Note that the results in Figure 2.8(b) and (c) exhibit apparent curving of the reflector at 7 m and lower amplitude of the reflector at 12 m on the left and right sides. This is caused by reduced stacking power in the CMP gathers at those positions.

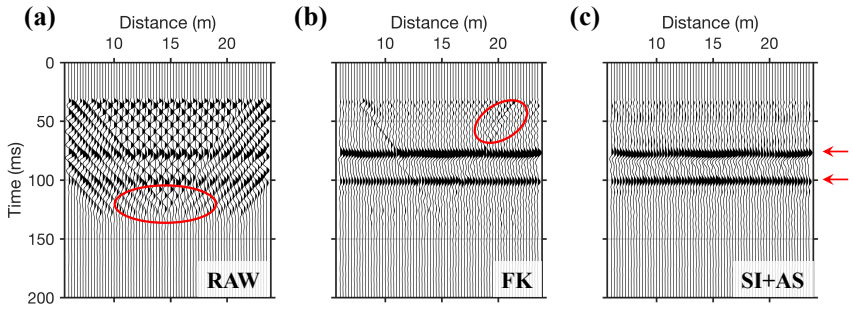

Figure 2.8: Comparison between stacked sections (located from 6 to 23.5 m), from the raw data, data after $f-k$ filtering, and data after SI + AS: (a) stacked section from data as in Figure 2.6(a) without the removal of SWs; (b) stacked section after $f-k$ filtering; (c) stacked section after SI + AS. The areas highlighted by red ellipses are caused by the stacking of SWs. We indicate the theoretical shearwave two-way time from the second and third reflectors of the model in Figure 2.4 with red arrows on the right side of the panels.

2.3.2. SOURCE-COHERENT SWS AND HORIZONTAL LMON

When conducting seismic surveys in archaeological environments, often, the recorded data contain SWs that are not connected to the active source used in the survey. Such SWs could be due to traffic passing close to the survey site, walking people, etc. These SWs most likely would not be aligned with the survey line, but would be propagating in a crossline direction. This kind of surface-wave energy, unlike the SWs generated by the active sources that we have discussed in the previous modelling study 2.3.1, can be retrieved by the application of SI at times that are different from the times in the original active-source data, i.e., they will result in the retrieval of nonphysical arrivals. Hence, such source-incoherent SWs are hard to suppress from the original data using the procedure described above. Therefore, we consider a new approach to suppress this type of noise to make the previous SI + AS scheme work also in this situation.

When the noise source that generates the crossline SWs is moving parallel to the survey line (e.g., from traffic passing by) and when the noise source is not too close to the receivers, the traveltime from the noise source to each receiver is almost the same. These arrivals will be characterised by nearly horizontal moveouts. To simulate this situation, we add SWs with horizontal moveouts to our previously modelled data. In Figure 2.9(a), we show an example of the resulting synthetic shot gather and mark areas containing this type of surface-wave energy with blue arrows. Figure 2.9(b) illustrates the result of the application of SI. We can see the dominant retrieved non-physical surface-wave arrivals at both causal and acausal times — the horizontal arrivals at 0 ms and about ± 100 ms. The other dominant retrieved arrival is the source-coherent surface wave.

Concentrating on the horizontal SWs, we can see that in Figure 2.9(b), the horizon-

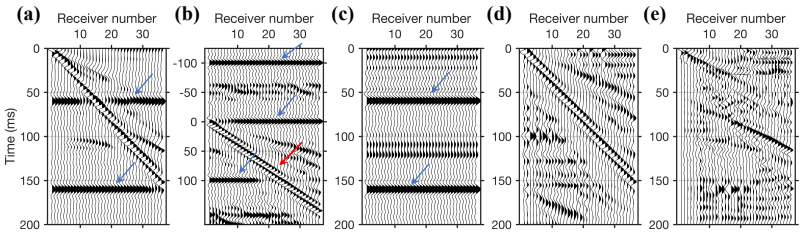

Figure 2.9: Steps for the implementation of the SI + AS to suppress source-coherent SWs and horizontal LMON: (a) a synthetic shot gather for a source located at 6 m, where the blue arrows mark the horizontal LMON; (b) retrieved virtual common-source gather using SI for a virtual source located at 6 m, where the blue and red arrows indicate the retrieved horizontal LMON and the retrieved inline SWs, respectively; (c) retrieved horizontal arrivals that are isolated using singular value decomposition and then manually moved to the time of the corresponding events in Figure 2.9(a); (d) retrieved inline SWs extracted from Figure 2.9(b) through subtraction of the retrieved horizontal LMON; (e) result after AS of the data in Figure 2.9(c) and Figure 2.9(d) from the data in Figure 2.9(a).

tal arrivals (marked by blue arrows) are retrieved, but at times not coincide with the times in the original data. This happens as the SI process effectively eliminates the common travel path shared by the two arrivals recorded at the two receivers. The SI process "recognises" the earlier horizontal surface wave in Figure 2.9(a) as the arrival bearing the common travel path, and eliminates its time from the time of the later horizontal surface wave. To approximate both horizontal SWs in Figure 2.9(a) as good as possible, we first apply SVD filtering to isolate them from the rest of the retrieved arrivals. We then use the acausal part of the isolated horizontal arrivals and shift them back to the physical time of the original horizontal SWs in Figure 2.9(a), which results in Figure 2.9(c). The shifting is currently performed manually, but this process could be automated (beyond the scope of this work). We use the acausal part as it is free from interference from other arrivals. Looking at the retrieved inline SWs (red arrow in Figure 2.9(b)), we see that its arrival time is consistent with the time of the original inline surface wave in Figure 2.9(a) (as should be expected from what was shown in modelling study 2.3.1). For this retrieved arrival, we only need to isolate it by subtracting the full isolated horizontal arrivals from Figure 2.9(b), and then taking the causal part of the result, which gives the outcome as shown in Figure 2.9(d). Finally, these retrieved dominant arrivals (Figure 2.9(c) and (d)) can now be adaptively subtracted one after the other from the original gather (Figure 2.9(a)), resulting in Figure 2.9(e).

We also apply $f-k$ filtering to Figure 2.9(a) in an attempt to suppress the inline SWs and the horizontal arrivals, the result of which is shown in Figure 2.10(b). Comparing Figure 2.10(b) and Figure 2.10(d), we see that two reflections can now be identified (red arrows in Figure 2.10(b)), because of the removal of the inline SWs after $f-k$ filtering. However, the performance of $f-k$ filtering in suppressing the horizontal arrivals is not good enough, as can be seen in Figure 2.10(b), which leads to a large amount of those horizontal arrivals still remaining. On the contrary, those horizontal arrivals, along with inline SWs, are significantly reduced in Figure 2.10(c), leading to the emergence of two clear reflections (red arrows in Figure 2.10(c)).

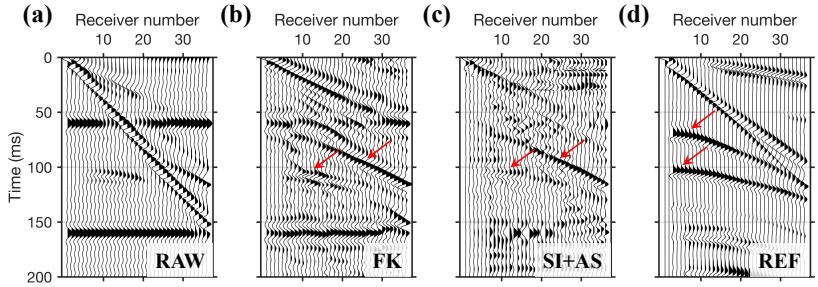

Figure 2.10: As in Figure 2.6, but in the case of suppression of both source-coherent SWs and horizontal LMON. The red arrows indicate the reflections from the interfaces of the model (Figure 2.4) at depths of 7 and 12 m.

Figure 2.11(a) is the stacked section obtained from the original data (containing the source-coherent and source-incoherent SWs). Figures 2.11(b) and (c) show the stacked sections obtained from the same data after the suppression of these two types of SWs using $f-k$ filtering and SI + AS schemes, respectively. The events (e.g., red rectangle in Figure 2.11(a)), caused by the stacking of source-incoherent surface-wave arrivals, can be wrongly interpreted as reflectors because of their continuity and clarity, which would be problematic in archaeological seismic surveys. As is visible in Figure 2.11(b), $f-k$ filtering fails to suppress these artefacts sufficiently (e.g., red rectangle in Figure 2.11(b)) due to poor performance to suppress these horizontal arrivals without damaging the reflections. However, such artefacts are greatly reduced in Figure 2.11(c) — the reflectors are now correctly imaged and clearly interpretable. This shows that our approach is successful in the removal of most of the inline and crossline SWs, with very little loss of the useful reflection energy.

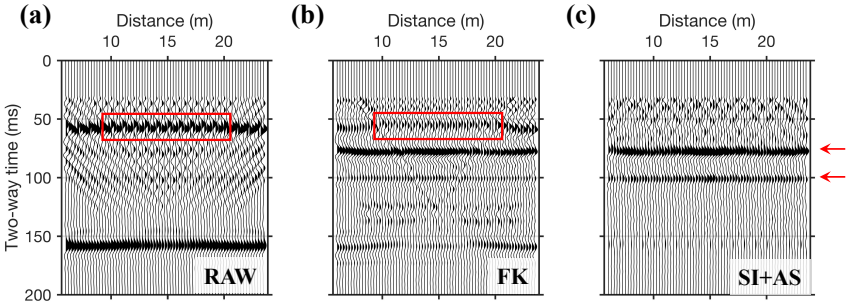

Figure 2.11: As in Figure 2.8, but for the data with source-coherent SWs and horizontal LMON. Red rectangles mark the artefacts caused by stacking LMON.

2.3.3. SOURCE-COHERENT SWS AND DIPPING LMON

Often, there are other types of noise sources (than what has been discussed above) in archaeological environments. Crossline SWs caused by these sources may be characterised by dipping moveouts. To test if the surface-wave suppression scheme that we propose in modelling study 2.3.2 could also help in the suppression of dipping crossline SWs, we add source-incoherent dipping arrivals to our previously modelled data (modelling study 2.3.1). A resulting common-source gather is shown in Figure 2.12(a), where the dipping surface-wave arrivals are marked by blue arrows. We first try to use $f-k$ filtering to suppress the inline SWs and dipping arrivals in Figure 2.12(a), which produces the result shown in Figure 2.13(b). In the $f-k$ domain, these dipping arrivals fall inside the area where also most of the reflection energy is located. To suppress these dipping arrivals using $f-k$ filtering will also mean total loss of reflection energy, as can be seen in Figure 2.13(b).

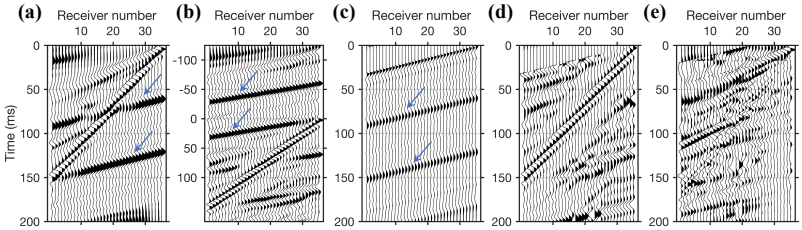

Figure 2.12: As in Figure 2.9, but in the case of suppression of both source-coherent SWs and dipping LMON. The active and virtual shots are at 24 m.

To reveal the true reflections, we apply an SI + AS scheme (as illustrated in Figure 2.12) similar to the one we used in modelling study 2.3.2. The final common-source gather resulting from this scheme is displayed in Figure 2.13(c). Two reflection events (red arrows in Figure 2.13(c)) have been revealed by the SI + AS procedure, and they can now be identified. Comparing the result in Figure 2.13(c) with the reference result shown in Figure 2.13(d), we notice that the amplitudes of the revealed reflections in Figure 2.13(c) have been greatly weakened after the SI + AS procedure; nevertheless, they can be well utilised in near-surface imaging.

Figure 2.14(a) shows the CMP stacked section using the data without surface-wave suppression. Two features (see the red rectangle in Figure 2.14(a)) with high amplitude and good continuity can be wrongly interpreted as reflectors. These features are due to the stacking of the dipping SWs. These artefacts can be utterly misleading in the archaeological geophysical interpretation. Figure 2.14(b) shows the stacked section from the data after surface-wave suppression using $f-k$ filtering. Because of the failure of the $f-k$ filter to suppress the dipping arrivals, artefacts (see the red rectangle in Figure 2.14(b)) caused by stacking these arrivals remain in Figure 2.14(b). The stacked section after surface-wave suppression using SI + AS is shown in Figure 2.14(c). Due to the successful suppression of the dipping SWs, the artefacts (e.g., red rectangle in Figure 2.14(a)) have nearly disappeared from Figure 2.14(c). Therefore, we can now easily and correctly interpret the two deeper reflectors in Figure 2.14(c).

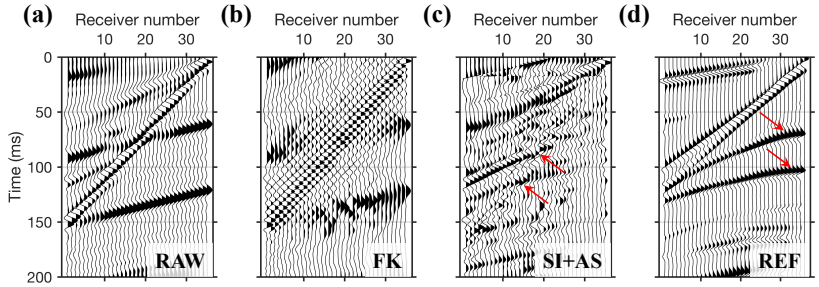

Figure 2.13: As in Figure 2.10, but in the case of suppression of both source-coherent SWs and dipping LMON. The active and virtual shots are at 24 m.

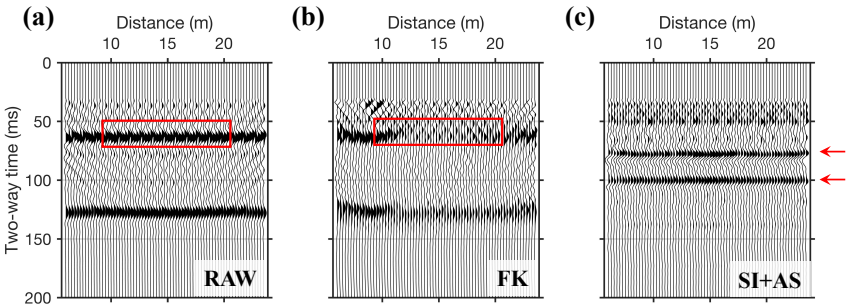

Figure 2.14: As in Figure 2.11, but for the data with source-coherent surface waves and dipping LMON.

2.4. FIELD-DATA EXAMPLE

In a high-resolution S-wave reflection survey, the receiver line consisted of 120 horizontal-component geophones spaced at a 0.25-m interval, ranging from 42 to 71.75 m. The geophones were oriented in the crossline direction. The receiver array was fixed during data collection, because of the limited available space in the survey area, which is a common constraint in archaeological settings. As a source, we used a high-frequency electrodynamic horizontal vibrator [Brouwer et al., 1997; Ghose, 2012; Ghose et al., 1996; Ghose and Goudswaard, 2004] also oriented in the crossline direction. The source spacing was 1 m, starting from 42 to 62 m. As both the sources and the receivers are oriented in the crossline direction, we made use of shear waves polarised in the crossline direction, i.e., SH-waves. The record length was 4 seconds. After vibroseis source signature deconvolution [Ghose, 2002], we obtain common-source gathers with a length of 0.5 seconds. Figure 2.15(a) shows an example common-source gather after the application of AGC (180 ms) and band-pass filtering (3-8-150-200 Hz). During the field work, due to the surface condition and source coupling, unfortunately, harmonic distortion was significant in the compressed vibrator data, which showed up as LMON (blue ellipse in Figure 2.15(a)). This kind of noise, together with the source-coherent SWs, is difficult to suppress using traditional filtering techniques (e.g., $f-k$ filtering and notch filtering),

due to the very similar frequency content and moveout velocity of the informative reflection signals. This makes this dataset ideal for testing the efficacy of our newly developed scheme.

To restore the true reflectors from this severely noise-contaminated data, we apply the SI + AS scheme, as illustrated in modelling study 2.3.3, to the data shown in Figure 2.15(a), with the main aim to suppress the dipping arrivals (see the area inside the blue ellipse). The result is shown in Figure 2.15(c). Comparing the common-source gathers in Figure 2.15(a) and (c), we can see that the dipping arrivals are significantly suppressed, and shallow reflections around 100 ms can now be identified clearly in Figure 2.15(c). We interpret them as true reflections because they are crisp and they also show clear hyperbolic moveouts in shot gathers. For the same gather, after $f-k$ filtering (Figure 2.15(b)), it is difficult to identify such shallow reflection events.

Figures 2.15(d)–(f) present the stacked section from the raw (unfiltered) field data, data after $f-k$ filtering, and data after SI + AS, respectively. In Figure 2.15(e), we see that there are many artefacts (example marked by a red rectangle) caused by $f-k$ filtering. Without prior knowledge about the subsurface, the interpretation can become erroneous. However, in Figure 2.15(f), we can identify a shallow reflector at around 100 ms two-way time, with a vertical resolution of less than 1 m, because of good quality stacking. This is due to the success of the SI + AS scheme in suppressing LMON, while preserving the shallow shear-wave reflections.

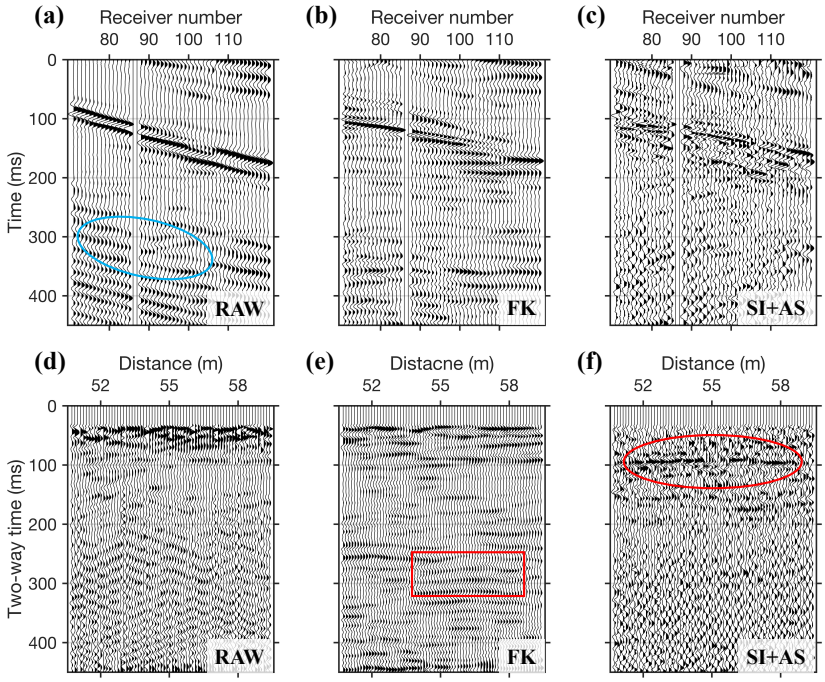

Figure 2.15: Comparison between field shear-wave shot gathers: (a) a typical raw shear-wave shot gather acquired in the field contaminated by dipping LMON (blue ellipse), with the source located at 50 m; (b) result after careful $f-k$ filtering; (c) result after SI + AS, following the procedure outlined in Figure 2.3. Comparison between field shear-wave stacked sections: (d) using raw (unfiltered) field data; (e) using $f-k$ filtered data; (f) using SI + AS data. The red rectangle highlights the artefacts caused by $f-k$ filtering, whereas the red ellipse marks the revealed shallow reflectors via SI + AS.

2.5. CONCLUSIONS

High-resolution reflection seismics using shear waves can be very effective in subsurface investigations in soil-covered archaeological sites. However, a successful application of the method can be hampered by the presence of source-coherent surface waves (SWs) and/or other linear moveout noises (LMON) in the field data, which camouflage the shallow shear-wave reflection events. In this chapter, we developed new schemes for the data-driven suppression of such surface-wave noise and LMON, while preserving the shallow reflections. Using numerical modelling data, we showed how a combination of SI and AS can significantly suppress the inline (source-coherent) SWs and LMON and, hence, improve significantly the imaging of shallow subsurface structures. In comparison with frequency-wavenumber ($f-k$) filtering, we demonstrate that our schemes are effective in separating reflections from source-coherent SWs and LMON, even when they overlap greatly in the $f-k$ domain. When applied to field shear-wave reflection data that are heavily contaminated by LMON, we found that crisp and clear shallow reflectors could be revealed, due to significant suppression of LMON as a result of the application of the newly developed seismic interferometry (SI) + adaptive subtraction (AS) schemes.

3

SEISMIC INTERFEROMETRY ASSISTING THE DETECTION OF NEAR-SURFACE HETEROGENEITIES

Detecting small-size objects is a primary challenge at archaeological sites due to the high degree of heterogeneity typically present in the near surface. Although high-resolution reflection seismic imaging often delivers the target resolution of the subsurface in different near-surface settings, the standard processing for obtaining an image of the subsurface is not suitable to map local diffractors. This happens because shallow seismic-reflection data are often dominated by strong surface waves (SWs), and because traditional common-midpoint moveout corrections are primarily optimal for reflection events. In this chapter, we propose an approach for imaging subsurface objects using masked diffractions. This method is based on a spatial summation of diffractions from these objects. We use amplitude-unbiased coherency to enhance the coherent summation of weak diffraction signals. Using synthetic data, we show that our scheme is robust in locating diffractors from data with a very low signal-to-noise ratio (S/N). We test our method on field data acquired at an archaeological site. The resulting distribution of shallow diffractors agrees with the location of anomalous objects detected in an independent magnetic survey and corings.

The main contents of this chapter have been published in *First Break*, 2019, **37(9)**: 93–97 [Liu et al., 2019]. For consistency, minor changes have been made.

3.1. INTRODUCTION

The detection of shallow buried ancient structures or objects of cultural heritage is a primary challenge for seismic surveys at archaeological sites. The knowledge of the distribution of shallow objects can assist archaeologists to study the past without making excavations. Excavations lead to surface exposure of the buried objects and potential damages and preservation issues. The seismic response arising from localized archaeological targets is encoded in diffractions, which can be used to locate the objects. However, the energy of a diffracted wave is usually weak and masked behind the strong presence of other coherent signals or coherent noise in the data (e.g., surface waves (SWs), specular reflections). This makes it difficult to detect and interpret reliably the diffractions.

For the past decades, researchers have attempted to detect various near-surface features using diffracted waves. Landa and Keydar [1998] developed a method for identifying local targets in the shallow subsurface using diffracted waves. They constructed a so-called D-section by concentrating diffracted waves from diffractor points. The anomalies in this D-section can be interpreted as potential scattering objects. Shtivelman and Keydar [2005] proposed a multipath summation approach to image near-surface objects by stacking diffracted energy along all possible diffraction curves defined by all velocity values within a specific range. Subsequently, Shtivelman et al. [2009] improved the resolution of this multipath summation approach by introducing image-dependent weights.

The above-mentioned methods have been tested earlier on field data dominated by SWs; no identification of diffracted waves could be found. To improve the reliability of diffraction imaging, in this chapter we first apply a method that consists of seismic interferometry (SI) and adaptive subtraction (AS) for the suppression of high-amplitude surface-wave noise (e.g., [Konstantaki et al., 2015a; Liu et al., 2018]). We then present an approach based on an extension of the spatial summation of weak diffractions as proposed by Shtivelman and Keydar [2005]. We utilize instantaneous-phase coherency [Schimmel and Paulssen, 1997] to enhance the optimal summation of weak but coherent diffractions.

In the following, we first describe the practical steps for the implementation of each of the above methods. We then demonstrate the feasibility of our approach in locating diffractors on numerically modelled data with a low signal-to-noise ratio (S/N). Finally, we test our method on field seismic data acquired at an archaeological site.

3.2. METHODOLOGY

3.2.1. SURFACE-WAVES REMOVAL

SI refers to the retrieval of new seismic responses between two receivers by, most commonly, cross-correlating the wavefields observed at these receivers from surrounding sources and stacking the cross-correlations for all the sources [Draganov et al., 2006; Wapenaar and Fokkema, 2006]. For a near-surface seismic survey, the active sources are located along the surface of the earth. Such a source configuration will make the results retrieved by SI dominated by SWs. Because of this, we make use of SI to retrieve the dominant SWs contained in the field data. A non-stationary matching filter [Fomel, 2009] is then estimated to adaptively subtract the retrieved SWs from the raw data, while preserving the weak diffraction events. For the implementation details of this surface-

waves suppression scheme, we refer the readers to Chapter 2 [Liu et al., 2018].

3.2.2. DIFFRACTION IMAGING

Assume a diffractor located at (X_D, Z_D) in a homogeneous medium. For an arbitrary source located at (X_S,0), a part of the wavefield emitted by this source will first travel downward and hit the diffractor. It will then be diffracted back to the surface and recorded by a receiver positioned at (X_R,0). The traveltime curve of this diffracted event can be expressed as

$$T_{SR} = \sqrt{\left(\frac{X_D - X_S}{V}\right)^2 + \left(\frac{T_D}{2}\right)^2} + \sqrt{\left(\frac{X_R - X_D}{V}\right)^2 + \left(\frac{T_D}{2}\right)^2}, \tag{3.1}$$

In equation 3.1, the first term on the right-hand side is the source-diffractor traveltime, whereas the second term is the diffractor-receiver traveltime. V is the near-surface velocity, T_D is the two-way vertical traveltime when the source, diffractor, and receiver share the same lateral position.

We assume that every subsurface point is a candidate diffractor which can cause a diffracted event. For every point to be imaged, the seismic data is stacked along a specific diffraction trajectory defined by equation 3.1; this results in a final staked time section where diffracted energy is optimally focused.

Next, we describe the practical implementation steps of this diffraction-stacking method. For a specific source gather, we first assume that the diffractor is located directly under the first receiver. This will lead to a specific diffraction traveltime curve according to equation 3.1, where X_D is the lateral location of the first receiver. Next, we apply diffraction-moveout correction to this source gather and obtain a new gather. Such traveltime correction procedure is repeated for all other combinations of source-receiver pairs. This will result in $ns \times nr$ gathers corrected for diffraction moveout, where ns and nr are the number of sources and receivers, respectively. These moveout-corrected source gathers are then sorted into common-receiver gathers and stacked to produce one single trace per receiver position. To further enhance the coherent summation along weak diffractions, the stacked trace is then weighted by amplitude-unbiased coherency factors [Schimmel and Paulssen, 1997]. The coherency for each stacked trace is calculated from the traces involved in the stacking of the common-receiver gather used to obtain that trace using

$$c(t) = \frac{1}{N}\left|\sum_{j=1}^{N} e^{i\phi_j(t)}\right|^{\nu}, \tag{3.2}$$

where N is the number of traces used, $\phi_j(t)$ is the instantaneous phase of the j-th trace obtained by complex trace analysis [Bracewell and Bracewell, 1986]. The parameter ν controls the transition between more coherent and less coherent signal summations; here we use $\nu = 2$ as suggested by Schimmel and Paulssen [1997].

The stacked traces weighted by equation 3.2 from each common-receiver gather are then assembled into a diffraction section [Landa and Keydar, 1998; Walters et al., 2009], where anomalies indicate the spatial location of diffractors. When the near-surface velocity V is not available, we can iterate the above procedures over a specific range of

velocity values [Shtivelman and Keydar, 2005; Shtivelman et al., 2009]. In this way, the diffraction energy can be coherently focused to produce a final image.

3.3. EXAMPLES

3.3.1. SYNTHETIC DATA

The model shown in Figure 3.1a includes seven randomly distributed point diffractors at shallow depths in a homogeneous medium with a background velocity of 150 m/s. The receiver array consists of 120 geophones, starting from 0 m to 29.75 m at 0.25 m intervals. This array remains fixed, while the source advances with a step of 2 m. The first source is located at 4 m before the first geophone, while the last source is placed 7.5 m after the last geophone. With this acquisition geometry, 21 common-shot gathers (e.g., Figure 3.2a) are computed using an acoustic finite-difference algorithm [Thorbecke and Draganov, 2011]. Band-pass-filtered Gaussian random noise (S/N = 5) is then added to the clean synthetic gathers to build a new dataset. Figure 3.2b illustrates one noisy common-source gather for a source positioned at 16 m. We use this noisy dataset to demonstrate the feasibility of our approach to detect shallow diffractors.

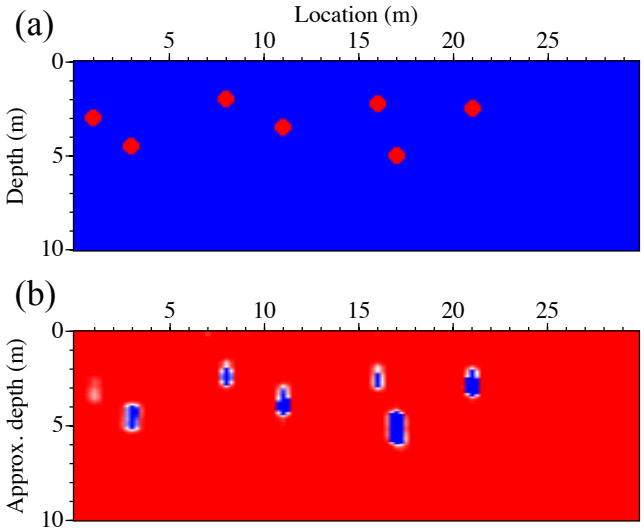

Figure 3.1: (a) Model used to generate the synthetic common-source gathers. Seven shallow diffractors with a certain impendence contrast with respect to the background medium are embedded in this model. The background velocity is 150 m/s. (b) Result of diffraction imaging through diffraction summation weighted by instantaneous-phase coherence. Seven high-amplitude anomalies can be identified in Figure 3.1(b), whose positions are very close to the true locations of the diffractors in the synthetic model. Note that the shapes of these anomalies do not necessarily correspond to the actual shapes of the objects.

Our new algorithm is designed to focus coherently the diffraction energy back to

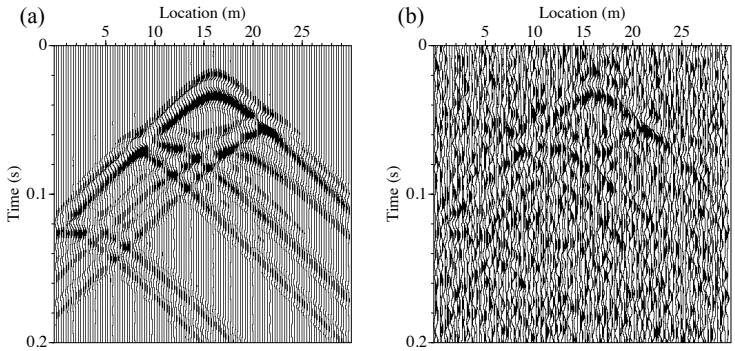

Figure 3.2: Typical example of a synthetic common-source gather for a source located at 16 m. (a) Common-source gather modelled without direct waves. (b) The same gather after adding highly uncorrelated random noise (S/N = 5).

its original position while suppressing all other incoherent events through directional summation. This procedure will make the true diffractions appear as a high-amplitude anomaly in the resulting section. Figure 3.1b represents the diffraction imaging section derived from the noisy data through our diffraction-enhancement approach. In Figure 3.1b, the horizontal axis denotes the lateral location (in m), while the vertical axis is the approximate depth (in m) that we obtain using the true subsurface velocity. The range of velocities used for diffraction summation is from 140 m/s to 160 m/s with a step of 5 m/s. We display the final time section (Figure 3.1b) using semblance calculated from diffraction sections obtained from each velocity used for stacking. We can identify seven prominent anomalies in Figure 3.1b, after significant suppression of the highly uncorrelated noise that is present in the original data. The maximum amplitudes of these anomalies can be interpreted as the centers of the diffractors, which correspond well with the true locations of the diffractors embedded in the synthetic model (Figure 3.1a).

3.3.2. FIELD DATA

We acquired in 2017 seismic data at an archaeological burial mound located in Veluwe, the Netherlands. Burial mounds are the most widespread prehistoric graves and are visible as low hillocks to this day. In the Veluwe, about 50 such burial mounds are well-preserved and are distributed along an approximately 6-km-long line. Most of these burial mounds can be dated back to about 5000 years ago [Bourgeois, 2012]. The mound that we investigated is labelled as Mound B4749, and it is located in the middle of the woods of the Veluwe.

To illuminate near-surface small objects underneath Mound B4749, we deployed an array of 120 horizontal 10-Hz single-component geophones over the top of this mound. We acquired two types of seismic data — using a sledgehammer (shear-wave) and a high-frequency horizontal (shear-wave) vibrator [Ghose, 2002; Ghose et al., 1996] as seismic sources. The reason we used shear waves is because of their relatively low propagation

velocity in soft soils — resulting in short wavelength, hence high resolution. In addition, shear waves are directly related to the small-strain rigidity and are quite sensitive to subtle changes in the subsoil mechanical properties [Ghose and Goudswaard, 2004; Ghose et al., 1998]. The source-receiver geometry used to record the impulsive hammer data was the same as the one applied to generate the synthetic data discussed above. We covered 41 source positions at an interval of 1 m to acquire the shear-wave vibrator data. To compare the diffraction section from the vibrator data with the one from the sledgehammer data, we select only vibrator shots whose positions coincided with those of the sledgehammer source.

Figure 3.3a shows a typical raw common-source gather using the sledgehammer as a source, while Figure 3.4a shows an example of a shot gather using the vibrator at the same lateral location, after cross-correlation of the raw vibrograms with the source-monitor signal. The pre-processing steps for these two gathers are identical: trace editing, statics corrections, geometrical-spreading correction, and band-pass filtering. In addition, automatic gain control (AGC) with a window length of 30 ms is applied to both raw gathers for display purposes. Due to the soft soil condition in the near-surface, we notice that the raw data are dominated by the presence of strong SWs (white ellipses in Figure 3.3a and Figure 3.4a). These SWs make the identification of weak diffraction events nearly impossible. To reveal the scattered energy, we apply the scheme that we have described in chapter 2 to attenuate the high-amplitude SWs. The data after surface-wave suppression are shown in Figure 3.3b and Figure 3.4b, respectively, where the yellow ellipses indicate some meaningful scattered events caused by small objects in the subsurface. We make such interpretations based on the negative moveouts of these events and consistently similar locations as revealed in two different datasets. Figure 3.5 illustrates the two final diffraction sections obtained from the hammer and vibrator data (after surface-wave suppression) using our new imaging approach. The velocity range we use for diffraction summation is from 120 ~ 140 m/s, with a step of 5 m/s. We obtain this velocity range using the asymptotic approach proposed by Shtivelman et al. [2009]. In Figure 3.5, the vertical axis indicates the approximate depth in meters, which is converted using the subsurface velocity of 130 m/s. High-amplitude anomalies (blue or light blue colour in Figure 3.5) indicate the locations of potential buried objects of archaeological importance.

Earlier in a separate work, archaeologists collected samples from closely spaced shallow boreholes at this site. These samples indicate that the burial mound consists of sand and gravel in the shallow part down to around 3 m. Based on these samples, a cross-section of the subsurface of Mound B4749 was made, and is illustrated in Figure 3.6. The vertical axis in Figure 3.6 indicates depth in meters above the Amsterdam Ordnance Datum (Normaal Amsterdams Peil or NAP). In Figure 3.6, two distinguished features (primary mound and secondary mound) can be identified and are interpreted as mounds constructed at different periods. A magnetic survey [Lambers et al., 2017] was also carried out at this site, where strong thermoremanent magnetization at the range of $\pm 5 \sim 8$ nT was detected. This anomalous value was probably caused by high temperatures, and indicates the existence of burnt stones inside this mound. From the magnetic map of this area, the possible location of pits containing burnt stones was interpreted, which is illustrated by the yellow ellipse in Figure 3.6, at a height of about 30 m NAP, while

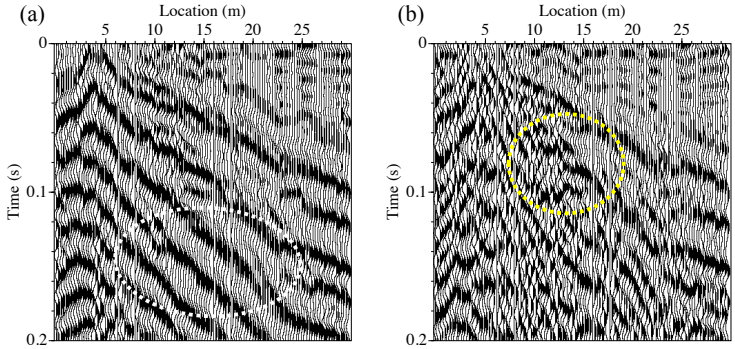

Figure 3.3: (a) A shot gather contaminated by strong SWs (white ellipse) acquired in the field using sledgehammer as a source. The source is located at 4 m lateral position. (b) The same shot gather after surface-wave suppression using a scheme described in chapter 2. Note that events with negative moveout (yellow circle in Figure 3.3b) can now be identified.

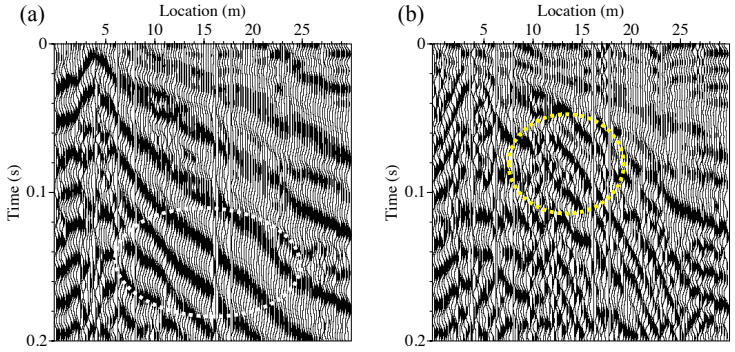

Figure 3.4: As in Figure 3.3, but for seismic data acquired in the field using a shear-wave vibrator source.

its lateral location is centered around 15 m. Due to the strong impedance contrast at this location compared to the surrounding medium, the seismic response from these stones can be recorded as diffraction events. In our diffraction sections, anomalies located at a lateral position around 15 m (yellow ellipse in Figures 3.5a, b) can be identified. These positions seem to agree with the locations of the burial pits indicated in Figure 3.6. For other deeper prominent anomalies in our diffraction sections, we cannot find direct indications in the core profile because of the limited depth of the shallow boreholes. These anomalies need to be verified through further checks.

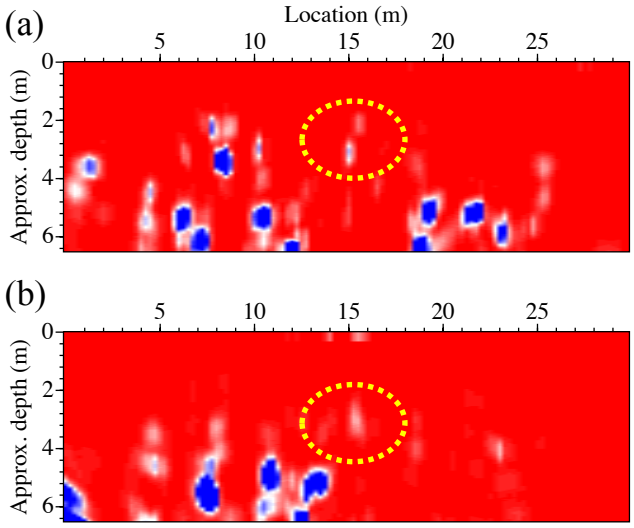

Figure 3.5: Diffraction imaging result obtained from seismic data after surface-wave suppression: (a) sledge-hammer data; (b) shear-wave vibrator data.

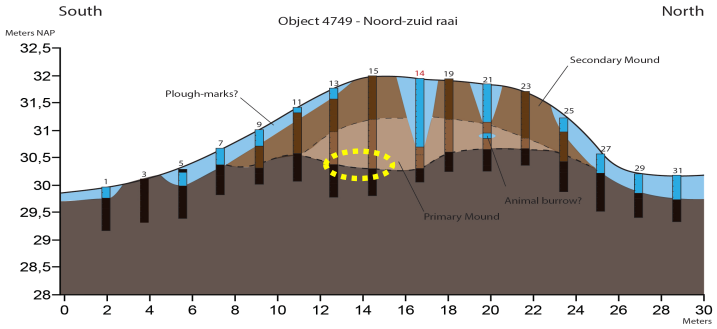

Figure 3.6: Drawing of the same burial mound based on information of borehole samples. The lateral axis is the same as in Figure 3.5. The vertical axis indicates the height in meters using Amsterdam Ordnance Datum system (NAP). The location of a burial pit detected by magnetometry survey [Lambers et al., 2017] is marked by the yellow ellipse.

3.4. DISCUSSION AND CONCLUSIONS

Diffraction imaging is inherently a 3D problem because diffracted waves caused by scattering objects propagate in all directions. When the seismic data is acquired along a line below which the target objects are distributed, the imaging of such targets is reliable. If

this is not the case, the location of the diffractors will be estimated at the wrong depths, and/or the quality of imaging will be heavily deteriorated, due to the lack of diffraction energy captured by the receivers. For the archaeological site that we investigated, the borehole profile already shows that the shallow subsurface up to 3 m depth is composed of finer sand and gravelly soils, which can be considered as a very heterogeneous media for the used seismic wavelengths. The wavefield containing information from local heterogeneities under our 2D seismic line could be acquired; the buried objects manifest as events with negative moveouts (e.g., yellow circles in Figure 3.3b and Figure 3.4b). This makes it possible to map the distribution of heterogeneities at this archaeological site using our 2D diffraction-imaging method.

The seismic data acquired at this site is dominated by strong surface waves (SWs). To increase the reliability of the diffraction imaging, a technique that consists of seismic interferometry (SI) and adaptive subtraction (AS) is first applied to the data for the suppression of high-amplitude surface-wave noise in a data-driven way. Weak diffractions from the subsurface objects become identifiable after this procedure. These diffractions can be input to our diffraction-imaging algorithm for locating the local, buried objects. Our diffraction-imaging method is based on the optimal summation of seismic diffractions from these objects. An amplitude-unbiased coherency method is used to suppress the incoherent summation of noise, to enhance the weak and coherent diffracted signals. The stacking procedure results in a section where diffractions are emphasized and the remaining SWs are further suppressed. This diffraction section can be useful for reliable identification of the local heterogeneities. We demonstrate the reliability of the proposed diffraction imaging method using synthetic and field data.

4

AN INTERFEROMETRIC WORKFLOW FOR NEAR-SURFACE DIFFRACTOR DETECTION

Continuing with the previous chapter, in this chapter, we propose an extended approach for imaging subsurface objects using masked diffractions. These masked diffractions are first revealed by a combination of seismic interferometry (SI) and nonstationary adaptive subtraction (AS), and then further enhanced through crosscoherence-based supervirtual interferometry (SVI). A diffraction image is then computed by a spatial summation of the revealed diffractions. We use phase-weighted stacking (PWS) to enhance the coherent summation of weak diffraction signals. Using synthetic data, we show that our scheme is robust in locating diffractors from data dominated by strong Love waves. We test our method on field data acquired at an archaeological site. The resulting distribution of shallow diffractors agrees with the location of anomalous objects identified in the V_S model obtained by elastic SH/Love full-waveform inversion using the same field data. The anomalous objects correspond to the position of a suspected burial, also detected in an independent magnetic survey and corings.

The main contents of this chapter have been published in *Geophysics*, 2021, **86:** WB1-WB11 [Liu et al., 2021]. For consistency, minor changes have been made. Note that the content of this chapter has some overlaps with that of the previous chapter.

4.1. INTRODUCTION

Archaeology is the study of past human cultures through the analysis and interpretation of artifacts and material remains [Smith, 2014]. The material remains, which possess certain physical properties (e.g., elastic impedance) that contrast with the subsurface background medium, can be detected using non-invasive near-surface geophysical surveys, and more specifically with the seismic methods. For detecting small, localized objects, the usual normal-moveout stacking is generally not useful, because traditional common-midpoint moveout corrections are only optimal for reflection events. Although common-offset gathers can potentially show such objects more reliably [Ghose et al., 1998], these gathers focus on the primary reflected waves and mostly ignore the diffracted waves. The conspicuous appearance of diffracted waves can be utilized to locate an object buried in the heterogeneous subsurface at an archaeological site. However, the amplitude of these diffracted events is usually weak [Klem-Musatov, 1994] and difficult to detect in field seismic data, due to the usually dominant presence of other coherent events like surface waves (SWs) and specular reflections.

Several methods have been developed to detect various near-surface buried features using diffracted waves. Landa and Keydar [1998] developed an algorithm to construct a so-called D-section by concentrating the diffracted signals spread from diffractor points. In this D-section, high-amplitude anomalies indicate the existence of local heterogeneities. Shtivelman and Keydar [2005] presented a multipath summation approach to stack diffracted signals along all possible diffraction trajectories for shallow inhomogeneities detection. Kaslilar et al. [2013] proposed an approach inspired by seismic interferometry (SI) to estimate the location of a near-surface tunnel by traveltime inversion of crosscorrelated diffracted arrivals. The crosscorrelation procedure eliminates the common raypath between the source and the subsurface diffractor. This makes the traveltime dependent only on properties between the receivers and the diffractors.

In this chapter, we introduce a workflow for imaging subsurface objects using masked diffractions, i.e., weak diffractions covered by other signals. This workflow consists of three main steps. We first reveal masked diffractions by suppression of the dominant Love waves through a combination of SI and nonstationary adaptive subtraction (AS) [Dong et al., 2006; Halliday et al., 2007; Konstantaki et al., 2015a; Liu et al., 2018]. We then enhance the revealed weak diffraction signal through crosscoherence-based supervirtual interferometry (SVI) [An and Hu, 2016; Dai et al., 2011; Nakata et al., 2011; Place et al., 2019]. Finally, a diffraction image, which can be used to interpret the locations of subsurface diffractors, is generated by a spatial summation [Landa et al., 2006; Shtivelman and Keydar, 2005; Shtivelman et al., 2009] of enhanced diffractions.

In the following, we first describe the theory of each of the above-mentioned steps. We then illustrate the feasibility of our approach in detecting near-surface objects using synthetic seismic data dominated by Love waves. Finally, we test our workflow on field seismic data acquired at an archaeological site in Veluwe, the Netherlands, to map the distribution of shallow diffractors of archaeological importance.

4.2. METHODOLOGY

In this section, we present a workflow (Figure 4.1) for near-surface diffractor detection from data dominated by strong SWs (in our case Love waves), which consists of three main steps. These steps include surface-waves suppression by SI+AS, diffraction enhancement through SVI, and diffraction imaging. Below, we present the theory of each of these steps.

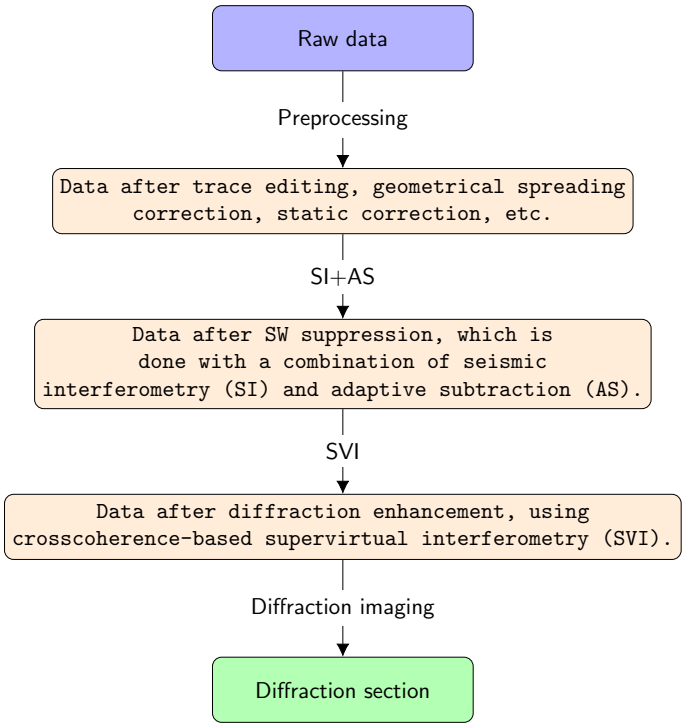

Figure 4.1: Flowchart for raw-data processing for diffraction imaging. To reveal weak diffractions, a combination of SI and AS is first used to suppress dominant SWs. A crosscoherence-based SVI is then applied to further enhance the diffractions.

4.2.1. SI+AS FOR SURFACE-WAVES SUPPRESSION

SI refers to a process of retrieving the seismic response between two receivers by cross-correlating and integrating the wavefields recorded at these receivers from a boundary of sources [Schuster, 2009; Wapenaar et al., 2008]. When the sources are located along the Earth's surface, the response retrieved by SI would be dominated by SWs [Dong et al., 2006; Halliday et al., 2007]. The dominance of SWs is observed in passive seismology (e.g., [Shapiro, 2005]), exploration seismology (e.g., [Balestrini et al., 2019; Dong et al., 2006]), and near-surface seismology (e.g., [Konstantaki et al., 2015b]). Depending on the source type (passive or active), the retrieval steps for SI are different. In the context of

this chapter, we focus only on active-source SI.

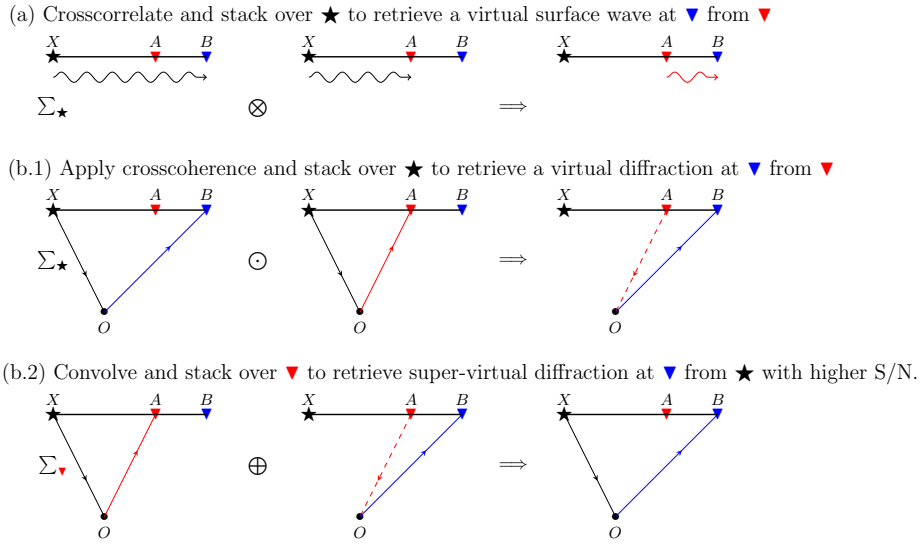

Figure 4.2: (a) The step for retrieving dominant SWs between two receivers by SI. (b1), (b2) The steps for creating super-virtual diffractions with an increased S/N. Note that the surface-wave component can also be retrieved/enhanced by the SVI step. Hence, it is beneficial to apply SVI for diffraction enhancement only after the suppression of the dominant SWs. $\otimes$, $\odot$, $\oplus$ denote crosscorrelation-, crosscoherence-, and crossconvolution-based operators, respectively. $\rightsquigarrow$ represents SWs propagating along the surface from an active source to the receivers. $\rightarrow$ denotes the propagation of diffracted waves from an active source to the receivers.

The steps of inter-receiver surface-wave retrieval using active sources are illustrated in Figure 4.2a. In Figure 4.2a, $\rightsquigarrow$ represents SWs propagating along the Earth's surface from an active source to the receivers. By crosscorrelating the trace recorded at receiver **A** with that at **B**, we obtain a virtual trace at **B** as if caused by a virtual source located at **A**. The traveltime of the signal in this virtual trace is denoted as τ_{AB} (red $\rightsquigarrow$ in Figure 4.2a), and it is independent of the source position as long as the source falls inside the stationary-phase region [Snieder, 2004]. For this reason, the virtual trace at **B** from each of the sources can be stacked constructively to give the inter-receiver estimate of the SWs propagating from **A** to **B**. Mathematically, it can be formulated in the frequency domain as [Halliday et al., 2007; Wapenaar and Fokkema, 2006]

$$C_{X_B X_A} = \sum_{i=1}^{N} u^*(X_A, X_i)\, u(X_B, X_i). \tag{4.1}$$

In equation 4.1, $C_{X_B X_A}$ represents inter-receiver SWs propagating from **A** to **B** retrieved by SI. The seismic data generated by a source at X_i and recorded by receivers at X_A and X_B are denoted as $u(X_A, X_i)$ and $u(X_B, X_i)$, respectively. The superscript $*$ indicates complex conjugation. N is the number of active sources available for stacking. If we ignore the presence of noise, in the frequency domain the seismic wavefield can also be represented by the multiplication of a source wavelet and a Green's function:

$$u(X, X_i) = W(X_i)G(X, X_i), \tag{4.2}$$

where $W(X_i)$ is the spectrum of the source wavelet generated by the source located at X_i and $G(X, X_i)$ denotes the Green's function between X_i and X. Substituting equation 4.2 into equation 4.1, we have

$$C_{X_B X_A} = |W|^2(X_i) \sum_{i=1}^{N} G(X_A, X_i)G^*(X_B, X_i). \tag{4.3}$$

To accurately retrieve the amplitude of the seismic response using equation 4.3, according to the theory, the sources should effectively surround the receivers and illuminate them homogeneously, the source boundary should be a sphere with a sufficiently large radius, and the medium should be lossless [Draganov et al., 2006; Wapenaar and Fokkema, 2006]. For conventional 2D near-surface seismic surveys, this requirement cannot be fulfilled because active sources are placed only at the surface and usually along the line connecting the receivers (this limitation is also true for 2D seismic surveys at the exploration scale); thus, the retrieved SWs will be characterized by amplitude errors.

To account for the amplitude difference between the retrieved SWs and the dominant SWs from the physical active source, a matching filter (see Appendix A) is estimated via the regularized nonstationary regression technique proposed by Fomel [2009]. This is done by using shaping regularization Fomel [2007] to constrain the continuity and smoothness of the filter coefficients. The retrieved SWs are then convolved with this estimated matching filter and subsequently subtracted from the field data.

4.2.2. SVI FOR DIFFRACTION ENHANCEMENT

After the suppression of the dominant surface waves, the hidden diffraction events may become identifiable. To further enhance the diffraction energy, we use SVI [Dai et al., 2011]. The principle of SVI consists of two steps and is illustrated in Figure 4.2b. First, the traces recorded at receivers **A** and **B** are crosscorrelated. The common raypath from the source to a subsurface object (black straight line) is subtracted, thus the traveltime of the obtained virtual diffraction can be denoted as $\tau_{OB} + \tau_{OA}$. This traveltime is the same for all active-source positions of a survey, so stacking the virtual diffraction at **B** from N sources will enhance its S/N by a factor of $\sqrt{N}$ assuming uncorrelated noise. Next, SI by convolution is applied [Slob et al., 2007] and the stacked virtual diffraction is convolved with an actual trace originally recorded at a receiver position **A** from the source at **X** to produce a super-virtual trace at **B**. This super-virtual trace represents the seismic response from a subsurface diffractor, recorded by receiver **B** from the source positioned at **X**. The super-virtual trace is kinematically equivalent (with traveltime equal to $\tau_{XO} + \tau_{OB}$) for all receiver positions **A** located between the source **X** and receiver **B**. Thus, the retrieved super-virtual traces at N receiver positions **A** could be stacked to obtain a final trace with S/N increased again by as much as $O(\sqrt{N})$.

In this chapter, we use crosscoherence instead of crosscorrelation (similar to equation 4.1) to retrieve the virtual diffraction $H_{X_B X_A}$ [Nakata et al., 2011; Place et al., 2019]:

$$H_{X_B X_A} = \sum_{i=1}^{N} \frac{u(X_A, X_i)u^*(X_B, X_i)}{|u(X_A, X_i)||u^*(X_B, X_i)| + \eta} = \sum_{i=1}^{N} \frac{G(X_A, X_i)G^*(X_B, X_i)}{|G(X_A, X_i)||G^*(X_B, X_i)| + \eta}, \tag{4.4}$$

where η is a small number for stabilizing the division, and $|\cdot|$ indicates that the amplitude spectrum is used. If we consider the effect of the source wavelet, which is denoted by $W(X_i)$, a virtual diffraction obtained by crosscorrelation will contain an amplitude factor proportional to $|W|^2(X_i)$ (see equation 4.3). The corresponding super-virtual diffraction will then include an amplitude factor proportional to $|W|^3(X_i)$, due to the additional convolution involved in the second step. This $|W|^3(X_i)$ factor may lead to wavelet distortion of the enhanced diffractions. On the other hand, SI by crosscoherence (equation 4.4) eliminates (theoretically) the contribution of the source wavelet $W(X_i)$ and makes the virtual diffraction contain only the medium response. The resulting super-virtual diffraction will then contain an amplitude factor proportional to $W(X_i)$, which avoids wavelet distortion and thus improves the precision of the reconstructed diffractions.

4.2.3. DIFFRACTION IMAGING

The diffractions that are revealed by SI+AS and enhanced by SVI can now be used for detecting near-surface diffractors. We design a diffraction algorithm (based on studies from Landa and Keydar [1998] and Shtivelman and Keydar [2005]) to coherently focus the diffraction energy back to its original position; all other events in the shot-gather domain will be suppressed by the used directional summation. Such a procedure will make the true diffractions appear as high-amplitude anomalies in the resulting sections, which can be used to indicate the locations of diffractors.

Consider a seismic wave emitted from a source X_0 (Figure 4.3). When it encounters a subsurface diffractor along its propagation path, it would generate a secondary wave that spreads from this point in all directions. In Figure 4.3, X_i is the image point and Ω denotes the diffracted wavefront element surrounding this image point. We assume that the velocity variations are small and the propagation distance between source and receiver is relatively short so that the diffracted wavefronts can be approximated as an arc of a circle with a radius of R. This radius R has a specific physical meaning, which is the depth of the diffractor below the image point. Thus, the kinematic response (T_{SR}) of the diffractor defined in equation 3.1 can be rewritten as [Landa and Keydar, 1998]:

$$T_{SR} = \frac{\sqrt{(X_0 - X_i)^2 + R^2} + \sqrt{(X_k - X_i)^2 + R^2}}{V_0} - \frac{2R}{V_0} + 2t_d, \tag{4.5}$$

where V_0 is the average velocity of the medium above the diffractor, t_d is the vertical time above the diffractor. X_0, X_i, X_k denote the lateral positions of the source, image point, and receiver, respectively.

If we know the exact value of R (the depth of the diffractor), a diffraction image can be obtained by stacking seismic energy along the diffraction surface defined by equation 4.5. If the value of R is unknown, it can be estimated by maximizing the semblance function [Taner and Koehler, 1969] calculated from seismic records within a time window along the traveltime surface defined by equation 4.5 (similar to the traditional

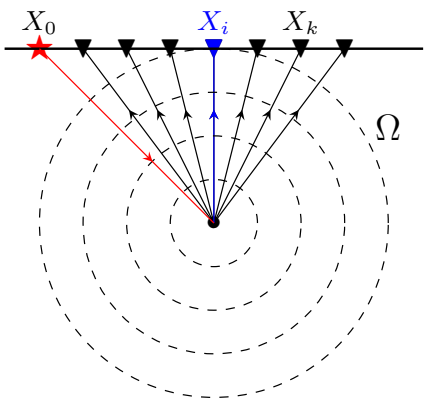

Figure 4.3: Schematic view of diffracted waves. X_0, X_i, X_k denote the lateral position of the source (red star), image point (blue triangle), and receiver (black triangle), respectively. Ω is the diffracted wavefront element surrounding the image point (blue triangle at lateral position X_i).

velocity analysis). The alternative approach for diffraction imaging, not requiring the specification of the radius R, is the multipath summation [Shtivelman and Keydar, 2005; Shtivelman et al., 2009]. This is done by stacking seismic energy (with unit weights) along diffraction trajectories defined by equation 4.5, calculated for various values of R within a specified range. The resulting diffraction image would be close to the one produced by stacking with the correct radius, due to the constructive and destructive interference of the amplitudes contributing along each diffraction trajectory.

The practical implementation steps of this diffraction-stacking method include the following. For a specific common-source gather, we first assume that the diffractor is located directly under the first receiver and the depth of the diffractor is known as R. This will define a specific diffraction traveltime curve according to equation 4.5. Next, we obtain a diffraction-moveout corrected gather by applying a diffraction-moveout correction to this common-source gather. Such a traveltime correction is repeated for all other combinations of source-receiver pairs. We then resort these moveout-corrected common-source gathers into the common-receiver domain and stack traces within each common-receiver gather to produce one single trace per receiver position. To enhance coherent summation of weak diffraction signals, a phase-weighted stacking (PWS) (see Appendix B) method is used. The stacked traces from each common-receiver gather are then assembled into a diffraction image [Landa and Keydar, 1998; Liu et al., 2019]. For better visualization of high-amplitude anomalies, we produce the final diffraction image using a coherency measure calculated from each diffraction image resulting from different R. The coherency measure we choose is the unnormalized crosscorrelation sum [Neidell and Taner, 1971], due to its high sensitivity to coherent weak signals. This coherency function (C) can be expressed as

$$C = \sum_{t} \left\{ \left[\sum_{i=1}^{M} f_{i,t(i)} \right]^2 \right\}, \tag{4.6}$$

where $f_{i,t(i)}$ denotes the amplitude value of the ith trace at two-way traveltime $t(i)$, and M is the number of traces. The outer summation is performed over the two-way zero-offset time samples t within a time gate. The length of the gate should be approximately equal to the main wavelength of the seismic signal.

4.3. SYNTHETIC TEST

To verify the effectiveness of our method for near-surface diffractor detection, we first test it on data from 2D synthetic modelling. The model shown in Figure 4.4 is an S-wave velocity (V_S) model. This model consists of two layers. The first layer has a lower velocity (100 m/s) and thickness of 0.5 m. Below this layer, we place a high-velocity (150 m/s) half-space. Two circular diffractors are also embedded in the model at a depth of 5 m. These diffractors have a certain impedance contrast with respect to the background medium. The diamter of these diffractors is 1.0 m. The receiver array, which is located at the surface, consists of 40 geophones aligned in the horizontal direction from 10 m to 29.5 m at an interval of 0.5 m. During data generation, the receiver array is kept fixed, while the source, also deployed at the surface, advances at a step of 1 m. The first source is located 5 m to the left of the first geophone, while the last source is placed 4.5 m to the right of the last geophone. With this acquisition geometry, 30 common-source gathers are computed using an elastic 2D SH finite-difference (FD) algorithm [Bohlen, 2002; Dokter et al., 2017]. We discuss the reason for choosing SH-wave processing in the field-example section. At the top boundary, a free-surface boundary condition is realised by the image technique [Robertsson, 1996] for accurate SH-wave modelling. For the other boundaries, Convolutional perfectly matched layers (C-PML) absorbing boundary conditions are used [Komatitsch and Martin, 2007]. The source signature is a band-limited spike with center frequency at 40 Hz.

4.3.1. REVEALING WEAK DIFFRACTIONS

Figure 4.5a shows an example of the synthetic shot gathers for the source located at horizontal position 13 m, i.e., at the seventh receiver. This shot gather (Figure 4.5a) is dominated by dispersive Love waves, because of the presence of the high-velocity half-space in the velocity model. The amplitudes of the diffracted waves in Figure 4.5a, which represent the seismic response from the diffractors embedded in the model in Figure 4.4, are so weak that it is difficult to identify them directly.

Before we introduce our SI+AS scheme for the suppression of Love waves, we first apply conventional frequency-wavenumber ($f-k$) filtering to eliminate the dominant Love waves, while preserving the weak diffraction signals. Figure 4.6a displays the $f-k$ spectrum of the synthetic gather from Figure 4.5a. We can see that this spectrum is dominated by two clusters of Love-wave energy (black arrows). We design a fan filter to reject the Love-wave energy in the $f-k$ domain (Figure 4.6b). This is followed by inverse mapping back to the shot-gather domain. As shown in the resulting filtered shot gather (Figure 4.7a), weak diffraction signals begin to be identifiable, due to the significant sup-

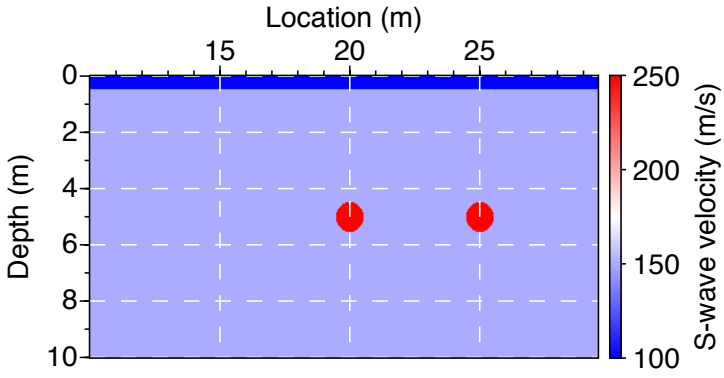

Figure 4.4: S-wave velocity (V_S) model used to generate the synthetic common-source gathers. Two shallow diffractors with a given impedance contrast with respect to the background media are included in the model.

pression of the Love waves. However, we can still observe some remaining Love waves (red box in Figure 4.7a). This is because Love waves and diffractions are not well separated in the $f-k$ domain (Figure 4.6a) due to their similar apparent velocities. Thus, it is hard to design an efficient fan filter, which can completely reject the Love-wave energy while preserving the diffraction events.

We then make use of SI to compute a virtual common-source gather for the receiver positioned at 13 m (this receiver becomes the virtual source), following the scheme presented in Figure 4.2a. As shown in Figure 4.5b, the main kinematic characteristics of the Love waves in Figure 4.5a are retrieved well. However, due to the source term $W^2(X_i)$ involved in the SI procedure (equation 4.3), the wavelet of the Love waves in Figure 4.5b is broader than that in Figure 4.5a. Further, the interferometric approximation used in equation 4.3, such as elastic media and active sources distributed only at the surface, causes the amplitude of the estimated Love waves in Figure 4.5b to be erroneous compared to the amplitude of the Love waves in the original shot gather in Figure 4.5a.

To account for amplitude, phase, and frequency differences between Figure 4.5a and Figure 4.5b, a matching filter is estimated via the regularized nonstationary regression technique proposed by Fomel [2007]. Figure 4.5d shows the mean coefficients of the matching filter determined by minimizing the difference between Figure 4.5a and Figure 4.5b in the least-squares sense. From Figure 4.5d, we can see that the filter coefficients vary in both time and space, which agrees well with the variability of the original shot gather (Figure 4.5a). We then convolve the estimated matching filter (Figure 4.5d) with Figure 4.5b to compensate for the amplitude, phase, and frequency distortions in Figure 4.5b that we mentioned earlier, which leads to the result presented in Figure 4.5c. Comparing Figure 4.5a with Figure 4.5c, we can now see that the dominant Love waves in Figure 4.5c and Figure 4.5a match very well. Next, we subtract Figure 4.5c from Figure 4.5a, which gives the result shown in Figure 4.7b. As shown in Figure 4.7b, two diffraction events with negative moveouts can now be easily recognized. This is due to the significant suppression of Love waves in Figure 4.5a through the SI + AS procedure (Fig-

ure 4.2a).

During the procedure of AS, the dominant Love waves dictate the parameters of the matching filter, and hence these waves will be most effectively suppressed. The weak diffraction signals might also be affected, but to a lesser extent. As shown in Figure 4.7b, certain parts of diffractions which overlap with the Love wave are also regarded as Love-wave energy by this algorithm (Figure 4.2a) and suppressed. To recover this lost diffraction energy and further enhance the amplitude of the diffraction events, we then apply SVI to the data as in Figure 4.7b, obtaining results as shown in Figure 4.7c. For comparison, we also show a reference shot gather (Figure 4.7d) containing only the seismic response from the diffractors. This shot gather is obtained by taking the difference of synthetic data modelled with and without the diffractors. This process removes any arrivals other than the diffractions. Comparing Figure 4.7c with Figure 4.7b, we can see that the diffractions in Figure 4.7c show more complete moveouts (see blue boxes in Figure 4.7b and 4.7c), and their apices are recovered well.

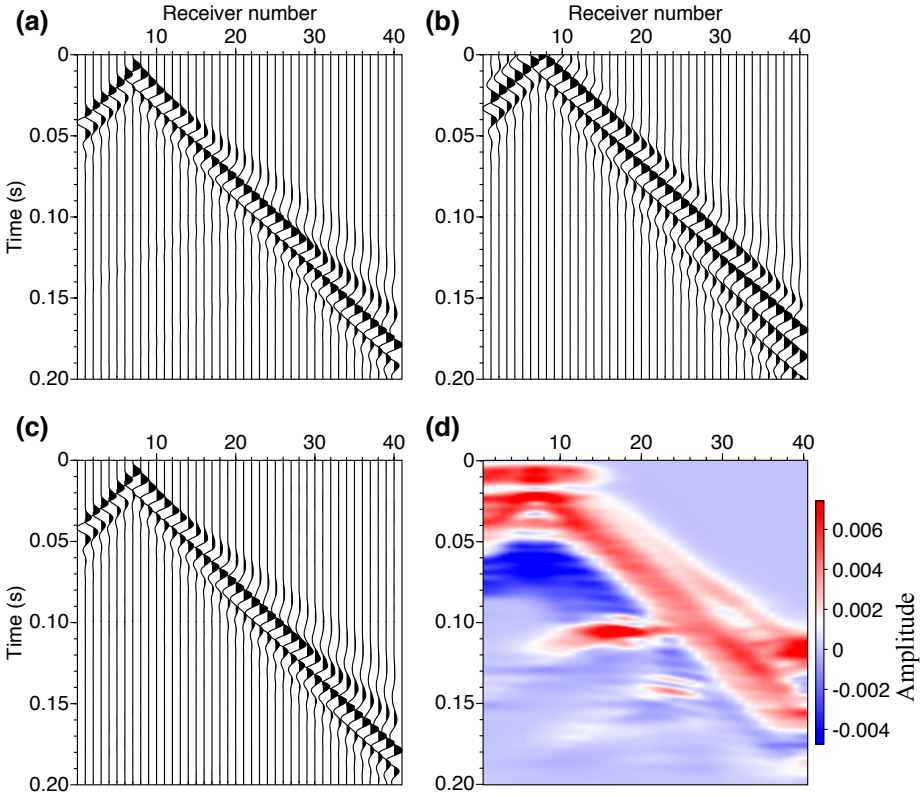

Figure 4.5: Steps for revealing weak diffractions dominated by strong Love waves. (a) A synthetic SH shot gather computed for the model shown in Figure 4.4; (b) retrieved Love waves from the gather as shown in Figure 4.5a; (c) result after convolution of the data in (b) with the matching filter (d); (d) mean filter coefficients estimated by minimizing the difference between (a) and (b), using the regularized non-stationary regression method.

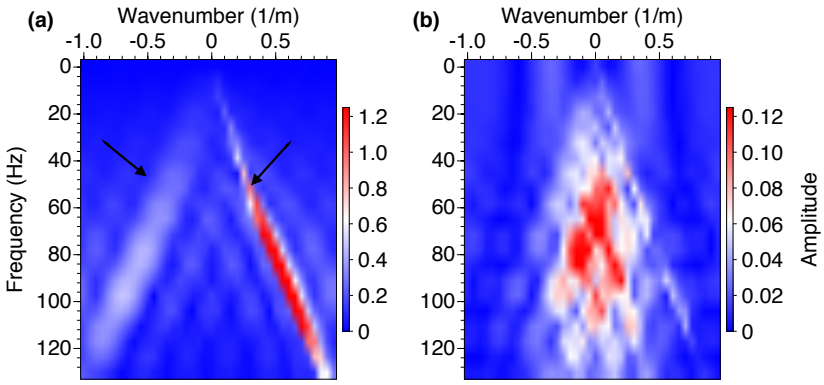

Figure 4.6: (a) The $f-k$ spectrum of the synthetic SH shot gather from Figure 4.5a; (b) the $f-k$ spectrum of the same shot gather, but after rejecting Love-wave energy indicated by the black arrows in (a).

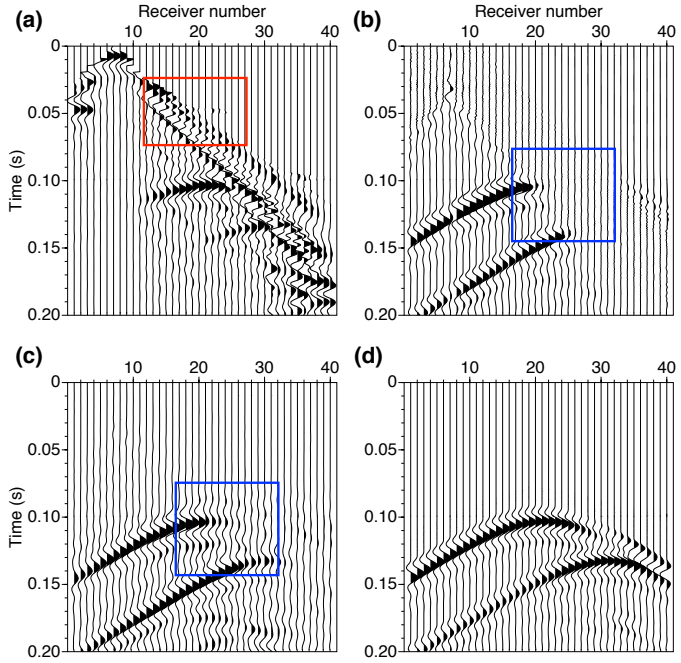

Figure 4.7: (a) Result after Love-wave suppression in the data in Figure 4.5a by $f-k$ filtering; (b) result after AS of Figure 4.5b from Figure 4.5a; (c) result after applying SVI to the result in (b) for diffraction enhancement; (d) reference shot gather showing only diffracted arrivals obtained from subtraction of modelled data using models with and without diffractors.

4.3.2. DIFFRACTION IMAGING

We now apply our diffraction-focusing approach to the data shown in Figure 4.7, i.e., after the suppression of the Love waves by different approaches, which gives the corresponding diffraction images (Figure 4.8). In this figure, the horizontal axes show the lateral location (in m) as shown in Figure 4.4, while the vertical axes denote the approximate depth (in m) that we derive using an average velocity ($V_0 = 150$ m/s) from the model in Figure 4.4. We also use this average velocity ($V_0 = 150$ m/s) in equation 4.5 to describe the moveouts of possible diffractions. The range of R (depth of potential diffractors) used for diffraction stacking is from 0.5 m to 8 m with a step of 0.5 m. Such a range covers the area of interest for near-surface diffractor detection. To mitigate the near-field effects as much as possible, we mute early arrivals before producing the final diffraction images.

Figures 4.8a–4.8c represent the diffraction images from the data after Love-wave elimination by the $f-k$ filtering, SI+AS, and SI+AS+SVI, respectively. Every second common-source gathers is used. We apply phase-weighted stacking (PWS) to enhance the coherent summation of weak signals. From Figures 4.8a–4.8c, we can clearly identify two prominent anomalies (red color). We interpret the maximum amplitudes of these anomalies as the centers of the detected diffractors, whose lateral locations agree well with those of the objects embedded in the synthetic model (Figure 4.4). There are some errors in the estimated depths of the detected diffractors (depths estimated around 6 m). This can be explained by the fact that a constant velocity ($V_0 = 150$ m/s) may not be accurate enough to describe the travel path of diffracted waves and hence may cause errors in the estimated depths. Note that the shapes of the anomalies in Figures 4.8a–4.8c do not necessarily indicate the actual shapes of the true objects in Figure 4.4. Figures 4.8d–4.8f show diffraction images as in Figures 4.8a–4.8c, respectively, but using all modelled common-source gathers. We show this result to investigate the effect of the number of common-source gathers on the resolution of the diffraction images. We can see that having half as many sources did not affect the resolution of the obtained diffraction images. This is very encouraging for field applications, where due to operational reasons sparser source points would be available. In the field data example below, we have sources every 2 m. Figures 4.8g–4.8i show diffraction images as in Figures 4.8d–4.8f, respectively, but using linear stack for weak diffraction summations. We can see that the resolution of the anomalies in Figures 4.8d–4.8f is higher than in Figures 4.8g–4.8i. This is because PWS is more efficient for incoherent-noise reduction than linear stack, thus reducing the amount of incoherent noise present in the resulting diffraction image.

4.4. FIELD EXAMPLE

4.4.1. SITE OVERVIEW

In 2017, we acquired seismic data at the Epe-Niersen barrow alignment, an archaeological site located in the Veluwe, the Netherlands. With our survey, we wanted to obtain more information about such monuments (burial mounds) using non-invasive geophysical methods, including seismic imaging, to minimize or even eliminate the need for excavation. To do that, we investigated one burial mound from the Epe-Niersen barrow alignment, which is known as Mound 4749 [Bourgeois, 2012].

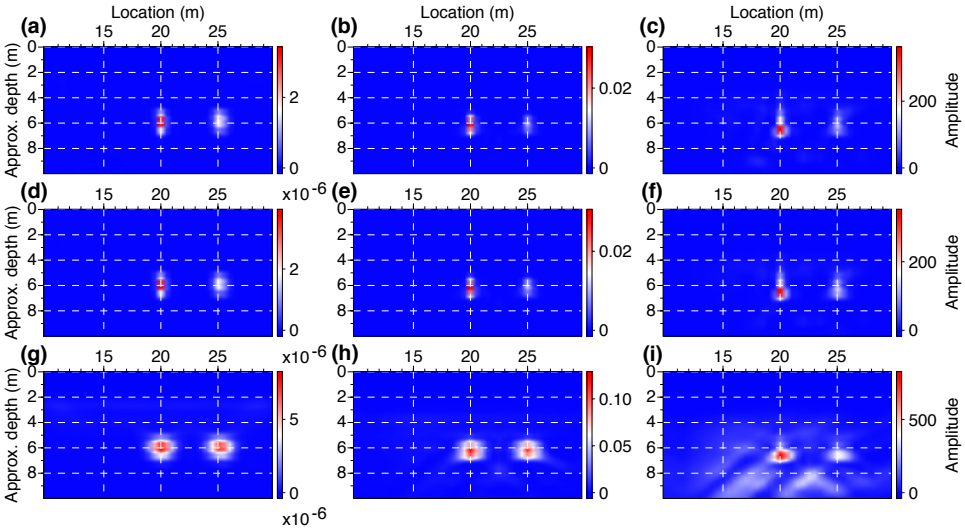

Figure 4.8: Comparison of results from diffraction imaging by different approaches. (a),(b),(c) diffraction imaging of the data after Love-wave suppression by $f-k$ filtering, SI+AS, and SI+AS+SVI, respectively. Every second common-source gather is used. PWS is applied to enhance the coherent summation of weak diffraction signals. (d),(e),(f) Similar to (a), (b), (c), but using all the modelled common-source gathers. (g), (h), (i) Similar to (d), (e), (f), but ordinary, linear stack is used to stack the weak diffraction signals.

4.4.2. SEISMIC-DATA ACQUISITION

We carried out a seismic survey over the top of Mound 4749. We used two kinds of active sources — a sledgehammer and a high-frequency S-wave vibrator [Brouwer et al., 1997; Ghose et al., 1996] — to excite seismic waves that are then recorded by horizontal, 10-Hz single-component geophones. The horizontal geophones were oriented in the crossline direction, while the active sources (hammer and vibrator) were used in the SH mode, i.e., also oriented in the crossline direction. Under such an acquisition system, we can generate and record SH-waves.

We used SH-waves because they have several main advantages over P-waves. The first advantage is that they can offer a higher resolution of subsurface structures than P-waves, given the same frequency content. This is due to the relatively low propagation velocity of SH-wave in soft soils and ensuing wavelength. The second benefit of SH-waves, compared to P-waves is that they are directly linked to the small-strain rigidity and hence quite sensitive to subtle changes in the subsoil mechanical properties [Ghose, 2003; Ghose et al., 2013; Ghose and Goudswaard, 2004]. Another advantage is that when SH-waves encounter a diffractive object in the subsurface, the diffracted wavefield will mainly consist of SH-wave diffractions. For P-waves, however, such discontinuity will cause a complex diffracted wavefield, which includes P-P, P-SV, SV-P, and SV-SV diffractions. Of all these diffraction modes, the SH-wave diffractions have the largest amplitude and most coherent phase characteristic along the traveltime hyperbola, making them advantageous for diffraction imaging [Lellouch and Reshef, 2017; Peterie et al., 2020]. Our receiver array consists of 120 geophones planted with a 0.25 m interval. During data

acquisition, we kept this receiver array fixed and moved only the source at an interval of 2 m. The first source position was at 4 m to the left of the first geophone, while the last source position was at 4 m to the right of the last geophone. At each source position, four recordings were acquired and stacked to yield one common-source gather. This was done to reduce the source-incoherent noise and increase the S/N of the recorded data.

4.4.3. NEAR-SURFACE DIFFRACTORS DETECTION

Figure 4.9a shows a typical raw SH-wave common-source gather when using the sledgehammer source, in this case at a lateral position of 0 m. Figure 4.9b shows an example shot gather when using the vibrator as a source at the same source position, after cross-correlation of the raw vibrograms with the estimated groundforce [Ghose, 2002]. The main preprocessing steps that we apply to these two types of seismic data are trace editing, top muting, statics corrections, geometrical-spreading correction, trace normalization, and band-pass filtering (5−80 Hz). Due to the soft-soil condition in the near surface of our study area, we can see that the raw seismograms (Figure 4.9a and Figure 4.9b) are dominated by distinct, dispersive Love waves. The strong presence of these Love waves makes it hard to identify the diffraction events, if they exist, directly from the raw data. To reveal possible weak diffracted energy, these dominant Love waves have to be suppressed while the diffraction events should also be preserved.

To attenuate the Love waves, we first retrieve the dominant Love-wave energy from the preprocessed data by SI in a data-driven way, as explained above, and then adaptively subtract the retrieved result from the raw data (Figures 4.9a and 4.9b), i.e., we apply SI+AS which leads to the results shown in Figures 4.9c and 4.9d, respectively. Comparing the latter with the respective gathers illustrated in Figures 4.9a and 4.9b, some meaningful diffraction events caused by heterogeneities in the subsurface (e.g., red circles in Figures 4.9c and 4.9d) can be identified. To further enhance these diffracted events and suppress other coherent signals, we then apply SVI to the data as shown in Figures 4.9c and 4.9d. The results are shown in Figures 4.9e and 4.9f, respectively. As in the synthetic example (Figure 4.6), Love waves and masked diffraction signals in the preprocessed data (Figures 4.9a and 4.9b) map to the similar regions in the $f-k$ domain. In such cases, it is hard to design an efficient filter to suppress the Love waves and preserve the weak diffractions at the same time. Because of this fact, we choose not to apply conventional $f-k$ filtering to suppress Love waves in the field data.

Figure 4.10 illustrates the four final diffraction images obtained from the hammer and vibrator datasets (after SI+AS, SI+AS+SVI) using our diffraction-focusing approach described in the Methodology section 4.2. The average velocity that we use for diffraction stacking is 90 m/s. We base this velocity value on the results from an iterative full-waveform inversion (FWI) algorithm [Tarantola, 1984; Virieux and Operto, 2009]. Note that the diffraction-focusing approach does not require detailed subsurface information, but assumes a homogeneous value characteristic of the velocity close to the surface (V_0 in equation 4.5). This assumption is only valid at sites with gradual velocity variation. Figure 4.11 shows the inverted V_S model by elastic SH/Love using the hammer data. From the velocity model (Figure 4.11) obtained by, we think that here the near-surface (< 1.0 m) is quite homogeneous laterally and can be, on average, described by a single velocity (V_0 = 90 m/s). We stack the diffraction events in the shot domain over diffractor

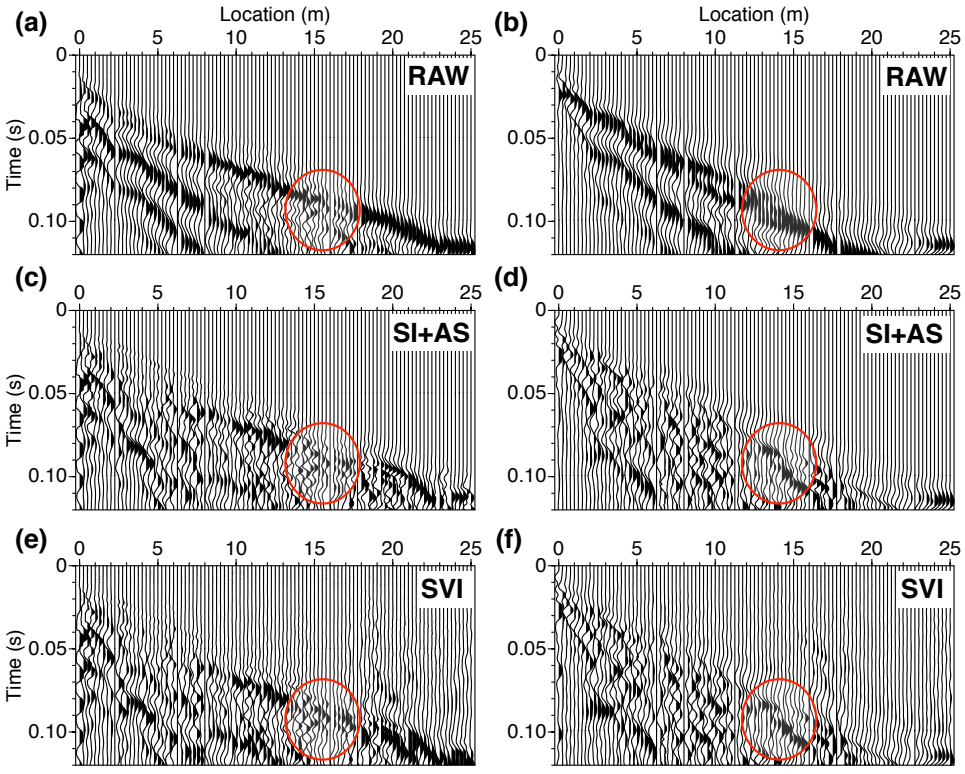

Figure 4.9: (a) A typical preprocessed SH-wave shot gather from the field data acquired using a sledgehammer source. The gather is dominated by strong Love waves. (c) Result after Love-wave suppression by SI+AS; (e) result after diffraction enhancement by SVI; (b),(d),(f) are the same as (a),(c),(e), but using S-wave vibrator as the source. The first 101 traces are displayed.

depths from 0.5 m to 5.0 m (R in equation 4.5), which mainly covers the depth range of our interest in the shallow subsurface. In Figure 4.10, the horizontal axes show lateral locations of the receiver array that we deployed over the Mound 4749, while the vertical axes indicate the approximate depth (in m) converted from time using an average velocity of 90 m/s.

Figures 4.10a and 4.10c display diffraction images obtained from sledgehammer and S-wave vibrator data after Love-wave suppression by SI+AS. Figures 4.10b and 4.10d represent diffraction images from sledgehammer and S-wave vibrator data after Love-wave suppression by SI+AS and diffraction enhancement by SVI. Two clusters of high-amplitude anomalies (indicated by ellipses) can be identified at similar positions (around 15 m and 22 m horizontal distance) in these four diffractions images. From the V_S model (Figure 4.11) obtained by, we can see that areas at similar positions also show high-velocity (blue ellipses) contrasts with the background medium. These facts give us more confidence to interpret these distinct anomalies (ellipses in Figure 4.10) as potential

buried objects of archaeological importance.

In an earlier separate field work, a magnetic survey was conducted at this site [Lambers et al., 2017]. This survey detected magnetic anomalies in the range of ±5 ~ 8 nT, which is nearly the strongest value among their measurements made within the mound. The configuration of the anomalies and their position within the burial mound suggest these are probably traces of a burial underneath the mound. Additional corings also confirm the place of a pit at this position — most likely a grave. Earlier excavations of burial mounds in the direct vicinity of this mound have found evidence for large stones that were incorporated within the structure of the graves [Bourgeois et al., 2009]. The high-amplitude anomalies detected in our diffraction images (Figure 4.10) might correspond to such stones.

During a seismic survey, when seismic waves encounter such stones, the waves would be diffracted due to the strong impedance contrast of the stones with the background medium. In the shot gathers after SI+AS and SI+AS+SVI, we can identify diffraction events (red circles in Figure 4.9), with apices located at around 15 m horizontal distance. However, the diffraction event at around 22 m horizontal distance is not recognizable in the shot gathers. A possible explanation is that the S/N of this diffraction is still low in them. However, after a coherent summation of this weak diffraction in the following diffraction-stacking procedure, its amplitude becomes strong enough and can be easily identified in the final diffraction images (dashed ellipses in Figure 4.10). Comparing the diffraction images from data after SI+AS and SI+AS+SVI, we can see that the high-amplitude anomalies in SI+AS+SVI diffraction image (ellipses in Figures 4.10b and 4.10d) seem to be more easily identifiable than those in the SI+AS diffraction image (ellipses in Figures 4.10a and 4.10c).

4.5. DISCUSSION

When a propagating seismic wave encounters a subsurface object or a velocity perturbation of size comparable to the wavelength, it will be diffracted. For a 2D seismic survey, the imaging of the target objects is reliable only when the seismic data are acquired along a line above such targets. If this is not the case, the imaging of diffractors will be negatively affected (spatially smeared or estimated at a wrong location).

In the modelled example, we saw that $f-k$ filtering could damage the desired diffraction arrivals. In our case, it indeed resulted in such damage to the right sides of the diffractions (Figure 4.7a). Still, the energy at and around the apices of the diffractions was preserved, and the diffraction stacking gave good results, possibly even better than the results from our proposed methodology. Figure 4.7b (and the filter in Figure 4.5d) show that SI+AS had damaged the diffraction apices with the result of less strong diffraction stacking. The application of SVI partly compensated for that and thus the diffraction stacking produced better results. Note that this is also a result of the modelling, as the diffractions are relatively strong and thus the SI step retrieves not only the dominant Love waves, but also the apices of the diffractions. In the case of the field data, the diffraction events are not clear at all. In such cases, the damaging effect of the $f-k$ filter on diffraction events, which map into the same region in the $f-k$ domain as the Love-wave energy, would lead to a lower diffraction-stacking image. Contrary to this, our proposed methodology, making use of a data-driven Love-wave suppression and diffraction-event

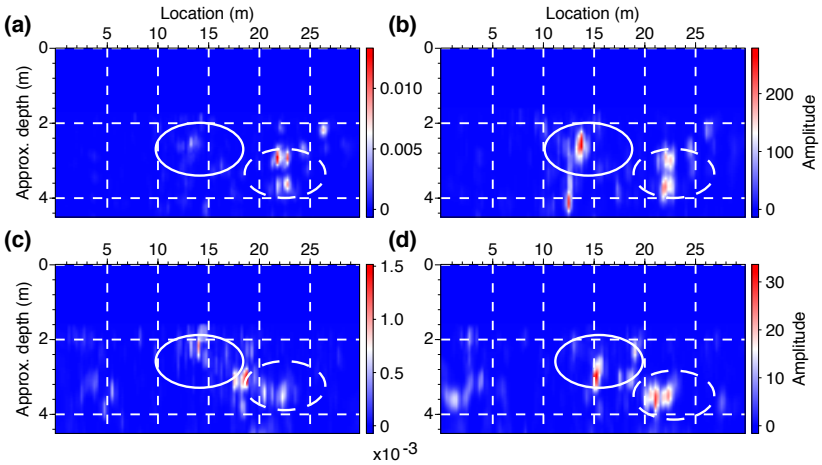

Figure 4.10: Diffraction imaging result obtained from the field seismic data following our proposed workflow 4.1: (a) sledgehammer data after Love-wave suppression by SI+AS; (b) sledgehammer data after Love-wave suppression by SI+AS and diffraction enhancement by SVI; (c), (d) are same as (a), (b) but using S-wave vibrator data. High-amplitude anomalies (solid and dashed ellipses) indicate the potential locations of subsurface diffractor-like objects.

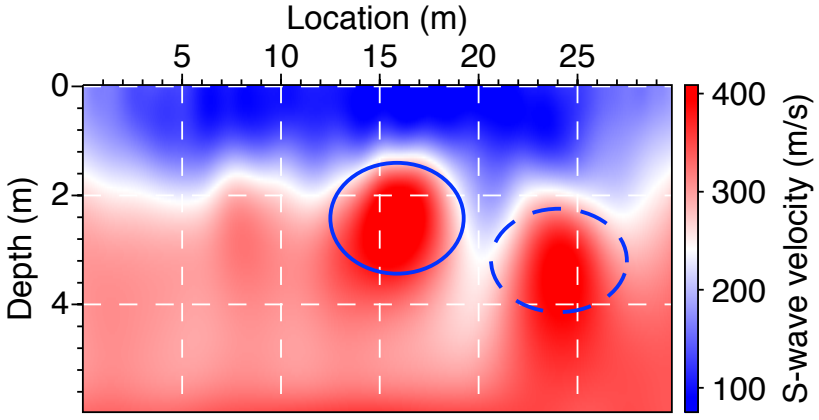

Figure 4.11: Two-dimensional subsurface V_S model obtained by elastic full-waveform inversion of the sledgehammer data.

enhancement through SI+AS+SVI, would not result in damage but in enhancement, and thus would produce a better diffraction-stacking image.

The two datasets corresponding to two different seismic sources, sledgehammer and S-wave vibrator, used in this study were independently acquired and processed. The

horizontal locations of diffractors are well-constrained by surface seismic methods [Peterie et al., 2020]. The very close lateral locations of the diffractors derived from the diffraction focusing applied on SI+AS and SI+AS+SVI processed datasets (Figure 4.10) validate our interpretation regarding the presence of these diffractors and their approximate lateral locations. The estimated depths of the detected diffractors have inherent uncertainty and are connected to the average velocity V_0 in equation 4.5. Assuming a constant velocity may not be enough to describe the travel path of the diffracted waves, especially at sites with strong lateral or vertical velocity variations. This may contribute to errors in the estimated depths. The estimated depth information of the detected diffractors could be verified by other geophysical methods (such as core profiling) once their horizontal locations are determined.

After Love-wave suppression and diffraction enhancement, diffraction events (red ellipses in Figure 4.9) with clear apices could be identified. These diffraction events are representative of subsurface heterogeneities, and are useful to map the distribution of buried objects at an archaeological site. However, as mentioned above, a diffraction image can only indicate the approximate location of the subsurface objects. To obtain a more complete picture regarding the subsurface objects of archaeological importance, the use of 2D near-surface FWI could be an important option, which is the main content of the next chapters.

4.6. CONCLUSIONS

In this chapter, we presented a workflow for imaging shallow subsurface objects represented by weak diffractions hidden behind dominant surface waves (SWs) (in our case Love waves). Our workflow included three main steps. The masked diffractions were first revealed after the suppression of the dominant Love waves. This was done by retrieving the Love waves in a data-driven way by seismic interferometry (SI) and then adaptively subtracting them from the raw data. Secondly, we enhanced the revealed weak diffraction signals further through crosscoherence-based super-virtual interferometry (SVI). Thirdly, we produced a diffraction section by a spatial summation of the revealed diffraction energy, where no specific velocity for the subsurface was needed. We introduced phase-weighted stacking to enhance the coherent summation of weak diffraction signals. Using synthetic data, we illustrated that our workflow is robust in detecting and imaging weak diffractions. We applied our workflow on seismic datasets acquired in an archaeological site using two different active seismic sources. Our results showed two prominent diffraction objects in the subsurface at our test location. Our workflow had the potential to be used to map the spatial locations of shallow heterogeneities in near-surface seismic surveys, when no detailed subsurface velocity is available.

5

CHARACTERIZING NEAR-SURFACE STRUCTURES BASED ON INSTANTANEOUS-PHASE COHERENCY INVERSION

Traditional least-squares full-waveform inversion (FWI) suffers from severe local minima problems in case of the presence of strongly dispersive surface waves. Additionally, recorded wavefields are often characterized by amplitude errors due to varying source coupling and incorrect 3D-to-2D geometrical-spreading correction. Thus, least-squares FWI is considered less suitable for near-surface applications. We introduce an amplitude-unbiased coherency measure as a misfit function that can be incorporated into FWI. Such coherency was earlier used in phase-weighted stacking (PWS) to enhance weak but coherent signals. The benefit of this amplitude-unbiased misfit function is that it can extract information uniformly for all seismic signals (surface waves, reflections, and scattered waves). Using the adjoint-state method, we show how to calculate the gradient of this new misfit function. We validate the robustness of the new approach using checkerboard tests and synthetic data contaminated by random noise. We then apply the new FWI approach to a field dataset acquired at an archaeological site located in Ostia, Italy. The goal of this survey was to map the unexcavated archaeological remains with high resolution. We identify a known tumulus in the FWI results. The instantaneous-phase coherency FWI results also establish that the shallow subsurface under the survey lines is quite heterogeneous. The instantaneous-phase coherency FWI of near-surface data can be a promising tool to image shallow small-scale objects buried under shallow soil covers, as found at archaeological sites.

The main contents of this chapter has been published in *Geophysics*, 2022, **87(4):** 1–50 [Liu et al., 2022]. For consistency, minor changes have been made.

5.1. INTRODUCTION

In recent years, 2D elastic full-waveform inversion (FWI) has evolved into a promising tool for various near-surface investigations. Tran et al. [2013] developed a 2D time-domain Gauss-Newton-based FWI and applied it for the detection of a sinkhole. The same approach has also been used in the investigation of roadway subsidence by Tran and Sperry [2018]. Dokter et al. [2017] and Pan et al. [2019] applied 2D time-domain FWI to estimate the near-surface S-wave velocity structure by inverting recorded Love waves. Groos et al. [2017] applied 2D time-domain FWI to recorded shallow seismic wavefields. They successfully inverted Rayleigh waves and demonstrated the potential of 2D FWI in the reconstruction of shallow small-scale structures.

Apart from the above-mentioned examples, the field-data application of 2D FWI for near-surface prospecting is still not very common. As pointed out by Virieux and Operto [2009], one principal challenge that limits the potential application of seismic FWI to near-surface characterization is how to define the proper minimization criteria to reduce the sensitivity of FWI to amplitude errors. Amplitude errors might be caused by inconsistent coupling effects at different source and receiver positions [Kamei et al., 2015; Maurer et al., 2012], non-uniform source amplitudes excited at different shot locations, noise, and inaccurate 3D-to-2D correction of the geometrical-spreading effects [Forbriger et al., 2014]. If the amplitude information of the recorded wavefields is not reliable, the inverted results from FWI would be questionable. Therefore, geophysicists are trying to use phase information to constrain the subsurface structures in a more stable way [Bozdağ et al., 2011; Luo et al., 2018; Mao et al., 2019; Yuan et al., 2020].

Phase information (instantaneous phase, $\phi(t)$) contains the kinematic properties of the wavefields and has a great potential to tackle the above-mentioned challenge. Fichtner et al. [2008] proposed an FWI approach based on the separation of phase and amplitude information in the time-frequency domain. By reducing the interaction between phase and amplitude, their method reduces non-linearities in FWI. Bozdağ et al. [2011] developed a similar concept but in the time domain, which avoids additional processing when compared with the time-frequency domain approach of Fichtner et al. [2008]. However, the instantaneous-phase measurements involved in these approaches suffer from phase wrapping. Phase unwrapping is a challenging task, especially for noisy data [Yuan et al., 2020]. To avoid the phase-wrapping problem, an alternative way is to implicitly measure the phase in the complex seismic traces. Luo et al. [2018] defined a misfit function based on the exponential phase difference ($e^{i\phi(t)}$) between observed and synthetic data. Subsequently, Yuan et al. [2020] analysed the advantages and disadvantages of a misfit function based on the exponential phase difference.

In this chapter, we propose a new misfit function based on the exponential phase to measure the coherency between measured and synthetic data. Using the theory of complex trace analysis, we show how to construct such a coherency measure from the exponential phase of the data, which is explicitly independent of the amplitude. This makes it possible to extract information uniformly for all components of seismic signals (surface waves, reflections, and scattered waves). Such a coherency measure is inspired by the concept of phase-weighted stacking (PWS) as proposed by Schimmel and Paulssen [1997] for weak but coherent signal detection. In the PWS, an amplitude-unbiased coherency is estimated from the exponential phase, which is then used to enhance the

stacking of signals with similar instantaneous phase.

In the following sections, we first present the theory of FWI based on instantaneous-phase coherency. Through numerical examples, we validate the effectiveness of the new approach using checkerboard tests and synthetic data with random noise. Finally, we test our new approach on field data recorded at an archaeological site located in Ostia, Italy.

5.2. METHODOLOGY

We first describe the basic theory of the instantaneous-phase coherence, which is used to measure the similarity between two signals. After reviewing the basic theory of FWI, we present the details on how to calculate the gradient of the misfit function based on instantaneous-phase coherency using the adjoint-state method [Plessix, 2006; Tarantola, 1984; Tromp et al., 2004].

5.2.1. INSTANTANEOUS-PHASE COHERENCE

The PWS method is an efficient technique, first proposed by Schimmel and Paulssen [1997], to reduce incoherent noise from the data. This method permits the detection of weak but coherent signals. An amplitude-unbiased coherency measure is employed to enhance components of stacked signals that share the same instantaneous phase. We extended the use of such instantaneous-phase coherency measure in a misfit function, which can be incorporated in FWI. Following the notation of Schimmel and Paulssen [1997], a complex trace $S(t)$ can be constructed by ascribing a seismic trace $s(t)$ to the real part of $S(t)$ and the Hilbert transform of $s(t)$ to the imaginary part of $S(t)$:

$$S(t) = s(t) + i\mathcal{H}\{s(t)\}. \tag{5.1}$$

The complex trace $S(t)$ in equation 5.1 can also be written in following form:

$$S(t) = A(t)e^{i\phi(t)}, \tag{5.2}$$

where $A(t)$ is the instantaneous amplitude which can be obtained as:

$$A(t) = \sqrt{s^2(t) + \mathcal{H}^2\{s(t)\}}, \tag{5.3}$$

and $\phi(t)$ is the instantaneous phase, and it can be calculated as follows:

$$\phi(t) = \arctan\frac{\mathcal{H}\{s(t)\}}{s(t)}. \tag{5.4}$$

However, the arc-tangent operator in equation 5.4 can cause a serious phase-wrapping problem [Bozdağ et al., 2011; Yuan et al., 2020]. To avoid this, the instantaneous phase is implicitly estimated as:

$$e^{i\phi(t)} = \frac{S(t)}{A(t)} = \frac{s(t) + i\mathcal{H}\{s(t)\}}{\sqrt{s^2(t) + \mathcal{H}^2\{s(t)\}}}. \tag{5.5}$$

Schimmel and Paulssen [1997] defined the *phase stack* as a coherency measure, where amplitudes of the complex traces are not involved. The amplitude of the *phase stack*

ranges between zero and one. If the instantaneous phases of all traces are perfectly coherent, then the corresponding value of the *phase stack* equals one. If the instantaneous phases of all traces vary significantly, the *phase stack* will be approximately zero.

Based on these principles and also on the phase cross-correlation concept presented in Schimmel et al. [2010], we define the following coherency measure that can be directly incorporated as a misfit function used in FWI:

$$J(t) = \frac{1}{4}\left\{\left|e^{i\phi_1(t)} - e^{i\phi_2(t)}\right|^2 - \left|e^{i\phi_1(t)} + e^{i\phi_2(t)}\right|^2\right\}, \tag{5.6}$$

where $\phi_1(t)$ and $\phi_2(t)$ denote the instantaneous phase of the observed and the synthetic seismic traces, respectively. In the complex plane, the amplitude of $J(t)$ can be represented by the difference (subtraction) between the length of the black vector and that of the blue vector shown in Figure 5.1. When two signals have significantly different instantaneous phases (Figure 5.1a), the amplitude of $J(t)$ has a positive value close to one. If the two signals have a similar instantaneous phase (Figure 5.1b), the amplitude of $J(t)$ has a negative value close to minus one. Therefore, $J(t)$ can be used in FWI as a misfit function to iteratively update the model parameters till the value of $J(t)$ is minimum, which will imply that the instantaneous phases of the observed and the synthetic data are then similar.

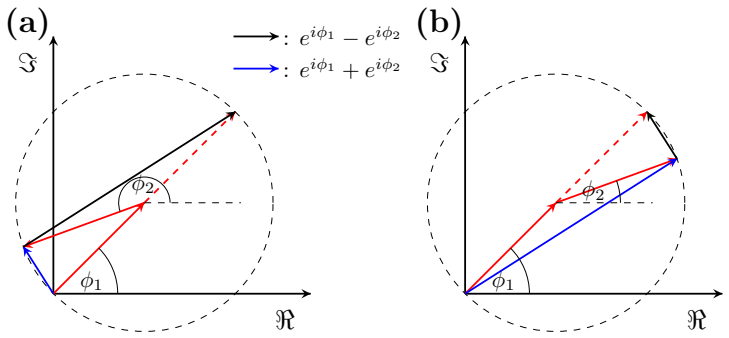

Figure 5.1: Illustrations of instantaneous-phase coherency as defined in equation 5.7. The red arrows denotes $e^{i\phi_1}$ and $e^{i\phi_2}$, whereas the black and blue arrows represent $e^{i\phi_1} - e^{i\phi_2}$ and $e^{i\phi_1} + e^{i\phi_2}$, respectively. The black arrow measures how the instantaneous phases of two signals are close to each other, while the blue arrow measures how much the instantaneous phases of two signals differ from 180 degrees. Either of the two measurements can be used on its own as a misfit function of FWI by matching the instantaneous phase between the measured and the synthetic data. Using numerical experiments (not shown in this chapter), we found that the performance of different misfit functions (black arrow, blue arrow, combination of black and blue arrows) is quite similar. The reason why we design a misfit function with a combination of black and blue arrows is that this approach is novel and it has the chance to be more robust to noise. $J(t)$ is obtained by subtracting the square of the two vectors given by the black and the blue arrows. (a) When the two signals have significantly different instantaneous phases, $J(t)$ will be close to 1. (b) When the two signals have similar instantaneous phases, $J(t)$ will be close to -1.

Using the theory of complex analysis, equation 5.6 can also be written as

$$J(t) = \frac{1}{2}\left\{\sin^2\left(\frac{\phi_1(t)-\phi_2(t)}{2}\right) - \cos^2\left(\frac{\phi_1(t)-\phi_2(t)}{2}\right)\right\}, \tag{5.7}$$

where $\phi_1(t)$ and $\phi_2(t)$ are the instantaneous phases of the measured and the synthetic data, respectively. Note that equation 5.7 also suffers from local minima problem as conventional least-squares FWI, meaning that $\phi_1(t)-\phi_2(t)$ should be less than π to avoid the cycle-skipping problem. However, our misfit function mainly focuses on matching the instantaneous phase between the measured and synthetic data, which indicates that it would be robust to amplitude errors and thus it is suitable for field-data applications.

We now illustrate why our approach is robust to amplitude errors. For this purpose, we analyse Gaussian signals. In Figure 5.2a, the black line denotes a Gaussian signal with a peak frequency of 5 Hz, while the red dashed line represents the same Gaussian signal with 10% random noise. Figure 5.2b illustrates the instantaneous phase of the two signals shown in Figure 5.2a. Compared with the instantaneous phase of a clean Gaussian signal (black line in Figure 5.2b), we encounter obvious phase-wrapping effects for the noisy Gaussian signal (red dashed line in Figure 5.2b). Figures 5.2c and 5.2d show the real and imaginary parts of the exponentiated phase of the Gaussian signal with and without random noise, respectively. Comparing Figures 5.2c and 5.2d with Figure 5.2b, we notice that the exponentiated phase is more robust to random noise. Thus, the exponentiated phase makes FWI based on the instantaneous-phase coherency advantageous in handling noisy field data that contain also amplitude errors.

5.2.2. OVERVIEW OF FWI

FWI consists of a forward-modeling step to generate the synthetic data and a nonlinear inversion process to update the model parameters by minimizing a chosen misfit function which is a measure of the difference between the synthetic and the recorded data. Using the adjoint-state method [Plessix, 2006; Tarantola, 1984; Tromp et al., 2004], the gradient of the misfit function with respect to the model parameters can be effectively computed through zero-lag crosscorrelation of a forward wavefield with the adjoint wavefield generated by back-propagating the residual wavefield at each receiver simultaneously. A gradient-based method, such as the nonlinear conjugate gradient (NLCG), can then be used to solve iteratively the nonlinear inverse problem.

The classic FWI formulation [Tarantola, 1984] uses the misfit function in the form of least-squares norm of the residuals between measured and synthetic data, which can be written as:

$$J_1(t) = \frac{1}{2}\sum_{s,r}\int_0^T \left(d_1(\mathbf{x_s},\mathbf{x_r},t) - d_2(\mathbf{x_s},\mathbf{x_r},\mathbf{m},t)\right)^2 dt, \tag{5.8}$$

where $\sum_{s,r}$ represents summation over all available sources and receivers, T is the recording time, $d_1(\mathbf{x_s},\mathbf{x_r},t)$, $d_2(\mathbf{x_s},\mathbf{x_r},\mathbf{m},t)$ are, respectively, measured and synthetic data at a receiver $\mathbf{x_r}$ from a source at $\mathbf{x_s}$, and $\mathbf{m}$ denotes the model parameters. In the following, to avoid clutter, we omit the dependency of the recorded and synthetic wavefields on $\mathbf{x_s}$, $\mathbf{x_r}$, $\mathbf{m}$. The gradient of the misfit with respect to the model parameters can then be written as:

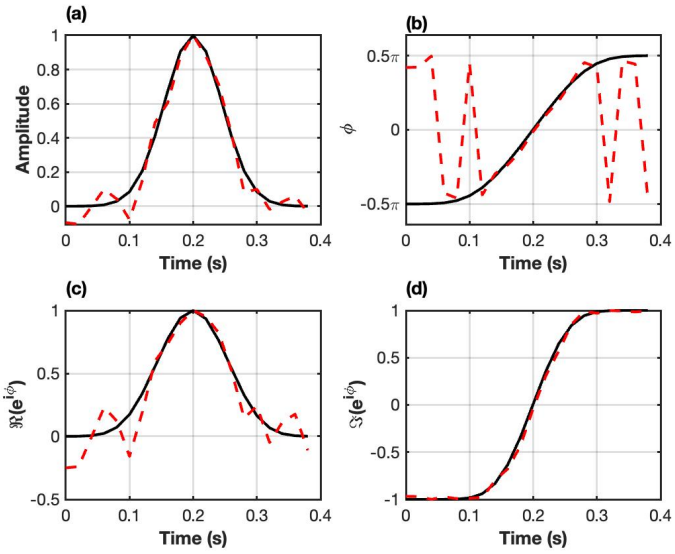

Figure 5.2: A simple synthetic example to demonstrate the robustness to noise of instantaneous phase ($\phi(t)$) and exponentiated phase ($e^{i\phi(t)}$). (a) A Gaussian signal with a peak frequency of 5 Hz (black line) and the same Gaussian signal with random noise and S/N = 10 (red-dashed line). In (b), (c), (d), we use black and red-dashed lines to represent respectively the instantaneous phase and exponentiated phase of the two signals presented in (a). (b) The instantaneous phase of the two signals as presented in (a). Note that for the signal with random noise, there are marked phase jumps. (c) The real part of the exponentiated phase of the two signals presented in (a). (d) The imaginary part of the exponentiated phase of the two signals presented in (a). Comparing (c), (d) with (b), it is clear that the exponentiated phase is more robust to noise.

$$\delta J_1 = \sum_{s,r} \int_0^T -\big(d_1(t) - d_2(t)\big)\delta d_2(t)\,dt = \sum_{s,r} \int_0^T r(t)\delta d_2(t)\,dt, \tag{5.9}$$

where $\delta d_2(t)$ denotes the perturbation of the synthetic wavefield due to a model perturbation $\delta\mathbf{m}$, and $r(t)$ is the residual wavefield.

The gradient of the misfit function in equation 5.9 can implicitly be calculated by the adjoint-state method [Tarantola, 1984; Tromp et al., 2004], which includes the following steps: (1) forward-propagating the source wavefield, (2) back-propagating the residual wavefield, and (3) computing the zero-lag crosscorrelation of the forward-propagated and the back-propagated wavefields.

5.2.3. INVERSION WITH INSTANTANEOUS-PHASE COHERENCY

Based on the instantaneous-phase coherence defined in equation 5.7, we define the following misfit function for use in FWI:

$$
\begin{aligned}
J_2(t) &= \frac{1}{4}\sum_{s,r}\int_0^T \left\{ \left| e^{i\phi_1(t)} - e^{i\phi_2(t)} \right|^2 - \left| e^{i\phi_1(t)} + e^{i\phi_2(t)} \right|^2 \right\} dt \\
&= \frac{1}{4}\sum_{s,r}\int_0^T \left| \frac{d_1(t) + i\mathcal{H}\{d_1(t)\}}{\sqrt{d_1^2(t) + \mathcal{H}^2\{d_1(t)\}}} - \frac{d_2(t) + i\mathcal{H}\{d_2(t)\}}{\sqrt{d_2^2(t) + \mathcal{H}^2\{d_2(t)\}}} \right|^2 dt \\
&- \frac{1}{4}\sum_{s,r}\int_0^T \left| \frac{d_1(t) + i\mathcal{H}\{d_1(t)\}}{\sqrt{d_1^2(t) + \mathcal{H}^2\{d_1(t)\}}} + \frac{d_2(t) + i\mathcal{H}\{d_2(t)\}}{\sqrt{d_2^2(t) + \mathcal{H}^2\{d_2(t)\}}} \right|^2 dt, \qquad (5.10)
\end{aligned}
$$

where $e^{i\phi_1(t)}$ and $e^{i\phi_2(t)}$ are the exponential phase (equation 5.5) of the measured and the synthetic data, respectively. The derivative of the misfit function with respect to the model parameters is expressed as (see Appendix C for details):

$$
\begin{aligned}
\delta J_2 &= \sum_{s,r}\int_0^T \left[\frac{d_2(t)\mathcal{H}\{d_1(t)\}\mathcal{H}\{d_2(t)\}}{A_1(t)A_2^3(t)} - \frac{d_1(t)\mathcal{H}^2\{d_2(t)\}}{A_1(t)A_2^3(t)} \right] \delta d_2(t)\, dt \\
&+ \sum_{s,r}\int_0^T \left[\mathcal{H}\left\{ \frac{d_2^2(t)\mathcal{H}\{d_1(t)\}}{A_1(t)A_2^3(t)} - \frac{d_1(t)d_2(t)\mathcal{H}\{d_2(t)\}}{A_1(t)A_2^3(t)} \right\} \right] \delta d_2(t)\, dt \\
&= \sum_{s,r}\int_0^T \tilde{r}(t)\delta d_2(t)\, dt. \qquad (5.11)
\end{aligned}
$$

where $A_1(t)$ and $A_2(t)$ denote the instantaneous amplitude (equation 5.3) of the measured and the synthetic data, respectively. The gradient in equation 5.11 is similar to that in equation 5.9 except for a different residual wavefield $\tilde{r}(t)$. To compute this new gradient, we back-propagate the residual wavefield $\tilde{r}(t)$ instead of $r(t)$, while the other steps involved in calculating the gradients are identical to the classic least-squares FWI approach described above.

5.3. SYNTHETIC TESTS

In this section, we validate the robustness of the FWI based on the instantaneous-phase coherency, using checkerboard tests and synthetic data containing random noise.

5.3.1. RESOLUTION TEST

We use checkerboard models (Figures 5.3a and 5.3b) with anomalies of different sizes to assess the near-surface resolution capability of FWI based on instantaneous-phase coherency. The background of these models is homogeneous, with V_P = 1000 m/s, V_S = 300 m/s and ρ = 2000 kg/m^3. We create anomalies only in the V_S model; the anomalies are such that they have ±10 % (± 30 m/s) deviation from the background velocity. The checkerboard anomalies are of size 5 m × 2.5 m and 2.5 m × 2.5 m (Figures 5.3a and 5.3b). The receiver array, which is located at the surface, consists of 41 vertical geophones with a spacing of 1 m between x = 5 m and x = 45 m. During data generation, the receiver

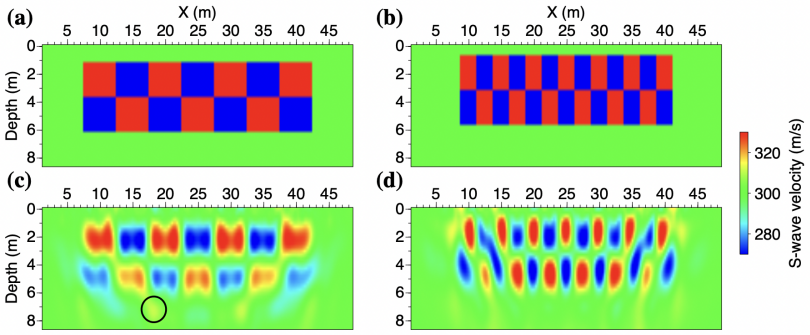

Figure 5.3: Checkerboard tests for resolution analysis. (a) True V_S model containing velocity anomalies. The size of these anomalies is 5 m × 2.5 m; (c) the result of instantaneous-phase coherency FWI. (b), (d) the same as in (a), (c) but for anomalies with size of 2.5 m × 2.5 m. A homogeneous background (V_S = 300 m/s) is used in all tests. The black circle indicates an artifact caused by the FWI algorithm.

5

array is kept fixed whereas a vertical-force source, also deployed at the surface, moves every 2 m. The sources are located between x = 10 m and x = 40 m. With this acquisition geometry, 16 common-source gathers are computed. During the simulation, we use a band-limited spike (10 ~ 60 Hz) as the source wavelet. For this case, the approximate resolution using Rayleigh criterion [Kallweit and Wood, 1982] can be in the range of 1.25 ~ 7.5 m (i.e., $0.25 * 300/60 \sim 0.25 * 300/10$ m).

We perform a monoparameter inversion where only the V_S model is updated/interpreted, which is because the dominant Rayleigh wave in the data is highly sensitive to the V_S model [Groos et al., 2017]. We use the background model with V_P = 1000 m/s, V_S = 300 m/s, and ρ = 2000 kg/m^3 as the initial model for all inversion tests. The source wavelet is assumed to be known. A minimum of eleven iterations is performed during the inversion stage. The inversion stops once the improvement in the relative misfit change becomes smaller than 1% between two consecutive iterations [Pan et al., 2019]. This also serves as a stopping criterion for other inversion tests performed in this research. The reconstructed V_S models by the instantaneous-phase coherency FWI are shown in Figures 5.3c and 5.3d. The anomalies are reconstructed very well. This illustrates the resolution capability of the instantaneous-phase coherency FWI. For the anomalies below the lateral positions 10 and 40 m, there are some smearing effects caused by the limited source-receiver illumination.

5.3.2. ROBUSTNESS TO RANDOM NOISE

To test our FWI approach for more realistic situations, we perform an inversion of synthetic data containing random noise. The V_S model is displayed in Figure 5.4, where two vertically separated anomalies with different velocities are present. The V_P and ρ models are set to 1000 m/s and 2000 kg/m^3, respectively. Our goal is to reconstruct these two velocity anomalies from data contaminated by different amounts of random noise. The source-receiver geometry is the same as the one used in the above checkerboard tests. Also, the same boundary conditions are considered on all sides. We use a

band-limited spike (10 ~ 60 Hz) as the source wavelet. Note that the models used for the random-noise experiments are not the same as those used in the above checkerboard tests. There are some artifacts (e.g., the black circle in Figure 5.3d) in the inverted V_S models in the checkerboard tests. If we use the models from the checkerboard tests also for the random-noise experiments, then it is hard to tell in the inverted models whether the artifacts are caused by fitting the random noise or by the FWI algorithm. Figure 5.5a shows an example of a vertical component common-source gather with the source positioned at x = 18 m. A bandpass-filtered (10 ~ 60 Hz) Gaussian noise is then added to the clean gathers to build two datasets with different signal-to-noise ratios (S/N=20, 10). This is done by defining the parameter `sn` in `suaddnoise`, a program from the open-source package `Seismic Unix` [Stockwell and Cohen, 2002]. Figures 5.5b and 5.5c illustrate the resulting noisy gathers.

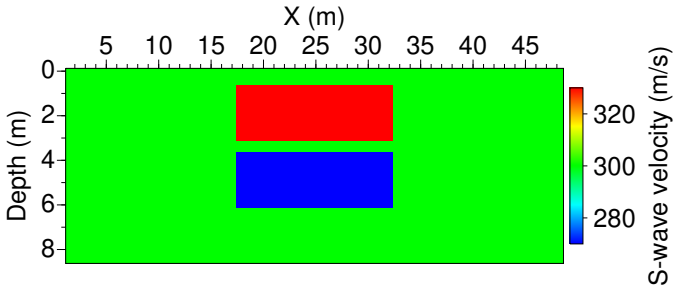

Figure 5.4: A simple V_S model used to test the robustness of the instantaneous-phase coherency FWI to random noise.

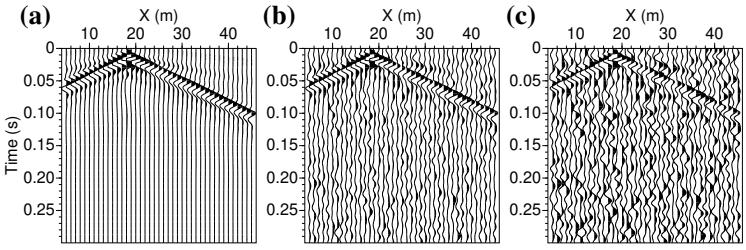

Figure 5.5: (a) Common-source gather (vertical receiver component) computed for the model shown in Figure 5.4, where the source is positioned at x = 18 m; (b) the same as (a) but with random noise of S/N = 20 added; (c) the same as (a) but with random noise of S/N = 10 added.

Before we present the results of the newly proposed FWI, we show the inverted V_S models using the conventional least-squares FWI. Figures 5.6a, 5.6c, and 5.6e present the inverted V_S models obtained from the synthetic data in Figures 5.5a, 5.5b, and 5.5c,

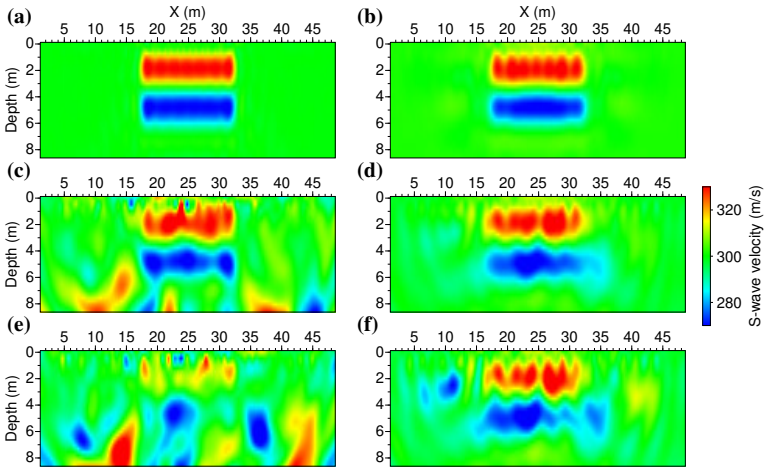

Figure 5.6: Test of inversion robustness to random noise present in the data. To maintain consistency with the checkerboard tests illustrated in Figure 5.3, the same bandpass filter (10 to 60 Hz) is applied to the data in Figure 5.5. (a) Inverted V_S model by least-squares FWI using noise-free synthetic data; (c) the same as (a) but for data contaminated by random noise with S/N = 20; (e) the same as (a) but for data contaminated by random noise with S/N = 10. (b), (d), (f) are the same as (a), (c), (e), respectively, but using instantaneous-phase coherency FWI.

respectively. Comparing the true V_S model (Figure 5.4) with the FWI result shown in Figure 5.6a, the two velocity anomalies are well recovered by the conventional least-squares FWI when there is no noise in the data. However, when there is noise in the data, the result (Figure 5.6c) using conventional least-squares FWI show many undesirable artifacts. These artifacts are caused when the least-squares FWI tries to simulate the additional noise present in the data. When the amount of noise increases (S/N=10), the two vertically separated velocity anomalies become harder to recognize (Figure 5.6e), and the increasing presence of the artifacts becomes problematic.

Figure 5.6b illustrates the inverted V_S models obtained by the instantaneous-phase coherency FWI using the noise-free shot gathers (Figure 5.5a). The velocity structures is imaged well even when S/N = 20 (Figure 5.6d). Comparing Figures 5.6d and 5.6c, the amount of artifacts is greatly reduced. When the S/N of the data decreases even further, for instance when S/N=10, we can still interpret correctly the two anomalies in the inverted result (Figure 5.6f). The proposed instantaneous-phase coherency FWI is robust against the presence of random noise. This is because this new approach peels off the amplitude information from the observed and the synthetic data, and tries to minimize only the instantaneous-phase coherency (instead of the residual) between them. An approach like Tikhonov regularization could potentially help such a situation, but to a limited extent.

5.4. FIELD-DATA APPLICATION

Our study area is located in the ancient Ostia, an archaeological site situated about 25 km west of Rome, Italy. Most of the ruins of Ostia were excavated in the 19th and the first half of the 20th century. These ruins provide a wealth of information about the Roman urban life of antiquity. There are still some unexcavated areas, which are mostly located at the southern boundary of the Region IV of ancient Ostia [Consoli, 2013]. In 2017, we carried out a seismic survey along two lines [Ghose et al., 2020], as shown in Figure 5.7. Under the seismic line A, a mysterious tumulus was identified in the past and is marked by the blue dot in Figure 5.7. This tumulus is now covered by the soil of 0.5 ~ 2 m thickness. The goal of our survey was to characterize this buried tumulus and investigate the possible presence of other buried structures of archaeological significance.

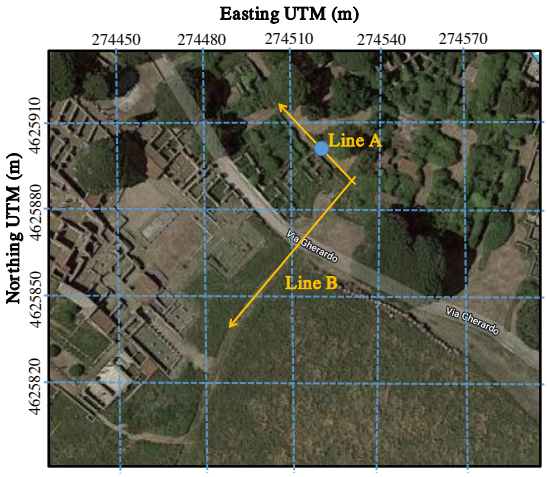

Figure 5.7: Photo of an unexcavated area in the ancient Ostia (from Google map). The two seismic lines A and B are indicated by yellow lines, where the arrows point in the direction of increasing coordinates (directions in which the source was moved) along the x-axes [Ghose et al., 2020]. The blue dot marks the approximate location of a tumulus identified earlier. Note that there are ancient walls present not too far away from the seismic lines.

5.4.1. FIELD-DATA ACQUISITION AND THE MAIN WORKFLOW

Seismic data were acquired along the two lines shown in Figure 5.7. Seismic energy was generated by striking vertically a metal plate with a sledgehammer. At each shot position, four vertical-force shots were excited and the recorded traces were stacked to enhance the S/N. Each shot gather consists of recorded traces from 120 vertical geophones at 0.25 m interval. We used a roll-along approach to acquire the data. The receiver array is illustrated in Figure 5.8. In Figure 5.9, we summarize the main workflow for field-data application of the instantaneous-phase coherency FWI; we will give the details of each step below.

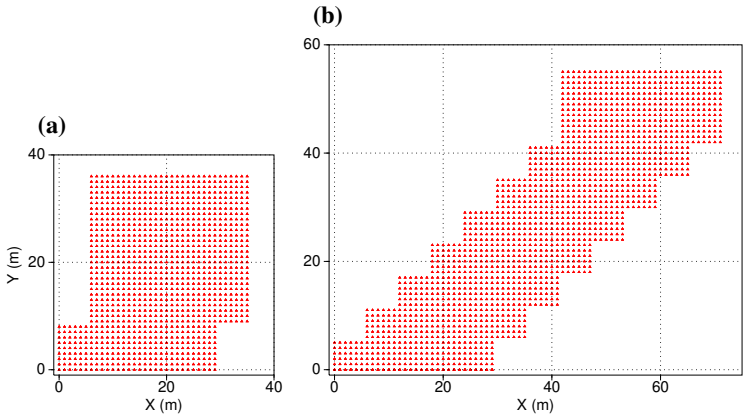

Figure 5.8: Layout of the receiver arrays used to acquire 2D seismic data along (a) seismic line A and (b) seismic line B, marked in Figure 5.7. For seismic lines A and B, the receiver interval is 0.25 m, while the source interval is 1 m. The number of common-source gathers acquired along seismic lines A and B are 37 and 57, respectively. The x-axis denotes the lateral positions of receivers, the y-axis represents the corresponding source positions for each receiver. The small, red triangles represent vertical, single-component geophones. Every fourth receiver position is displayed here.

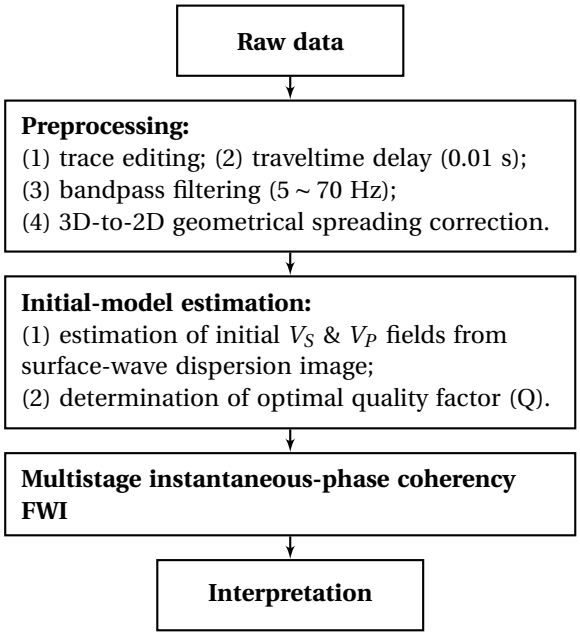

Figure 5.9: Workflow for field-data application of the instantaneous-phase coherency FWI.

5.4.2. PREPROCESSING STEPS

Figures 5.10a and 5.10d display two representative common-source gathers, which are dominated by Rayleigh waves. The corresponding sources are positioned at x = 14.5 m

and x = 29.5 m, respectively. The geometrical spreading of the wavefield takes place in 3D. However, 2D elastic FWI considers 2D wave propagation from a line source and 2D geometrical spreading. Therefore, a procedure that can transform the recorded point-source wavefield to its equivalent line-source wavefield is needed. We adopted the single-velocity transformation approach proposed by Forbriger et al. [2014] and Schäfer et al. [2014]. This 3D-to-2D transformation is derived from a 3D Green's function but with a 2D acoustic wave equation. It has been shown to perform well when applied to shallow-seismic data generated by point sources, e.g., sledgehammers [Dokter et al., 2017; Groos et al., 2017; Pan et al., 2019]. This single-velocity transformation needs the following steps. First, each trace in the common-source gather is multiplied with $\sqrt{t^{-1}}$, where t is traveltime. Such a procedure corresponds to a phase shift by $\frac{\pi}{4}$. Secondly, an offset-dependent factor $F_{amp} = \sqrt{2|r|V_{ph}}$ is multiplied to each trace in order to correct their amplitudes, where V_{ph} denotes phase velocity and r is offset. We use V_{ph} = 200 m/s. A rough estimation of this parameter (phase velocity) is sufficient, as suggested by Groos et al. [2017].

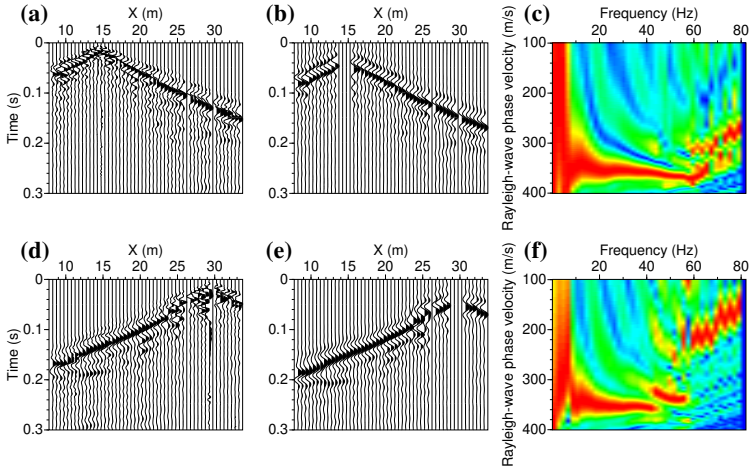

Figure 5.10: (a) A top-muted common-source gather from seismic line A, where the source is positioned at x = 14.5 m; (b) the same as (a) but after preprocessing described in the text; (c) Rayleigh-wave dispersion image obtained by slant-stacking of the preprocessed shot gather shown in (b). (d), (e), (f) are respectively same as (a), (b), (c) but for a common-source gather where the source located at x = 29.5 m.

Apart from the 3D-to-2D transformation, a few other preprocessing steps are also needed. We kill the traces within the absolute source-receiver offset of 1 m because signals in such near-offset are generally clipped [Pan et al., 2019]. Dead traces are removed and all events prior to the first arrivals are muted. To mitigate the occurrence of non-casual parts in the estimated source wavelets during deconvolution, we delay the whole common-source gather by 0.01 s. Finally, we apply a bandpass filter (5 ~ 70 Hz) to the shot gather and normalize each trace by its maximum amplitude value. Figures 5.10b and 5.10e show the same shot gathers as in Figures 5.10a and 5.10d after the preprocessing steps described above. The same preprocessing steps are applied to all

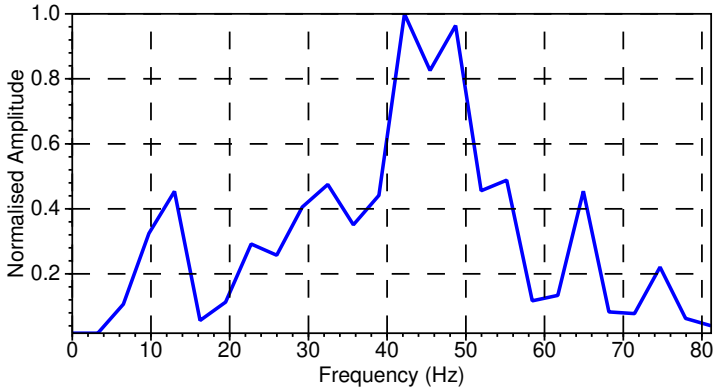

Figure 5.11: Average amplitude spectrum of 37 preprocessed shot gathers acquired along seismic line A.

common-source gathers. Figure 5.11 presents the averaged frequency spectrum of the 37 preprocessed shot gathers acquired along seismic line A.

5.4.3. INITIAL MODELS

The FWI is generally a gradient-based optimization approach, which requires a starting model in the parameter space. For simplicity, we estimate the initial model through multichannel analysis of surface waves (MASW) applied to the preprocessed data [Tran and Sperry, 2018]. Figures 5.10c and 5.10f present the dispersion images calculated using slant-stacking [McMechan and Yedlin, 1981] of the data shown in Figures 5.10b and 5.10e. We can see that the energy concentrates mostly in a narrow band (10 ~ 60 Hz), and the phase velocities of the Rayleigh waves vary in the range of 140 m/s to 160 m/s. Because V_S is slightly larger than the Rayleigh-wave phase velocity, for the starting model of V_S we consider the velocity to be changing linearly from 140 m/s at the surface to 200 m/s at the bottom of the model (z = 12.25 m). The initial V_S models for lines A and B are shown in Figures 5.12a and 5.13a, respectively. The size of the model in Figure 5.12a is 12.25 m in depth and 39.75 m in width (including the C-PML boundaries); the model is made of 50×160 cells with a grid spacing of 0.25 m. The depth of the model is determined approximately by 1/2 ~ 1/3 of the length of the receiver array (29.75/3 ~ 29.75/2 m). The initial V_P model is calculated from the initial V_S model assuming a Poisson's ratio of 0.3. The density is kept constant at 2000 kg/m^3 during the inversion. We do not invert for density because the density of the subsurface has a relatively small impact on the energy of the recorded wavefield at the surface [Groos et al., 2017] and our primary goal is to get a good V_S model. To account for the strong attenuation effects in the near-surface, we use a constant quality factor ($Q_S = Q_P = 15$) to simulate the viscoelastic wave propagation. These optimal Q values are determined by repeating the inversion for a set of

constant quality factors and examining the misfit between the field data and the synthetic data [Dokter et al., 2017].

5.4.4. FWI STRATEGIES

With the initial models for lines A and B described above, we start the instantaneous-phase coherency FWI by first inverting data in the frequency bandwidth 5 ~ 10 Hz. The upper corner frequency of the bandpass filter is then progressively increased to 20, 30, 40, 50, 60 Hz [Bunks et al., 1995]. The FWI result obtained in each frequency band becomes the initial model for inversion in the next frequency band. We move to the next frequency band when the relative misfit value at an iteration becomes less than 1% compared to the misfit value in the previous iteration. During the inversion, we update the V_S and V_P models independently, while the density model is kept fixed. We use a parabolic line search method [Nocedal and Wright, 2006] to determine the optimum step length for updating the V_P and V_S models. As we can see in the recorded shot gathers (e.g., Figures 5.10a and 5.10d), the amplitude of the P-waves is much smaller than that of the Rayleigh waves. The V_P model is thus not as well constrained as the V_S model. Therefore, we only show and interpret the inverted V_S models [Groos et al., 2017]. To update the models in the shallow parts, we apply a preconditioning, semicircular taper to the gradient of each shot. We also smooth the gradients using a 2D Gaussian filter [Ravaut et al., 2004] with a length of approximately half of the dominant wavelength to avoid the occurrence of small-scale artifacts below the FWI resolution limit. For the two seismic lines, the instantaneous-phase coherency FWI converges to provide the V_S models shown in Figures 5.12b and 5.13b.

5.4.5. FWI RESULTS AND THEIR INTERPRETATIONS

In absence of ground truth, we evaluate the final inverted models (Figures 5.12b and 5.13b) from their ability to explain the measured seismic wavefields. We compute synthetic shot gathers using the source wavelets estimated by a stabilised Wiener deconvolution method [Köhn et al., 2016]. The basic idea behind this approach is to deconvolve the recorded data using simulated data obtained from the current subsurface model. In Figures 5.14 and 5.15, we show comparisons between measured shot gathers and synthetic shot gathers for seismic lines A and B, respectively. The main events in the observed common-source gather (e.g., black lines in Figure 5.14a) and the corresponding synthetic gather (e.g., red lines in Figure 5.14a) are very similar. From the overlay of these two gathers (e.g., Figure 5.14a), we can see that the main events match very well without any cycle skipping. There are also some realistic events that are not fully matched. This phenomenon is expected because our misfit function (equation 5.7) is mainly designed to match the instantaneous-phase part of the measured and synthetic data. To recover amplitude information in the synthetic data, we also perform a subsequent envelope-based FWI, starting from the inverted models in Figures 5.12a and 5.13a. However, in the final inverted models, no significant velocity changes are observed, which means that our final inverted models (Figures 5.12b and 5.13b) are good enough to represent the subsurface given the data. Figure 5.16 shows a comparison between the preprocessed field data, synthetic data from the initial models, and synthetic data from the inverted models in the phase velocity-frequency domain. In the Rayleigh-wave dispersion

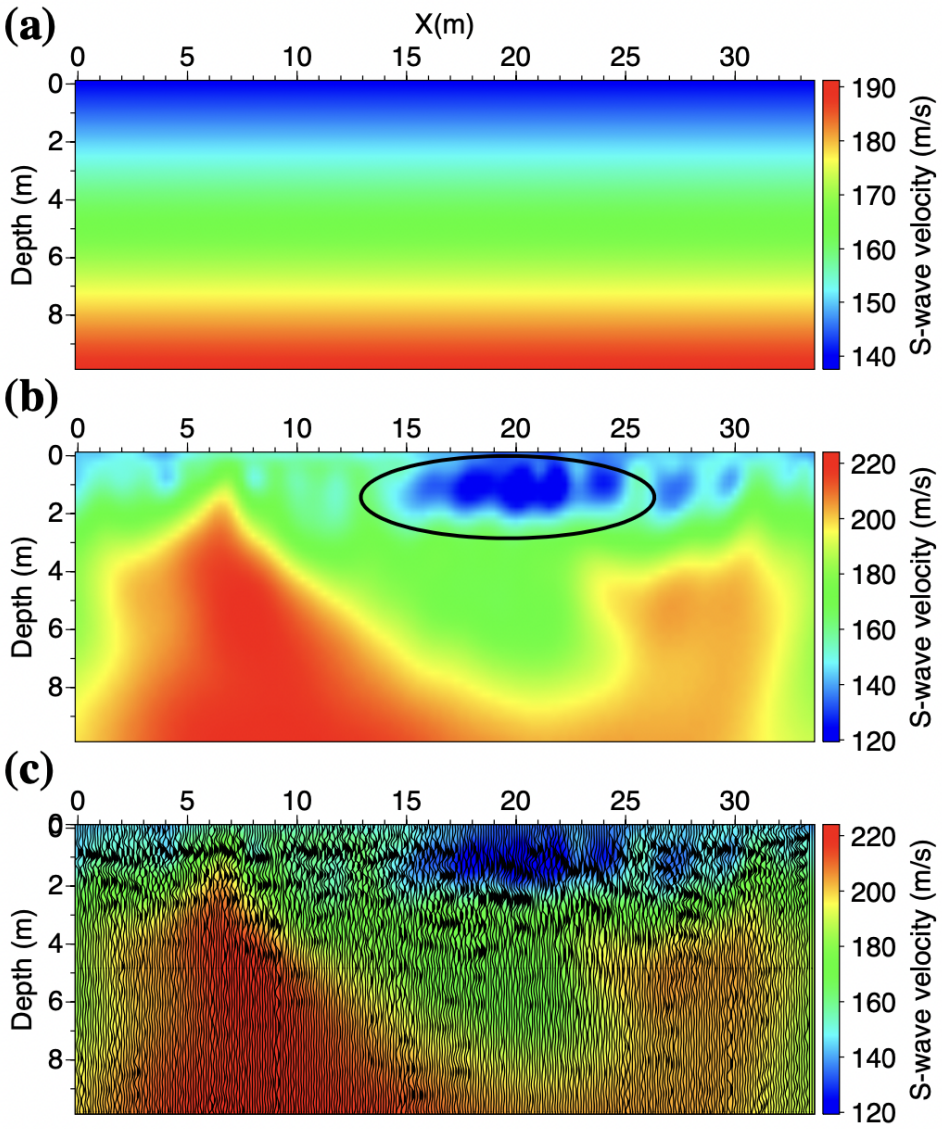

Figure 5.12: Inverted V_S model for seismic line A. (a) Initial model used in inversion; (b) result of instantaneous-phase coherency FWI after the 6th stage of sequential inversion (i.e., frequency band 5 ~ 60 Hz); (c) the overlay of CMP stacked section from S-wave reflection data [Ghose et al., 2020] and the inverted V_S model shown in (b). The ellipse in (b) marks the area where a tumulus was previously identified

.

images of the preprocessed data (e.g., Figure 5.16a), we can observe fundamental and first higher modes. Compared with the dispersion image of the synthetic data obtained from the initial models, the dispersion image from the synthetic data derived from the

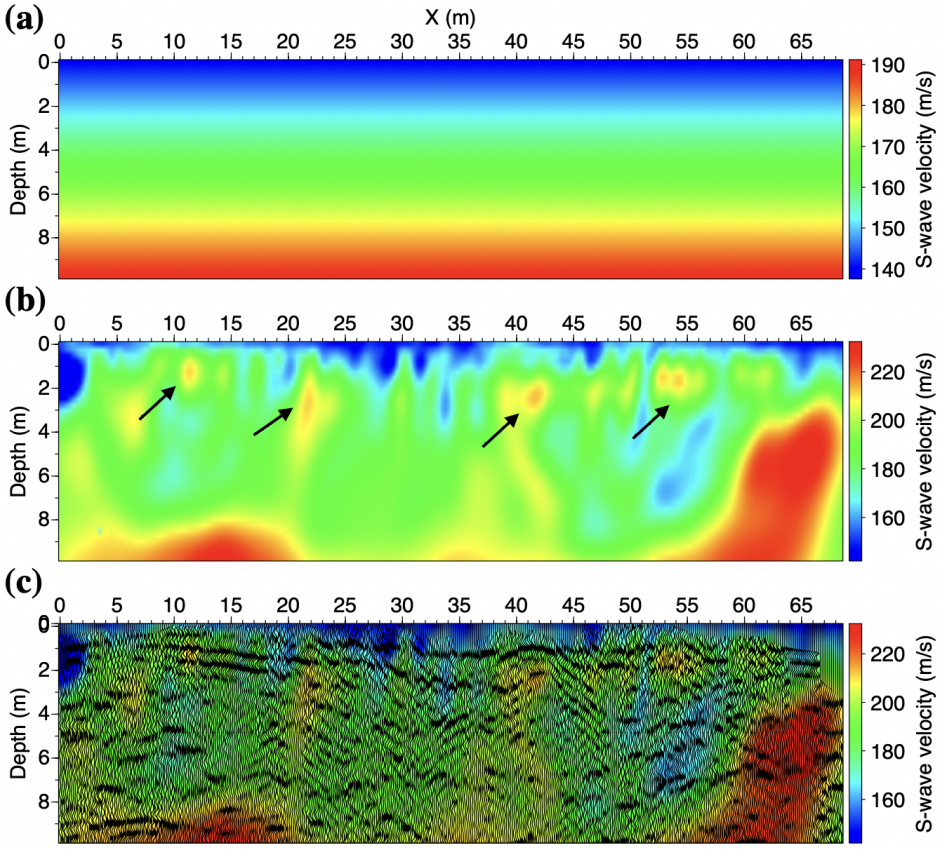

Figure 5.13: Inverted V_S model for seismic line B. (a) Initial model used in inversion; (b) result of instantaneous-phase coherency FWI after the 6th stage of sequential inversion (i.e., frequency band 5 ~ 60 Hz); (c) the overlay of the CMP stacked section from S-wave reflection data [Ghose et al., 2020] and the inverted V_S model presented in (d). The black arrows in (b) indicate potential subsurface heterogeneities of interest.

inverted models can improve the fitting of both the fundamental and first higher modes.

The good fit between the observed and the synthetic data offers confidence to the inverted, final V_S models. For the seismic line A, the 2D V_S profile obtained from instantaneous-phase coherency FWI (Figure 5.12b) shows a low-velocity area at x = 15 ~ 20 m (black ellipse in Figure 5.12b). A known tumulus of archaeological significance, which is covered by soft soil of thickness 0.5 ~ 2 m, was identified in the same vicinity [Ghose et al., 2020]. Based on this information, we interpret the very shallow low-velocity area in our FWI result as the anticipated tumulus body. In the final V_S models for the seismic line B, we notice the presence of many small-size anomalies. Some of these have been marked by black arrows in Figure 5.13b. At present, it is unknown whether these heterogeneities correspond to archaeological objects. Recent shear-wave reflection studies also suggest the possible presence of multiple buried structures in this part of the field [Ghose et al.,

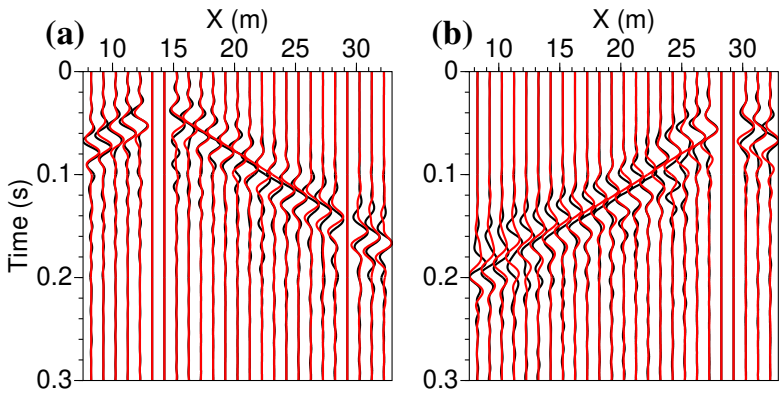

Figure 5.14: Comparison between the measured (black) and the modelled data (red) calculated using the inverted V_S model of Figure 5.12b. (a) The measured and the modelled common-source gathers with their sources located at x = 14.5 m along line A. Data are bandlimited in the frequency range of 5 ~ 60 Hz. Traces are normalized using the maximum value in each trace individually; only every fourth trace is displayed. (b) is same as (a), but for a source at x = 29.5 m.

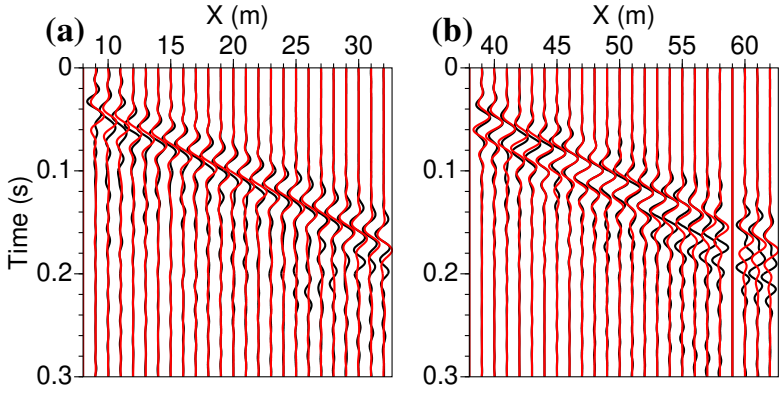

Figure 5.15: Same as in Figure 5.14, but for two common-source gathers acquired along seismic line B with lateral position of the source at x = 10.5, 40.5 m, respectively.

2020].

Ghose et al. [2020] analysed S-wave vibrator data acquired along the same two lines in Ostia. The acquisition geometry is similar to that shown in Figure 5.8. We overlay the stacked seismic reflection sections from Ghose et al. [2020] and the inverted V_S profiles from our FWI (Figures 5.12c and 5.13c). The location of the body-wave scatterers

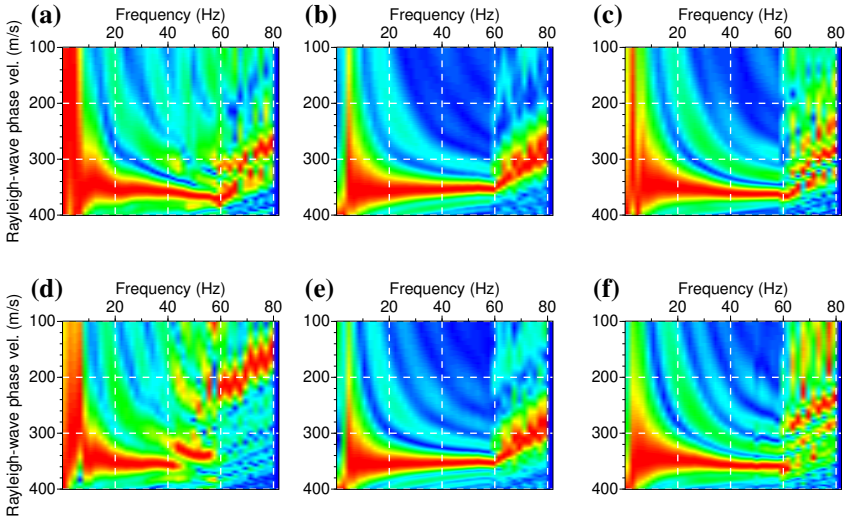

Figure 5.16: Comparison of Rayleigh-wave dispersion images for preprocessed field data, computed data from the initial model, and computed data from the inverted model. (a) Dispersion image calculated from the preprocessed common-source gather shown in Figure 5.14a, the source is located at x = 14.5 m; (b) dispersion image from the computed data using the initial model shown in Figure 5.12a; (c) dispersion image from the computed data using the inverted model shown in Figure 5.12b. (d), (e), (f) are same as (a), (b), (c) but for a common-source gather with the source located at x = 29.5 m.

mapped in the stacked sections matches the locations of some of the plausible underground objects imaged in our FWI results. Distinct, shallow diffraction events were identified in the raw S-wave data. There are also many structures visible in the inverted V_S models that are hard to interpret. Quantifying the uncertainties can help the final interpretation of the FWI results. Uncertainties present in the inverted models can be coming from: (1) the non-linearity of FWI, (2) the uncertainties in building the starting models, (3) the selection of frequency bandwidth for each inversion stage, and (4) undesired amplitude variations at each source/receiver position. Resolution analysis [Cai and Zelt, 2019; Fichtner and Trampert, 2011] is a promising tool for the quantification of such uncertainties; this needs further investigation.

The field data acquired in 2D seismic surveys are often contaminated by scattered waves from the out-of-plane objects and other incoherent noise. There are ancient walls (Figure 5.7) near our survey lines. The seismic lines were planned in such a way that the distance from these walls to the seismic line is more than 10 ~ 12 m. Therefore, the very shallow scattered energy in our data is most probably not due to side-scatterring. Nevertheless, it is possible that the side-scattering from those ancients walls is present at slightly later times in the acquired seismic wavefield. For a reliable interpretation, one should try to eliminate such events before performing FWI. Seismic interferometry can be advantageously used to retrieve and enhance the surface waves arriving from the inline direction [Balestrini et al., 2019; Liu et al., 2018, 2021] and suppress the interference of out-of-plane seismic energy. Inversion of such retrieved data can prevent imaging ar-

tifacts. 3D seismic imaging can also add more constraints to such interpretation. This will be the direction of our future research.

5.5. CONCLUSIONS

We introduced a new instantaneous-phase coherency measure, and extend it as a misfit function that can be directly incorporated into full-waveform inversion (FWI). Such instantaneous-phase coherency has earlier been a key to the phase-weighted stacking (PWS) for enhancing signals with similar instantaneous phase. We presented the details of how to compute the gradients of a new misfit function using the adjoint-state method. We validated the robustness of our FWI approach using checkerboard tests and data contaminated by random noise. Finally, we applied our new approach to field data acquired at an archaeological site located in Ostia, Italy. The locality containing a tumulus, known to be buried under a shallow soil cover, could be identified in our FWI results. The inversion results of instantaneous-phase coherency FWI also showed that the subsurface of this unexcavated part of the archaeological site of Ostia has a high degree of heterogeneity, with the likely presence of small objects in the shallow subsurface. But this interpretation needs more careful analysis. Our results suggest that FWI based on the instantaneous-phase coherency method can be a promising noninvasive tool for archaeological site investigation.

6

REDUCING NEAR-SURFACE ARTIFACTS BY FULL-WAVEFORM INVERSION OF INTERFEROMETRIC SURFACE WAVES

Seismic incoherent noise and waves scattered from objects in the crossline directions can cause the 2D elastic full-waveform inversion (FWI) to produce artifacts in the resulting 2D models. We develop a complete workflow that can determine subsurface S-wave velocity (V_S) models inverted from 2D near-surface seismic data more stably. We make use of a combination of super-virtual interferometry (SVI) and matching filter to accurately retrieve dominant surface waves from the field data, while the incoherent noise and 3D scattering events are significantly suppressed. The subsurface structures obtained from inverting the retrieved data can be interpreted together with the sections resulting from FWI of the original data, to mitigate the potential misinterpretation of artifacts. Our results demonstrate that it is possible to invert 2D near-surface seismic data even when the data quality is lowered by the presence of strong noise and 3D scattered events from objects located in the crossline direction.

The main contents of this chapter has been submitted to *Geophysics*. For consistency, minor changes have been made.

6.1. INTRODUCTION

Obtaining details of small-scale near-surface subsurface structures in a non-invasive way is an important issue in various fields of applications, such as geotechnical site investigation [Nguyen and Tran, 2018], groundwater management [Lambot et al., 2008], natural-hazard evaluation [Mecking et al., 2021], and archaeological prospecting [Dokter et al., 2017; Köhn et al., 2019]. An appropriate method to resolve near-surface features is an elastic full-waveform inversion (FWI). Over the past decades, much of the research on elastic FWI [Mora, 1987; Vigh et al., 2014] has focused on exploiting body waves at the exploration scale. However, surface waves dominate the near-surface wavefield, and their amplitudes are very sensitive to the distribution of the S-wave velocity (V_S). Therefore, it seems more appropriate to use surface waves to characterize the near-surface structures.

In the context of near-surface characterization, there are several approaches to obtaining a 2D V_S model by inverting surface-wave full-waveform data. Tran et al. [2013] developed a 2D time-domain Gauss-Newton Rayleigh-wave FWI to detect possible sinkholes and other anomalies. Groos et al. [2017] proposed a complete 2D Rayleigh-wave FWI workflow to reconstruct shallow small-scale lateral changes in the V_S structure. Dokter et al. [2017] and Köhn et al. [2019] applied SH-FWI (where SH stands for S-wave polarized in the horizontal direction when propagating horizontally) for mapping near-surface small-scale structures at archaeological sites.

Most of the above-mentioned field applications of FWI have so far been demonstrated on near-surface seismic data along 2D lines. Next to the desired events, the recorded data might additionally contain relatively stronger seismic noise and suffer from interference due to 3D scattering from crossline objects. In the 2D elastic FWI, the algorithm will try to mimic these additional events associated with wave propagation, which may cause strong artificial heterogeneity in the resulting 2D models. To mitigate these pitfalls, these additional events should be suppressed before the application of FWI, while the surface-wave response from the structures below the investigated 2D seismic survey line should be preserved.

In this study, we propose to retrieve the dominant surface-wave responses along the inline direction in a data-driven manner using super-virtual interferometry (SVI) [Bharadwaj et al., 2011; Dai et al., 2011; Liu et al., 2021; Place et al., 2019]. We correct the amplitude and phase errors from the retrieval procedure by means of SVI using matching filters [Fomel, 2007]. We then invert the resulting surface-wave waveforms in the time domain to estimate the near-surface V_S structure. After a short description of each step in detail, we will apply our proposed FWI workflow to seismic data acquired over an archaeological site.

6.2. METHODOLOGY

During the acquisition of a 2D near-surface seismic dataset, events reflected (or scattered) from crossline objects are also recorded in the shot gathers. In 2D FWI, the algorithm tries to mimic these events, and hence artificial subsurface objects are produced. To reduce such incoherent noise or 3D events, we make use of SVI to retrieve and enhance the inline surface waves. We then apply a matching filter to correct for the ampli-

tude and phase errors that occur unavoidably during the procedure of SVI. The resulting data can then be input to the 2D FWI algorithm for subsurface imaging. The complete workflow consisting of all these steps is summarised in Figure 6.1. Our workflow is designed for surface waves (e.g., Rayleigh waves and Love waves). In this chapter, we focus on inverting SH-waves field data. For Rayleigh waves, the propagation depends on the subsurface distribution of mainly the V_S, density (ρ), but also on the P-wave velocity (V_P). Contrary to that, the propagation of Love-waves requires only the knowledge of V_S and ρ. Compared to PSV-FWI (where P stands for P-waves and SV for S-waves polarized in the vertical direction when propagating horizontally), SH-FWI requires significantly less computational resources due to the reduced size of the parameter space. In the following, we will present the theory behind each step in detail.

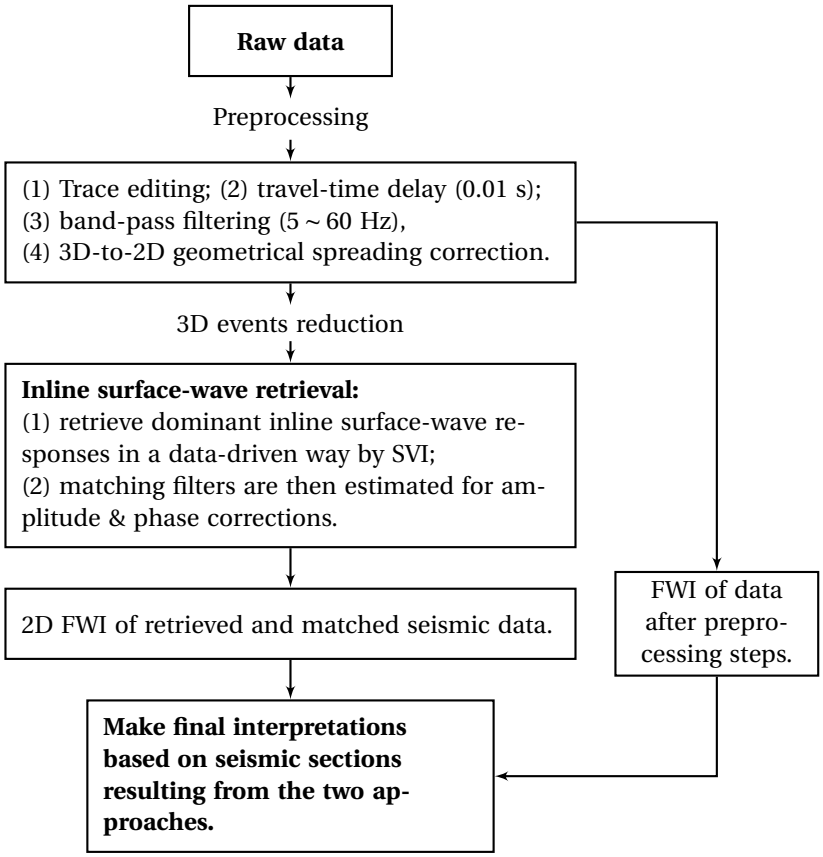

Figure 6.1: The main workflow proposed in this chapter. Note that the preprocessing steps will differ per dataset.

6.2.1. INLINE SURFACE-WAVE RETRIEVAL BY SVI

SVI was first proposed to enhance the refraction signals at far offsets [Bharadwaj et al., 2011; Place et al., 2019], and later it was modified to enhance weak diffraction signals [Dai et al., 2011; Liu et al., 2021]. The procedure for retrieving and enhancing the ***shot-to-receiver*** surface waves is similar, and it is illustrated in Figure 6.2.

In Figure 6.2a, $\rightsquigarrow$ indicates surface waves propagating from an active source **X** to receivers along the Earth's surface. The surface waves recorded at receiver **A** and **B** can be denoted as $u(X_A, X_i)$ and $u(X_B, X_i)$, respectively. By crosscorrelating these two recordings, we can obtain the virtual surface wave (red $\rightsquigarrow$) at **B** as if it were coming from a virtual source at **A**. The traveltime of these virtual waves is the same as at other actual source positions as long as they fall inside the stationary-phase region [Snieder, 2004], so they can be stacked constructively to retrieve the surface waves propagating from **A** to **B**. In the frequency domain, this step can be formulated as [Halliday et al., 2007; Wapenaar and Fokkema, 2006]

$$C_{X_B X_A} = \sum_{i=1}^{N} u^*(X_A, X_i) \cdot u(X_B, X_i), \tag{6.1}$$

where $C_{X_B X_A}$ denotes the retrieved ***receiver-to-receiver*** surface waves propagating from **A** to **B**. The superscript $*$ denotes complex conjugation in the frequency domain, which corresponds to the time-reversal operation in the time domain. N represents the number of sources available for stacking.

To further obtain ***shot-to-receiver*** surface waves propagating from **X** to **B**, additional convolution and stacking steps follow. This is demonstrated in Figure 6.2b, where the retrieved virtual surface wave (red $\rightsquigarrow$) is convolved with an recorded surface-wave arrival at a receiver position **A** from the source at **X** to produce a super-virtual wave at **B**. For all receiver positions **A** located between the source **X** and the receiver at **B**, the super-virtual wave is kinematically equivalent. Thus, the retrieved surface waves can be further enhanced by stacking super-virtual surface waves over different receiver positions **A**, which can be expressed in the frequency domain as

$$C_{X_B X_i} = \sum_{X_A} C_{X_B X_A} \cdot u(X_A, X_i), \tag{6.2}$$

where $C_{X_B X_i}$ denotes the retrieved ***shot-to-receiver*** surface waves. Contrary to traditional seismic interferometry (SI) for surface-wave retrieval and suppression [Balestrini et al., 2019; Konstantaki et al., 2015a; Liu et al., 2018], this SVI approach relaxes the requirement that an active shot and a receiver should coexist at the same position for adaptive subtraction.

6.2.2. MATCHING-FILTER ESTIMATION

To accurately retrieve the amplitude of the seismic response using equations 6.1 and 6.2, there are several requirements to be fulfilled according to the theory of SI [Draganov et al., 2006; Wapenaar and Fokkema, 2006]: the sources should illuminate the receivers homogeneously, the enclosing source boundary should be a sphere with a large radius, the medium at and outside the source boundary should be homogeneous, and the medium

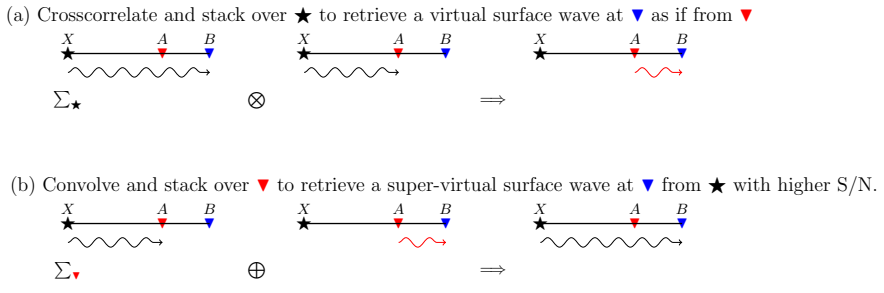

Figure 6.2: The step for retrieving dominant ***shot-to-receiver*** surface waves between source **X** and receiver **B** by super virtual interferometry (SVI). $\otimes$, $\oplus$ denote crosscorrelation- and crossconvolution-based operators, respectively. $\rightsquigarrow$ represents surface waves propagating along the Earth's surface. The symbols ★ and ▼ represent active source and receiver, respectively.

parameters should change smoothly across the source boundary. In addition, the application of equation 6.1 also assumes a lossless medium. Note also, that for retrieval of higher-mode surface waves, sources are required also in the shallow (in the wavelength sense) subsurface [Kimman and Trampert, 2010; van Dalen et al., 2013]. These requirements are very hard to meet in conventional 2D near-surface seismic surveys, where the active sources and receivers are normally deployed only at the surface. Thus, the retrieved surface waves will be characterized by amplitude errors and possibly even phase errors.

To make the retrieved surface waves suitable for FWI, these errors should be corrected. We estimate a non-stationary matching filter [Fomel, 2007, 2009] to account for these errors, by solving the following least-squares inversion problem:

$$\min \left| \sum_{\gamma} C_{X_B X_i}(\gamma t) * \mathbf{f}(\gamma, t) - D_{X_B X_i}(t) \right|^2, \tag{6.3}$$

where $C_{X_B X_i}$ and $D_{X_B X_i}$ are respectively retrieved and recorded surface waves at receiver X_B from the source position X_i. $*$ is the convolution operator, $\mathbf{f}(\gamma, t)$ is the estimated non-stationary matching filter, γ is a stretching variable. Equation 6.3 presents an ill-posed problem because it contains more unknown variables than constraints. One remedy is to add additional constraints, i.e., regularization, to limit the variability of the filter coefficients $\mathbf{f}(\gamma, t)$. With shaping regularization [Fomel, 2007], equation 6.3 can be solved as

$$\mathbf{f}(\gamma, t) = \frac{\mathbf{S}\mathbf{P}^T\mathbf{D}}{\left[\lambda^2\mathbf{I} + \mathbf{S}\left(\mathbf{P}^T\mathbf{P} - \lambda^2\mathbf{I}\right)\right]^{-1}}, \tag{6.4}$$

where λ is a scaling coefficient, which is defined as $\lambda = |C_{X_B X_i}(t)|^2$. The terms $\mathbf{P}$ and $\mathbf{D}$ are the diagonal matrices composed of $C_{X_B X_i}(\gamma t)$ and $D_{X_B X_i}$, respectively. $\mathbf{I}$ is the identity operator in the data space. $\mathbf{S}$ represents the shaping operator which, for this application, we have chosen to be a triangular smoothing operator. In the procedure of shaping regularization, the only additional parameter to control is the radius of the

smoothing operator. As the smoothing radius increases, the result of the non-stationary matching filter regularized by the shaping operator approaches the result of the stationary matching filter. In practice, we define the triangular smoothing operator with a small radius ($r_1 = 10, r_2 = 5$), which can significantly suppress the incoherent noise and 3D scattering events, while preserving the inline surface waves. After estimating the filter coefficients through equation 6.4, we convolve them with the retrieved surface waves ($\sum_\gamma C_{X_B X_i}(\gamma t) * \mathbf{f}(\gamma, t)$) to account for the errors. The resulting data will be dominated by inline surface waves, while incoherent noise and other 3D events from the crossline direction will be suppressed. These data are thus suitable for 2D elastic FWI to characterize 2D subsurface structures.

6.2.3. THEORY OF 2D SH-FWI

The FWI [Tarantola, 1984] is a method to deduce high-resolution models of the subsurface (such as V_S and density) by minimizing the residuals between synthetic and measured data. The method consists of two main steps. One is to simulate synthetic wavefields by solving the governing wave equation. The second step is to update the model parameters via a nonlinear-inversion approach (such as the conjugate gradient method) until the misfits between modelled and measured data are negligible.

We make use the acquired SH-wave data. Thus, the propagation of waves in a 2D visco-elastic isotropic medium can be described by the following equation [Aki and Richards, 2002; Köhn et al., 2016]:

$$\hat{L}_{kl}(\mathbf{x})\mathbf{u}_l(\mathbf{x}, t) = f_k(\mathbf{x}, t), \tag{6.5}$$

where $\mathbf{u}_l$ denotes the l-th component of the particle-displacement vector, f_k the directional component of the body force. $\hat{L}_{kl}(\mathbf{x})$ is the differential operator:

$$\hat{L}_{kl}(\mathbf{x}) = \rho(\mathbf{x})\delta_{kl}\frac{\partial^2}{\partial t^2} - \frac{\partial}{\partial x_j}\Psi_{jkml}(\mathbf{x}) * \frac{\partial}{\partial x_m}, \tag{6.6}$$

where Ψ is a tensor of rank four that contains the time derivatives of the relaxation functions, which describe the rheology of the medium, δ_{kl} is the Kronecker delta ($\delta_{kl} = 0$ for $k \neq l$; $\delta_{kl} = 1$ for $k = l$), and $*$ denotes the convolutional operator. Equation 6.5 can be solved by a time-domain 2D finite-difference (FD) algorithm [Virieux, 1984]. We use convolutional perfectly matched layers (C-PML) absorbing boundary conditions [Komatitsch and Martin, 2007] to damp spurious reflections from the model's left, right and bottom boundaries. At the model's top boundary, the free-surface condition is implemented by the image technique [Robertsson, 1996] for accurate modeling.

To update the model parameters along the direction where the residuals between the modelled and the measured data are decreasing, a specific misfit function measuring the difference between computed and measured data should first be defined. Traditionally, a misfit function is defined in a least-squares sense [Tarantola, 1984] to serve the criterion for measuring the similarity between modelled and measured data. However, this kind of misfit function is not very suitable for near-surface seismic field data. This is mainly because the receiver coupling at each source/receiver position is different, resulting in offset-dependent amplitude variations [Dokter et al., 2017]. To partly mitigate

this problem, we choose to use our recently proposed misfit function [Liu et al., 2022] to measure the instantaneous-phase coherency between measured and synthetic data modelled. This type of misfit function assigns stronger weights to the phase part of the signals, and it is explicitly independent of amplitude errors. It is formulated as

$$
\begin{aligned}
J(t) &= \frac{1}{4}\sum_{s,r}\int_0^T \left\{ \left| e^{i\phi_1(t)} - e^{i\phi_2(t)} \right|^2 - \left| e^{i\phi_1(t)} + e^{i\phi_2(t)} \right|^2 \right\} dt \\
&= \frac{1}{4}\sum_{s,r}\int_0^T \left| \frac{d_1(t) + i\mathscr{H}\{d_1(t)\}}{\sqrt{d^2(t) + \mathscr{H}^2\{d_1(t)\}}} - \frac{d_2(t) + i\mathscr{H}\{d_2(t)\}}{\sqrt{s^2(t) + \mathscr{H}^2\{d_2(t)\}}} \right|^2 dt \\
&- \frac{1}{4}\sum_{s,r}\int_0^T \left| \frac{d_1(t) + i\mathscr{H}\{d_1(t)\}}{\sqrt{d^2(t) + \mathscr{H}^2\{d_1(t)\}}} + \frac{d_2(t) + i\mathscr{H}\{d_2(t)\}}{\sqrt{s^2(t) + \mathscr{H}^2\{d_2(t)\}}} \right|^2 dt,
\end{aligned}
\tag{6.7}
$$

where $J(t)$ is the value of the misfit function. $e^{i\phi_1(t)}$ and $e^{i\phi_2(t)}$ are the exponential phases of the measured ($d_1(t)$) and the synthetic data ($d_2(t)$), respectively. $\mathscr{H}\{\cdot\}$ denotes the Hilbert transform. $\sum_{s,r}$ represents summation over all available sources and receivers, T the recording time of the acquired data. Using the theory of complex analysis, equation 6.7 can also be written as

$$
J(t) = \frac{1}{2}\left\{ \sin^2\left(\frac{\phi_1(t) - \phi_2(t)}{2}\right) - \cos^2\left(\frac{\phi_1(t) - \phi_2(t)}{2}\right) \right\}, \tag{6.8}
$$

where $\phi_1(t)$ and $\phi_2(t)$ are the instantaneous phases of the measured and synthetic data, respectively. Note from equation 6.8 that the instantaneous-phase coherency equals one when the two signals have opposite polarity ($\phi_1(t) = -\phi_2(t)$) and equals minus one when the two signals have the same polarity ($\phi_1(t) = \phi_2(t)$). The value of $J(\mathbf{m})$ can be minimized by iteratively updating the model parameters ($\mathbf{m}$), beginning at the initial model ($\mathbf{m}_0$), along a search direction determined by a nonlinear optimization approach, such as the preconditioned conjugate gradient method [Nocedal and Wright, 2006].

6.2.4. MASW FOR INITIAL MODELS BUILDING

To avoid being trapped in a local minimum, 2D elastic FWI needs a good initial model to start. In this chapter, we use multichannel analysis of surface wave (MASW) to provide the initial V_S model. MASW has been proven to be an efficient means to obtain velocity profiles by inverting the dispersion curves of surface waves (e.g., Xia et al. [1999]). Compared with FWI, which utilizes all the information (amplitude and phase) from a recorded wavefield, MASW uses only the dispersion curve skeletonized from a complex wavefield. Thus, the MASW approach converges more easily; on the other hand, the resolution of the extracted structure from MASW will be much lower than that from FWI. Hence, it is beneficial to build initial models by MASW for subsequently using them as input for FWI.

MASW includes two steps – the first is to extract the dispersion curve from a recorded shot gather and the second is to fit the picked and the modelled dispersion curve to obtain the velocity models. In this research, we transfer the recorded wavefield data from the time-space ($t-x$) domain to the frequency-slowness ($f-p$) domain using the

slant-stack approach [McMechan and Yedlin, 1981]. The dispersion curves of different modes can then be easily picked. We use the Neighborhood Algorithm (NA) [Sambridge, 1999; Wathelet, 2008] to minimize the misfit between picked and computed dispersion curves, resulting in a 1D velocity structure for a specific lateral position.

6.3. FIELD-DATA EXAMPLE

The study area is located at Dreumel, central Netherlands. The purpose of this survey was to locate/characterize with a high resolution the presence of ancient boats that were anticipated to be buried under shallow soil covers at this site. We carried out a seismic survey along two lines. We present here the FWI results along one of the survey lines.

6.3.1. FIELD-DATA ACQUISITION

We used a high-frequency S-wave vibrator [Ghose, 2012; Ghose et al., 1996] to excite seismic energy. The receiver array consisted of 120 10-Hz horizontal geophones at an interval of 0.25 m. We oriented the vibrator (source orientation) and the geophones in the crossline direction so that we could generate and record SH-waves. We used a roll-along geometry during data acquisition, the layout of the receivers is illustrated in Figure 6.3. At each shot position, four recordings were acquired and stacked to yield one common-source gather, to enhance the signal-to-noise ratio (S/N) of the acquired data in the field. In total, 105 common-source gathers were recorded and used subsequently for imaging the subsurface.

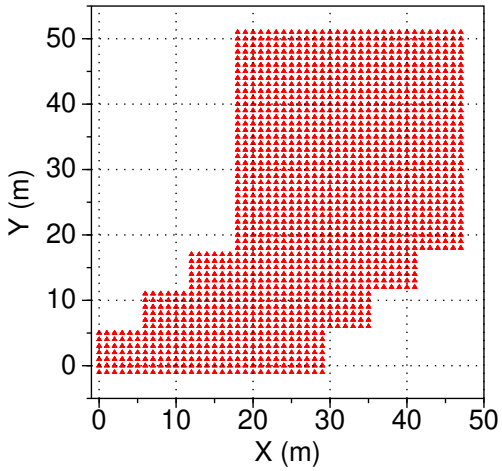

Figure 6.3: Layout of receiver array used to acquire 2D seismic data in a roll-along receiver geometry. The x-axis denotes the lateral positions of receivers, the y-axis represents the corresponding source positions for each receiver. The triangles represent horizontal, 10 Hz, single-component geophones. Every receiver position with an interval of 1 m is displayed.

6.3.2. INLINE SURFACE-WAVE RETRIEVAL

Figures 6.4a and 6.4e display two examples of S-wave common-source gathers after application of crosscorrelation of the raw vibrograms with the estimated groundforce [Ghose, 2002] and followed by two other basic preprocessing steps — trace editing and bandpass filtering between 5 Hz and 60 Hz. We can see that the data is dominated by dispersive Love waves. Underneath those Love waves, we can also identify weak reflection and diffraction events. Although the amplitude of these events (reflections/diffractions) is much lower than those of the Love waves, these events in the recorded data can cause additional problems during the FWI procedure. Especially when inverting the low frequencies, the FWI can interpret those reflections/diffractions as part of the Love-wave dispersion, which may lead to artifacts in the 2D inverted models. Therefore, the Love waves should be separated from the other events for further inversion.

Figures 6.4b and 6.4f display the virtual gathers retrieved by SVI (equations 6.1 and 6.2 and Figure 6.2) for a virtual source at the position of the active source in Figures 6.4a and 6.4e. Comparing Figures 6.4b and 6.4a (and also Figures 6.4f and 6.4e), we can see that the main kinematic characteristics of the Love waves are retrieved well. However, due to the interferometric approximations used in equations 6.1 and 6.2, there are errors in the estimated Love waves in Figures 6.4b and 6.4f. We correct these errors by estimating a non-stationary matching filter (equation 6.4) and then convolving this filter with the virtual gather (Figures 6.4b and 6.4f), resulting in the matched Love waves (Figures 6.4c and 6.4g). The phase and amplitudes of the retrieved Love wave in Figures 6.4c and 6.4g match well with those in the original active-source shot gather while the weak reflections and diffractions are greatly suppressed (Figures 6.4d and 6.4h). In the following, we will mainly make use of shot gathers as the one shown in Figure 6.4c, for the FWI procedure.

6.3.3. FWI RESULTS

The recorded wavefields were excited by a spatially limited (point) source, while the 2D elastic FWI considers 2D wave propagation modelled with a line source. To compensate for that, we turn the recorded seismic wavefield to its equivalent line-source wavefield by the single-velocity transformation approach [Forbriger et al., 2014; Schäfer et al., 2014]. To stabilize the procedure of source-wavelet estimation using a Wiener-deconvolution approach [Groos et al., 2017], we delay the whole common-source gather by 0.01 s. We also kill the traces falling inside the near-offset range (less than 1 m), because such near-offset traces are partly clipped and thus contain less information about the subsurface [Pan et al., 2019]. Noise before the first arrivals is muted. Additionally, we normalize each trace by its maximum. The above preprocessing steps are applied to common-source gathers (as in Figures 6.4a and 6.4c), which are subsequently used in FWI.

To avoid being trapped in local minima, proper initial models are required. We estimate the initial model through the MASW approach described above. Figure 6.5a shows a shot gather of the retrieved Love waves after SVI and matching filtering for a source located at 18.5 m. The corresponding dispersion image of the retrieved wavefield is shown in Figure 6.5b. We pick the dispersion curve (white-dashed line in Figure 6.5b) along with the maximum energy in the dispersion image. We generate 30000 models using the NA approach and select the best model whose theoretical dispersion curve fits best the

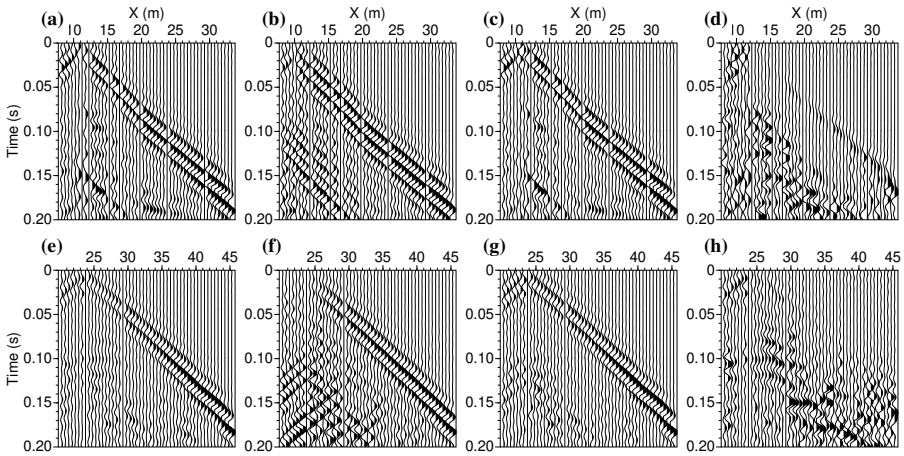

Figure 6.4: (a) A typical preprocessed SH-wave shot gather. The preprocessing steps include trace editing and band-pass filtering (5 ~ 60 Hz); (b) retrieved supervirtual Love waves for a virtual source at a position as in (a); (c) result after convolution of the data in (b) with a non-stationary matching filter to account for the errors in the retrieval during the procedure of SVI; (d) result after subtraction of (c) from (a). (e-h) as in (a-d), but for a common-source gather with a different source position. Every second trace is plotted.

picked one. The computed dispersion curve (black curve in Figure 6.5b) from the best V_S model (black line in Figure 6.5c) is plotted together with the picked dispersion data. Because the dispersion images calculated at other lateral positions are similar, we use only the inverted V_S structure at this position to build the laterally homogeneous V_S model, by extending the 1D model in the horizontal direction. The initial V_S model is displayed in Figure 6.5d. We discretize the model with 215×40 grid points in the x and z directions, with a grid spacing of 0.25 m. To ensure the stability of wave simulation, we choose a timestep of 50 ms, with a recording time of 0.2 s. The density model is assumed to be known and kept constant at 1800 kg/m^3. We choose a constant quality factor ($Q_S = 20$) [Bohlen, 2002; Cheng et al., 2018] to account for the strong attenuation effects at the near-surface. We determined this optimal Q value by repeating the inversion for a set of constant quality factors and using the relative objective function (Figure 6.6) to select the optimum Q value.

Starting from this initial model, we apply elastic FWI by first inverting a subset of the data within the frequency band 5 ~ 10 Hz. The upper corner frequency of the passband is then subsequently increased to 20, 30, 40, and 50 Hz. The FWI result from each frequency band is used as the initial model for the next frequency band. We move to the next frequency band once the improvement in the misfit value for the current frequency band becomes smaller than 1% between two consecutive iterations. This also serves as the abort criterion for the last stage where a subset of the data within the frequency band 5 ~ 50 Hz is inverted. To obtain an update at the shallower part, we precondition the gradients using a semicircular taper [Groos et al., 2017] with a length of 3 m. We also smooth the gradients and models by a 2D Gaussian filter [Ravaut et al., 2004] with a length of ap-

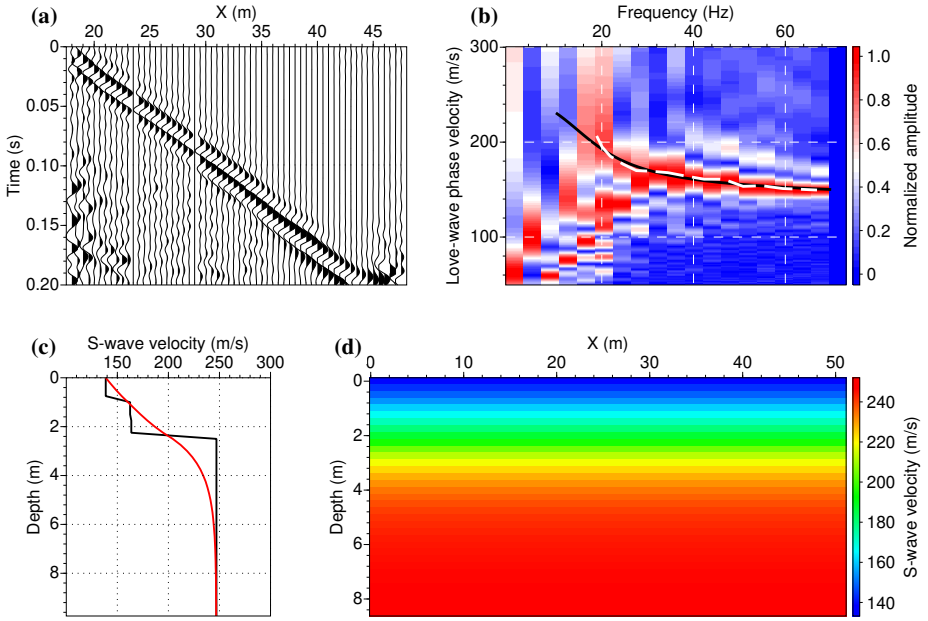

Figure 6.5: (a) An example of shot gather showing retrieved Love waves after SVI and matching filtering, as in Figure 6.4(c), for a source at 18.5 m. Every second trace is plotted. (b) Dispersion image of the data in (a) calculated by a slant-stack procedure. The white-dashed line denotes the picked Love-wave dispersion curve of the fundamental mode. The black line is the theoretical dispersion curve calculated from the finally inverted V_S profile as shown in (c). (c) Estimated 1D V_S structure (black line) obtained by minimizing the misfit between picked and computed dispersion curves. Such minimization is performed with the neighborhood algorithm (NA) using the code from Wathelet et al. [2020]. The red line represents the smoothed version of the estimated structure (black line), which is then extended laterally to build the initial, laterally homogeneous V_S model (d) for the subsequent elastic FWI.

proximately half of the dominant wavelength. This is done to avoid the occurrence of small-scale artifacts below the FWI resolution limit and make the inversion stable. The evolution of the normalized least-squares misfit functions during FWI of the field data is displayed in Figure 6.7, where the normalized misfit reduces from 1.0 at the first iteration to around 0.2 at the final iteration.

The FWI of the dominant Love waves retrieved by SVI and matching filtering converges after a total of 63 iterations. Figure 6.8a shows the final inverted V_S results for the frequency bands 5 ~ 50 Hz. To show how FWI has improved the subsurface V_S structures, we have plotted slices of the 1D inverted V_S profile from FWI (Figure 6.8a) and the 1D initial V_S profile from MASW (Figure 6.5d) at x = 10 m, 20 m, 30 m, 40 m, respectively. Based on the final inverted V_S model, we model the synthetic data using source wavelets as shown in Figure 6.9. These source wavelets are estimated by a stabilized Wiener-deconvolution approach [Groos et al., 2017]. In Figures 6.10a and 6.10c, we show the overlay for two source positions of the shot gathers with the Love waves retrieved by

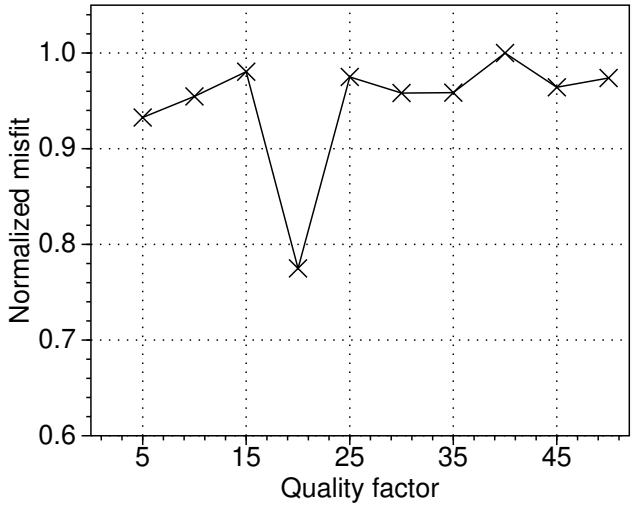

Figure 6.6: Determination of the optimum quality factor by repeating the inversion for a set of constant Q values. The least-squares misfits between the synthetic and measured data for each inversion are displayed.

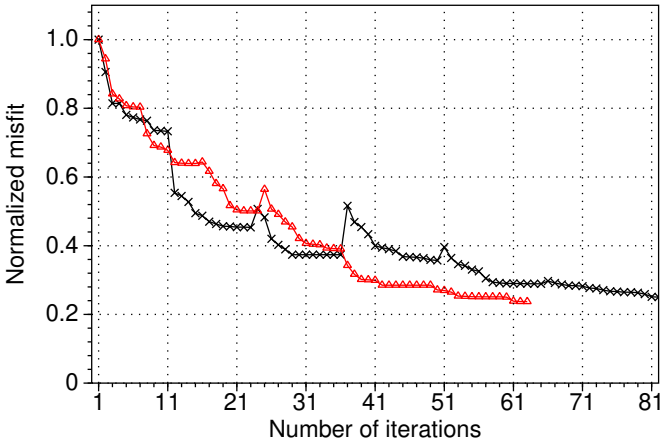

Figure 6.7: Evolution of the normalized misfit values during FWI of data as in Figure 6.4a (black line) and FWI of data as in Figure 6.4c (red line). Note that FWI of data after the procedure of super-virtual interferometry (SVI) and matching filter converges faster.

SVI and matching filtering, and the shot gathers with the synthetic Love waves, and also their residuals. From the overlay of these two gathers, we can see that the main events across the entire offset range are matching quite well without any obvious cycle skipping. The residuals (Figures 6.10b and 6.10d) are small across the entire source-receiver offset range, except for channels far away from the source locations.

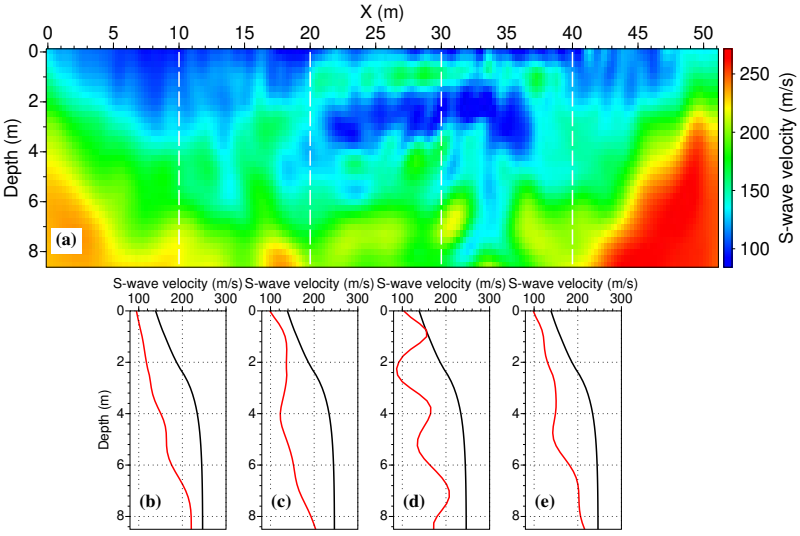

Figure 6.8: (a) V_S model obtained by FWI applied to data as in Figure 6.4c. (b) Comparison between the 1D inverted Vs profile from FWI (red line) and the 1D initial Vs profile from MASW (black line) at x = 10 m; (c-e) the same as (b), but for x = 20 m, 30 m, 40 m, respectively. These lateral positions are indicated with white dashed lines in (a).

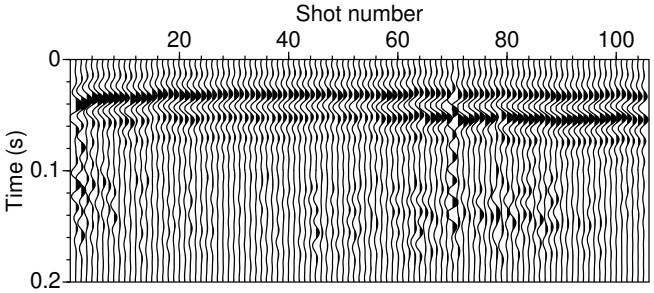

Figure 6.9: Estimated source wavelets for the 105 shot gathers with a frequency band between 5 and 50 Hz.

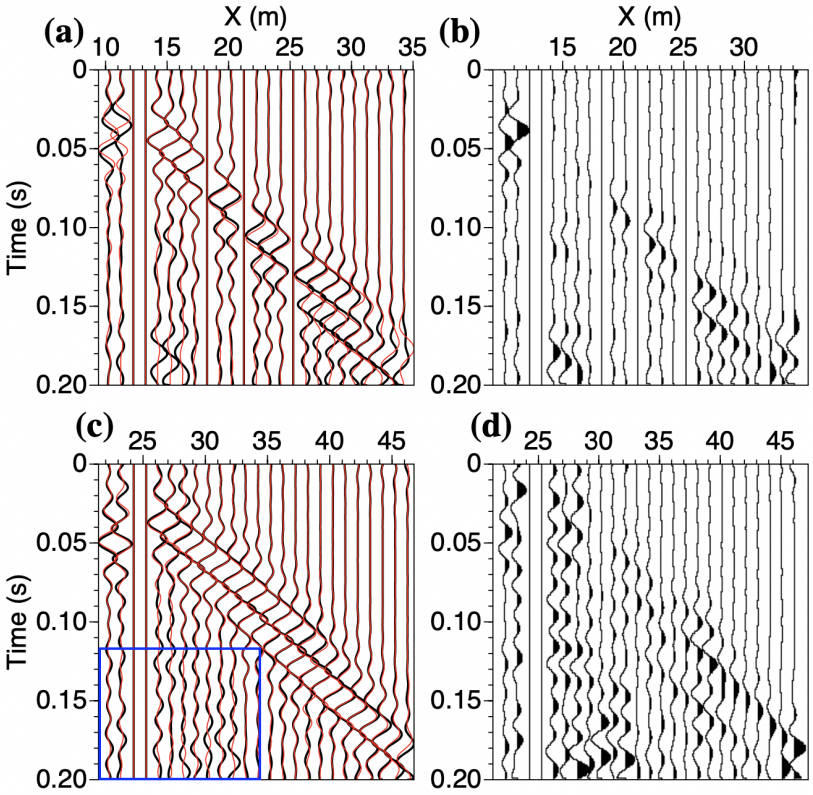

Figure 6.10: (a) The overlay between measured data as in Figure 6.4c (black lines) and synthetic data (red lines) modelled using the inverted Vs model from Figure 6.8a and using the source signatures from Figure 6.9. (b) The residuals between measured and synthetic data in (a). (c-d) Same as in (a-b), but for a source at a different lateral location. Data are band-limited within the frequency range of 5 ~ 50 Hz. Traces are normalized using its maximum value. For visualization purposes, every fourth trace is plotted here.

For comparison, we also run FWI on the preprocessed data as shown in Figure 6.4a, i.e., without suppression of incoherent noise and 3D scattering events. The inverted V_S models for the final frequency bands 5 ~ 50 Hz are displayed in Figures 6.11. In this Figure, we also plot slices of the 1D inverted V_S profile from FWI and the 1D initial V_S profile from MASW at different lateral locations. The overlay between measured wavefield (as in Figure 6.4a), synthetic data associated with the final inverted V_S model, and their residuals are shown in Figure 6.12, whose source positions are the same as the source positions for the shot gathers presented in Figure 6.10. As we can see from Figures 6.12a and 6.12c, the dominant events (mainly Love waves) over all available source-receiver offset ranges match well, without the cycle-skipping problem. However, the weak events in the observed gathers cannot be simulated as those in the synthetic data (blue rectangle in Figure 6.12d). Because these events have been suppressed well in the data as shown in Figures 6.10a and 6.10c by a combination of SVI and non-stationary matching

filtering, we can see a significantly better waveform fitting in the same area (blue rectangle in Figure 6.10d).

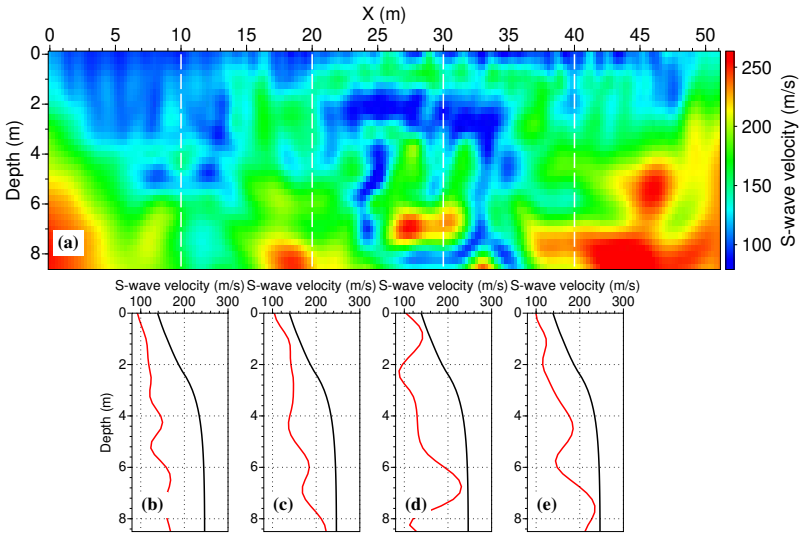

Figure 6.11: (a) V_S model obtained by FWI applied to data as in Figure 6.4a. (b) Comparison between the 1D inverted Vs profile from FWI (red line) and the 1D initial Vs profile from MASW (black line) at x = 10 m; (c-e) the same as (b), but for x = 20 m, 30 m, 40 m, respectively. These lateral positions are indicated by white dashed lines in (a).

The final inversion result from FWI of the dominant Love waves retrieved by SVI and matching filtering is shown in Figure 6.8a. At lateral location 5 ~ 20 m, a low-velocity area (100 ~ 120 m/s) is shown at the shallow depth (0 ~ 2.5 m). Another low-velocity area can also be identified at the lateral position 20 ~ 37 m, which extends to a greater depth (1 ~ 4 m). The final 2D V_S profile obtained from FWI of the preprocessed field data without the suppression of incoherent noise and the 3D scattering events is presented in Figure 6.11a, where two low-velocity anomalies are imaged at similar positions as in Figure 6.8a. Figure 6.13a shows the V_S uncertainties calculated by $(V_1 - V_2)/V_1$, where V_1 denotes the inverted V_S model from Figure 6.8a, V_2 the inverted Vs structure from Figure 6.11a. Areas with low uncertainties can be interpreted with more confidence. For the two low-velocity areas identified in Figure 6.8a and Figure 6.11a, the corresponding V_S uncertainties are low (see Figures 6.13b and 6.13d). This means that these low-velocity areas are constrained well. Since we do not have any other subsurface information about this area, the final interpretation of these low-velocity areas has to be corroborated by other independent archaeological investigations.

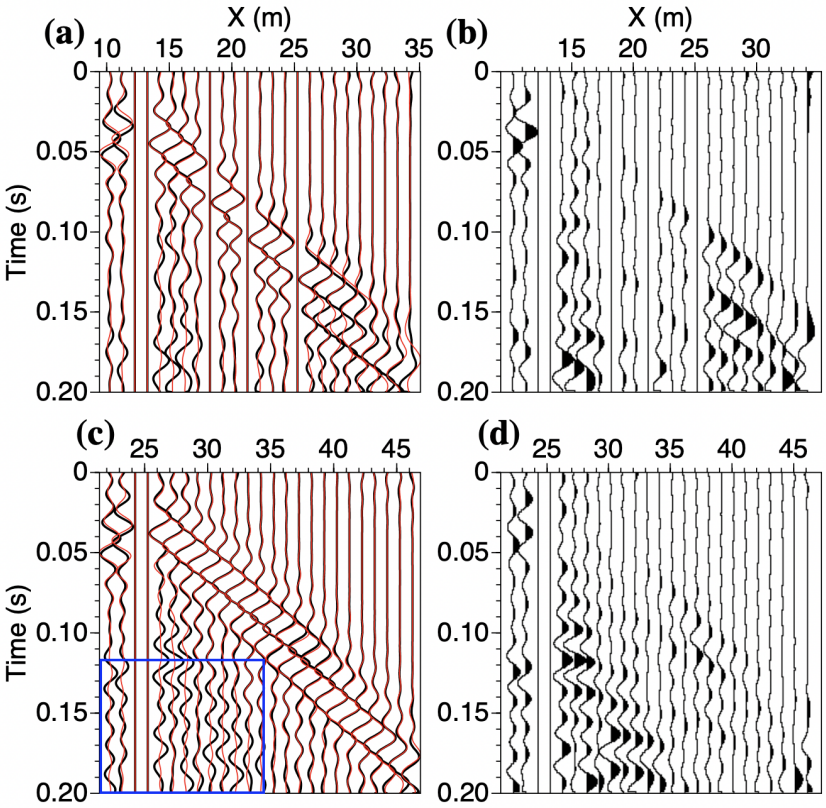

Figure 6.12: (a) The overlay between measured data as in Figure 6.4a (black lines) and synthetic data (red lines) modelled using the inverted Vs model from Figure 6.11a. (b) The residuals between measured and synthetic data in (a). (c-d) Same as in (a-b), but for a source at a different lateral location. Data are band-limited within the frequency range of 5 ~ 50 Hz. Each trace is normalized using its maximum value. For visualization purposes, every fourth trace is plotted here.

6.4. CONCLUSIONS

We proposed a complete 2D elastic full-waveform inversion (FWI) workflow for the inversion of near-surface propagating Love waves. To mitigate the artifacts caused by seismic noise and the 3D events scattered from objects from the crossline direction, we proposed to make use of a combination of super-virtual interferometry (SVI) and matching filtering to accurately retrieve the dominant inline surface waves (Love waves). We then applied 2D elastic SH-FWI to the retrieved Love-wave waveforms to deduce a high-resolution S-wave velocity model of the subsurface structure. The results showed that our workflow is stable; the results can be interpreted together with the model inferred from the inversion of the original data to mitigate the potential misinterpretation of artifacts caused by 3D effects.

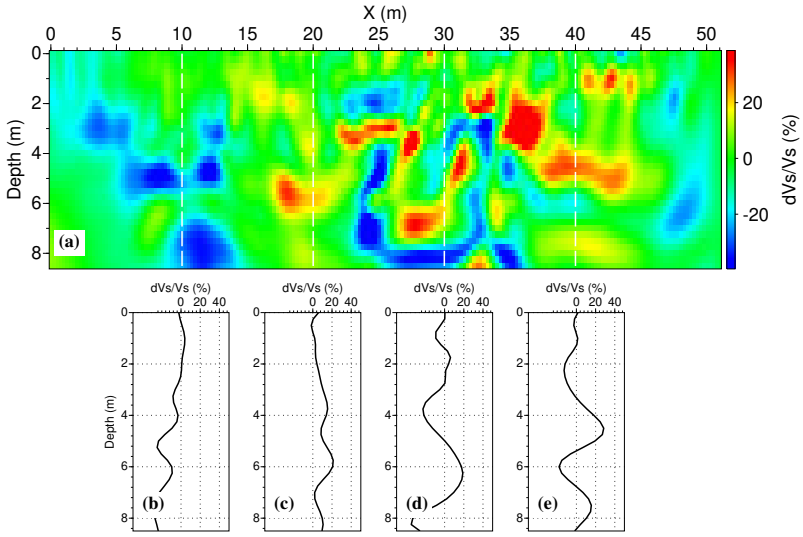

Figure 6.13: (a) V_S uncertainties calculated by $(V_1 - V_2)/V_1$, where V_1 denotes the inverted V_S model from Figure 6.8a, V_2 the inverted V_S model from Figure 6.11a. (b) Slice of 1D-estimated Vs uncertainties at x = 10 m from (a); (c-e) the same as (b) but at x = 20 m, 30 m, 40 m, respectively.

7

CONCLUSIONS AND RECOMMENDATIONS

7.1. CONCLUSIONS

The primary research goal of this thesis was to develop methods for a more reliable localization/characterization of near-surface buried objects at archaeological sites using advanced seismic approaches. For near-surface seismic applications, the data are normally dominated by strong surface waves (SWs). Beneath these SWs, there are reflections and diffractions. In this Ph.D. dissertation, we first aim to reveal these hidden signals (reflections, diffractions) from behind the SWs and then use them for imaging specific structures (reflectors and small-size buried objects). In the later part of this thesis, we try to make use of SWs for near-surface imaging, which is regarded as noise in the first half of this thesis. The technologies that we have developed in this research are mainly aimed for archaeological site investigations. Nevertheless, they can also be used for urban site investigations. In the following, we will outline the conclusions of each chapter.

In chapter 2, we have attempted to overcome the challenge that limits the application of high-resolution reflection seismic for imaging subsurface shallow reflectors in sites covered by soft soil. Source-coherent SWs and/or other linear moveout noises (LMON) are often dominant in the field data and camouflage the shallow reflection events. We develop new schemes for the data-driven suppression of such surface-wave noise and LMON, while preserving the shallow reflections. This is achieved using seismic interferometry (SI) and adaptive subtraction (AS). Comparing with the traditional frequency-wavenumber ($f-k$) filtering method for surface-wave suppression, the advantages of our methods are that: (1) they can retrieve the dominant SWs from field data in a data-driven manner, no subsurface velocity details or other input parameters are needed; (2) they work well in the situation where the surface-wave noise and reflection signals have similar velocity and frequency content. However, this new approach requires that shot and receiver should coexist at the same position for a successful AS. Using numerical modelling data, we have shown how a combination of SI and AS can significantly sup-

press the inline (source-coherent) SWs and LMON and, hence, improve significantly the imaging of shallow subsurface structures. We apply our schemes to a part of the field dataset recorded at an archaeological site located at Dreumel, central Netherlands. We find that crisp and clear shallow reflection events can be revealed, due to significant suppression of LMON as a result of application of our newly developed SI and AS schemes.

In chapters 3 and 4, we have proposed a new approach for detecting/locating subsurface small-size objects using masked diffractions. Detecting small-size objects is a primary challenge at archaeological sites due to the high degree of heterogeneity present in the near-surface. Although high-resolution reflection seismic imaging (main content in chapter 3) can deliver the target resolution of the subsurface in near-surface settings, the standard processing (common-midpoint stacking) for obtaining an image of the subsurface is not suitable to map local diffractors. The reasons are: (1) shallow seismic-reflection data are often dominated by strong SWs that might cover the weaker diffractions; (2) traditional common midpoint moveout corrections are only optimal for the reflection events. Therefore, we propose a seismic-interferometry workflow that can detect/locate shallow subsurface objects using masked diffractions hidden beneath the dominant SWs. This workflow includes three main steps: (1) suppress the dominant SWs in a data-driven way by a combination of SI and AS; (2) enhance further the revealed weak diffraction signals through crosscoherence-based super-virtual interferometry (SVI); (3) produce a diffraction section by a spatial summation of the revealed diffraction energy. The phase-weighted stacking (PWS) technology is introduced to facilitate the coherent summation of weak diffraction signals. Using synthetic data, we show that our approach is robust in locating diffractions from data dominated by strong SWs. We then test our method on field data acquired at Epe-Niersen barrow alignment, an archaeological site located in Veluwe, the Netherlands. The resulting distribution of shallow diffractors agrees with the location of a suspected ancient burial, which was earlier detected in an independent magnetic survey and corings. However, our workflow for diffractor detection only works for SH-waves. Besides, the estimated depths of the detected small-size objects have inherent uncertainty, while the lateral locations of these objects are well constrained.

In chapter 5, we have developed an amplitude-unbiased coherency measure as a misfit function that can be incorporated into full-waveform inversion (FWI) for near-surface characterization of subsurface objects. In recent years, 2D elastic FWI has evolved into a promising tool for various near-surface investigations. However, the field-data application of FWI for near-surface prospecting is still not very common. Traditional FWI suffers from severe local minima problems in case of the presence of dominant SWs. Besides, recorded wavefields are often characterized by amplitude errors due to varying source/receiver coupling and insufficient 3D-to-2D geometry spreading correction. The use of phase information in the FWI has great potential in tackling such challenges. Such coherency is earlier used in chapters 3 and 4 for enhancing the stacking of weak but coherent diffraction signals. Using the adjoint-state method, we offer the details on how to calculate efficiently the gradient of this new misfit function. The benefits of our new misfit function are that: (1) it can extract information uniformly over seismic signals (SWs, reflections, and diffractions); and (2) it is robust to field-data application when the amplitude of recorded wavefields are inaccurate. We then apply this new FWI approach

to a field dataset recorded at an archaeological site located in the ancient Ostia, Italy. The goal of this survey was to map the unexcavated archaeological remains with high resolution. The locality is known to contain a tumulus buried under a shallow soil cover. We could identify the tumulus in our FWI results. The inverted velocity sections from the new FWI also show that the subsurface of this unexcavated part of the archaeological site of Ostia has a high degree of heterogeneity, with the likely presence of small objects in the shallow subsurface. Our results suggest that FWI based on the instantaneous-phase coherency method can be a promising noninvasive tool for archaeological site investigation.

In chapter 6, we propose a complete workflow that can determine subsurface S-wave velocity models inverted from 2D near-surface seismic data more stably, while the artifacts are caused by incoherent noise and 3D scattering events would be significantly suppressed. The field data acquired in 2D seismic surveys have generally been contaminated with scattered energy from out-of-plane objects and other incoherent noise. In the procedure of FWI, the algorithm tries to mimic these events, which may lead to the appearance of spurious heterogeneities or artefacts in the resulting 2D model. To solve such challenges associated with 2D seismic surveys, we make use of a combination of SVI and matching filters to accurately retrieve dominant SWs from the inline direction, while the incoherent noise and 3D scattering events are significantly suppressed. The subsurface structures obtained from inverting retrieved data show similar structures to those visible in seismic section obtained from the original data. We apply this new method to a field dataset recorded at an archaeological site located at Dreumel, central Netherlands. The purpose of this survey was to locate/characterize with a high resolution the presence of ancient boats that were anticipated to be buried under shallow soil covers at this site. Our results show that the workflow is stable; the results can be interpreted together with the velocity models obtained by the inversion of original data, in order to mitigate the potential misinterpretation of artifacts caused by the 3D effects. Two low-velocity areas can be identified in our inverted velocity fields, which might correspond to meaningful subsurface structures of archaeological significance.

7.2. RECOMMENDATIONS

Our results suggest that for reliable location and depth estimation of the meaningful seismic diffractors at archaeological sites, it is advisable to perform in the future 3D seismic surveys as opposed to 2D ones. In those cases, most of the techniques that have been developed in this research will still be useful. The FWI scheme needs to be adapted for handling high-resolution 3D data and the associated computational challenges. Secondly, independent ground truthing is very important in order to attach credibility to seismic interpretations and for the learning purpose. Third, although in FWI we have concentrated primarily on the information contained in the surface waves, in the future more attention paid on using both surface waves and body waves should improve the resolution further. Fourth, a more rigorous, data-driven compensation of intrinsic attenuation of seismic waves in the near-surface is necessary for a better illumination of the relatively greater depths of the shallow subsoil at archaeological sites. Finally, use of a broader seismic frequency band in data than what we have used, and more recent concepts to avoid local minima and cycle-skipping problems in FWI will be beneficial to

further improve the efficiency and accuracy of the methods developed in this research.

A

NON-STATIONARY MATCHING FILTER ESTIMATION

Matched filtering is a method to measure the time-varying differences between two signals [Fomel, 2009]. In this thesis, we use it for adaptive subtraction of surface waves. Consider two time series — prediction $\mathbf{p}(t)$ and observation $\mathbf{b}(t)$. A stationary matching filter $\mathbf{f}(\gamma)$ can be obtained by stretching $\mathbf{p}(t)$ to different scales in order to match $\mathbf{p}(t)$ and $\mathbf{d}(t)$. This can be formalized as the following least-squares inversion problem:

$$\min \left| \sum_{\gamma} \mathbf{p}(\gamma t) * \mathbf{f}(\gamma) - \mathbf{d}(t) \right|^2, \tag{A.1}$$

where $*$ denotes the convolution operator, γ is a stretching variable. For a particular value of the stretching variable γ, equation A.1 gives a single measurement $\mathbf{f}(\gamma)$ for all time coordinates. To handle non-stationary seismic data, a time-varying matching filter $\mathbf{f}(\gamma, t)$ is needed. As equation A.1 shows, this $\mathbf{f}(\gamma, t)$ can be obtained by minimizing the following objective function:

$$\min \left| \sum_{\gamma} \mathbf{p}(\gamma t) * \mathbf{f}(\gamma, t) - \mathbf{d}(t) \right|^2. \tag{A.2}$$

Equation A.2 is an ill-posed problem because it contains more unknown variables than constraints. One remedy is to add additional constraints, i.e., regularization, to constrain the variability of the filter coefficients. With shaping regularization [Fomel, 2007], equation A.2 can be solved as

$$\mathbf{f}(\gamma, t) = \left[\lambda^2 \mathbf{I} + \mathbf{S}\left(\mathbf{P}^T \mathbf{P} - \lambda^2 \mathbf{I}\right)\right]^{-1} \mathbf{S}\mathbf{P}^T \mathbf{d}, \tag{A.3}$$

where λ is a scaling coefficient , which is defined as $\lambda = |\mathbf{p}(t)|^2$. $\mathbf{P}$ is the data matrix composed of $\mathbf{p}(\gamma t)$. $\mathbf{S}$ denotes the shaping operator, which is chosen as a triangular smoothing operator in this thesis.

B

PHASE-WEIGHTED STACKING METHOD

Phase-weighted stacking (PWS) is a technique first proposed by Schimmel and Paulssen [1997] to detect weak but coherent arrivals. The basic idea underlying PWS is to suppress those components in the stacked signals, which do not share the same instantaneous phase. Following the notations from Schimmel and Paulssen [1997], a complex trace $S(t)$ is constructed from a seismic trace $s(t)$ and its Hilbert transform $\mathscr{H}[s(t)]$:

$$S(t) = s(t) + i\mathscr{H}(s(t)), \tag{B.1}$$

which can also be expressed by amplitude $A(t)$ and instantaneous phase $\Phi(t)$:

$$S(t) = A(t)e^{i\phi(t)}, \tag{B.2}$$

where

$$A(t) = \sqrt{s^2(t) + \mathscr{H}^2(s(t))}, \tag{B.3}$$

and

$$\Phi(t) = \arctan\frac{\mathscr{H}(s(t))}{s(t)}. \tag{B.4}$$

Schimmel and Paulssen [1997] define the following **phase stack** $c(t)$, where no amplitudes of complex traces are explicitly involved:

$$c(t) = \frac{1}{N}\left|\sum_{j=1}^{N} e^{i\phi_j(t)}\right|, \tag{B.5}$$

where N is the number of traces involved in stacking, j is the index of each trace. The amplitude of the phase stack $c(t)$ varies between 0 and 1, as schematically illustrated in Figure B.1. As shown in Figure B.1a, the amplitude of $c(t)$ equals 1 when the instantaneous phase of each of the two traces are exactly the same (coherent) at time t. On the

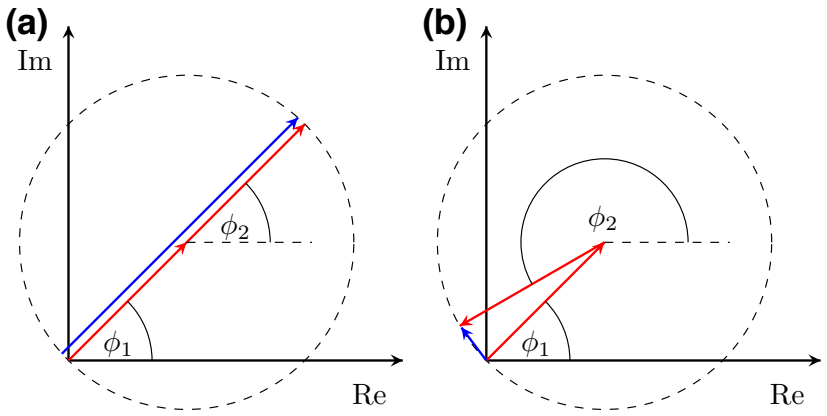

Figure B.1: Illustrations of the summation of $exp[i\phi_1(t)]$ and $exp[i\phi_2(t)]$ in the complex plane. Red arrows denote these two vectors, while the blue arrow is the addition of these two vectors. (a) When two signals have the same instantaneous phase ($\phi_1(t) = \phi_2(t)$), the amplitude of the phase sum (blue arrow) will be 2, and the corresponding value of $c(t)$ will be 1. (b) When two signals have significantly different instantaneous phases, the amplitude of the phase sum (blue arrow) and the corresponding value of $c(t)$ will be approximately 0. Modified from Schimmel and Paulssen [1997].

other hand, when the instantaneous phase of each of the two traces varies quite significantly, $c(t)$ will be approximately 0 (Figure B.1b). Thus, we can use the phase stack to weight the summation of all the traces as follows:

$$g(t) = \frac{[c(t)]^{\nu}}{N} \sum_{j=1}^{N} s_j(t). \tag{B.6}$$

In equation B.6, $[c(t)]^{\nu}$ is used to enhance the coherent signals, that is, signals with similar phase. The exponent ν controls the transition between more coherent and less coherent signal summations. In our research we use $\nu = 2$, as suggested by Schimmel and Paulssen [1997]. When ν equals 0, equation B.6 reduces to the conventional linear stack.

C

GRADIENT FOR INSTANTANEOUS-PHASE COHERENCE

The gradient for the misfit function based on the exponential phase ($e^{i\phi}$) difference is given in Luo et al. [2018] and Yuan et al. [2020]. Our new misfit function utilizes the exponential phase to measure the coherency between the recorded and the synthetic data. Following these earlier works, we present here the details on how to derive the gradient of the misfit defined in equation 5.10 with respect to model parameters $\vec{m}$.

The instantaneous-phase coherence misfit function defined in equation 5.10 can be expanded as

$$
\begin{aligned}
J_2(t) &= \frac{1}{4}\sum_{s,r}\int_0^T \left\{ \left| e^{i\phi_1(t)} - e^{i\phi_2(t)} \right|^2 - \left| e^{i\phi_1(t)} + e^{i\phi_2(t)} \right|^2 \right\} dt \\
&= \frac{1}{4}\sum_{s,r}\int_0^T \left| \frac{d(t) + i\mathcal{H}\{d(t)\}}{A_1(t))} - \frac{s(t) + i\mathcal{H}\{s(t)\}}{A_2(t))} \right|^2 dt \\
&- \frac{1}{4}\sum_{s,r}\int_0^T \left| \frac{d(t) + i\mathcal{H}\{d(t)\}}{A_1(t))} + \frac{s(t) + i\mathcal{H}\{s(t)\}}{A_2(t))} \right|^2 dt \\
&= \frac{1}{4}\sum_{s,r}\int_0^T \left\{ \left| \frac{d(t)}{A_1(t)} - \frac{s(t)}{A_2(t))} \right|^2 + \left| \frac{\mathcal{H}\{d(t)\}}{A_1(t)} - \frac{\mathcal{H}\{s(t)\}}{A_2(t)} \right|^2 \right\} dt \\
&- \frac{1}{4}\sum_{s,r}\int_0^T \left\{ \left| \frac{d(t)}{A_1(t)} + \frac{s(t)}{A_2(t))} \right|^2 + \left| \frac{\mathcal{H}\{d(t)\}}{A_1(t)} + \frac{\mathcal{H}\{s(t)\}}{A_2(t)} \right|^2 \right\} dt. \qquad \text{(C.1)}
\end{aligned}
$$

where $\sum_{s,r}$ represents summation over all available sources and receivers, and T is the recording time. $d(t)$, $s(t)$ are measured and synthetic data. $e^{i\phi_1(t)}$ and $e^{i\phi_2(t)}$ are the exponential phase of the measured and the synthetic data. $A_1(t)$ and $A_2(t)$ are the instantaneous amplitude of the measured and the synthetic data, respectively. $\mathcal{H}$ denotes

the Hilbert transform. To simplify this expression, $R_1(t)$, $I_1(t)$, $R_2(t)$, $I_2(t)$ can be introduced as follows:

$$\begin{cases} R_1(t) = \frac{d(t)}{A_1(t)} - \frac{s(t)}{A_2(t))}, & I_1(t) = \frac{\mathscr{H}\{d(t)\}}{A_1(t)} - \frac{\mathscr{H}\{s(t)\}}{A_2(t)}; \\ R_2(t) = \frac{d(t)}{A_1(t)} + \frac{s(t)}{A_2(t))}, & I_2(t) = \frac{\mathscr{H}\{d(t)\}}{A_1(t)} + \frac{\mathscr{H}\{s(t)\}}{A_2(t)}. \end{cases} \tag{C.2}$$

Equation C.1 can thus be further rewritten as

$$J_2(t) = \frac{1}{4}\sum_{s,r}\int_0^T \Big\{R_1^2(t) + I_1^2(t) - R_2^2(t) - I_2^2(t)\Big\}dt. \tag{C.3}$$

The derivative of the misfit function defined in equation C.3 can be written as

$$\delta J_2 = \frac{1}{2}\sum_{s,r}\int_0^T \Big\{R_1(t)\delta R_1(t) + I_1(t)\delta I_1(t) - R_2(t)\delta R_2(t) - I_2(t)\delta I_2(t)\Big\}dt. \tag{C.4}$$

Note that:

$$\begin{cases} \delta R_2(t) = -\delta R_1(t) = \delta\Big(\frac{s(t)}{A_2(t)}\Big); \\ \delta I_2(t) = -\delta I_1(t) = \delta\Big(\frac{\mathscr{H}\{s(t)\}}{A_2(t)}\Big). \end{cases} \tag{C.5}$$

Substituting equation C.5 into equation C.4, we get

$$\delta J_2 = -\sum_{s,r}\int_0^T \left\{\frac{d(t)}{A_1(t)}\delta\Big(\frac{s(t)}{A_2(t)}\Big) + \frac{\mathscr{H}\{d(t)\}}{A_1(t)}\delta\Big(\frac{\mathscr{H}\{s(t)\}}{A_2(t)}\Big)\right\}dt. \tag{C.6}$$

Next, we present the details on how to evaluate $\delta\Big(\frac{s(t)}{A_2(t)}\Big)$ and $\delta\Big(\frac{\mathscr{H}\{s(t)\}}{A_2(t)}\Big)$.

$$\begin{aligned} \delta\Big(\frac{s(t)}{A_2(t)}\Big) &= \delta\Big(\frac{s(t)}{\sqrt{s^2(t)+\mathscr{H}^2\{s(t)\}}}\Big) \\ &= \frac{\delta s(t)\sqrt{s^2(t)+\mathscr{H}^2\{s(t)\}}}{s^2(t)+\mathscr{H}^2\{s(t)\}} - \frac{\delta s(t)s^2(t) + s(t)\mathscr{H}\{s(t)\}\delta(\mathscr{H}\{s(t)\})}{\Big[s^2(t)+\mathscr{H}^2\{s(t)\}\Big]^{\frac{3}{2}}} \\ &= \frac{\cancel{\delta s(t)s^2(t)} + \delta s(t)\mathscr{H}^2\{s(t)\} - \cancel{\delta s(t)s^2(t)} - s(t)\mathscr{H}\{s(t)\}\delta(\mathscr{H}\{s(t)\})}{\Big[s^2(t)+\mathscr{H}^2\{s(t)\}\Big]^{\frac{3}{2}}} \\ &= \frac{\delta s(t)\mathscr{H}^2\{s(t)\} - s(t)\mathscr{H}\{s(t)\}\delta(\mathscr{H}\{s(t)\})}{\Big[s^2(t)+\mathscr{H}^2\{s(t)\}\Big]^{\frac{3}{2}}}. \end{aligned} \tag{C.7}$$

Here, we make use of two properties of the Hilbert transform as also presented in Yuan et al. [2015]:

$$\begin{cases} \delta\mathscr{H}\{s(t)\} = \mathscr{H}\{\delta s(t)\}; \\ \big\langle\mathscr{H}\{s_1(t)\}, s_2(t)\big\rangle = -\big\langle s_1(t), \mathscr{H}\{s_2(t)\}\big\rangle. \end{cases} \tag{C.8}$$

Thus, the second part of the numerator in equation C.7 can be rewritten as

$$s(t)\mathcal{H}\{s(t)\}\delta(\mathcal{H}\{s(t)\}) = s(t)\mathcal{H}\{s(t)\}\mathcal{H}\{\delta s(t)\}$$
$$= -\mathcal{H}\Big\{s(t)\mathcal{H}\{s(t)\}\Big\}\delta s(t). \tag{C.9}$$

Substituting equation C.9 into equation C.7, we get

$$\delta\Big(\frac{s(t)}{A_2(t)}\Big) = \frac{\mathcal{H}^2\{s(t)\} + \mathcal{H}\Big\{s(t)\mathcal{H}\{s(t)\}\Big\}}{\Big[s^2(t) + \mathcal{H}^2\{s(t)\}\Big]^{\frac{3}{2}}}\delta s(t). \tag{C.10}$$

Similarity, $\delta\Big(\frac{\mathcal{H}\{s(t)\}}{A_2(t)}\Big)$ can be obtained as

$$\delta\Big(\frac{\mathcal{H}\{s(t)\}}{A_2(t)}\Big) = \frac{-\mathcal{H}\{s^2(t)\} - s(t)\mathcal{H}\{s(t)\}}{\Big[s^2(t) + \mathcal{H}^2\{s(t)\}\Big]^{\frac{3}{2}}}\delta s(t). \tag{C.11}$$

Substituting equations C.10 and C.11 into equation C.6 and rearranging the orders we have the gradient for the misfit function defined in equation 5.10 as

$$\delta J_2 = \sum_{s,r}\int_0^T \Big[\frac{s(t)\mathcal{H}\{d(t)\}\mathcal{H}\{s(t)\}}{A_1(t)A_2^3(t)} - \frac{d(t)\mathcal{H}^2\{s(t)\}}{A_1(t)A_2^3(t)}\Big]\delta s(t)dt$$
$$+\sum_{s,r}\int_0^T \Big[\mathcal{H}\Big\{\frac{s^2(t)\mathcal{H}\{d(t)\}}{A_1(t)A_2^3(t)} - \frac{d(t)s(t)\mathcal{H}\{s(t)\}}{A_1(t)A_2^3(t)}\Big\}\Big]\delta s(t)dt. \tag{C.12}$$

C

REFERENCES

Aki, K., and P. G. Richards, 2002, Quantitative seismology.

An, S., and T. Hu, 2016, Suppression of seismic surface waves based on adaptive weighted super-virtual interferometry: Science China Earth Sciences, **59**, 2179–2188.

Angelo, P., 2016, Ground penetrating radar experiments for high school students, https://creep-it.gm.univ-montp2.fr/outreach-5/, accessed 15 may 2022.

Bailey, J. T., S. Evans, and G. de Q. Robin, 1964, Radio echo sounding of polar ice sheets: Nature, **204**, 420–421.

Balestrini, F., D. Draganov, A. Malehmir, P. Marsden, and R. Ghose, 2019, Improved target illumination at Ludvika mines of Sweden through seismic-interferometric surface-wave suppression: Geophysical Prospecting, **68**, 200–213.

Bekara, M., and M. van der Baan, 2007, Local singular value decomposition for signal enhancement of seismic data: Geophysics, **72**, V59–V65.

Bharadwaj, P., G. Schuster, I. Mallinson, and W. Dai, 2011, Theory of supervirtual refraction interferometry: Geophysical Journal International, **188**, 263–273.

Bohlen, T., 2002, Parallel 3-D viscoelastic finite difference seismic modelling: Computers & Geosciences, **28**, 887–899.

Bourgeois, Q., 2012, Monuments on the horizon: the formation of the barrow landscape throughout the 3rd and 2nd millennium BC: Sidestone Press.

Bourgeois, Q., L. Amkreutz, and R. Panhuysen, 2009, The Niersen Beaker burial: A renewed study of a century-old excavation: Journal of Archaeology in the Low Countries, **1**, 83–105.

Boyce, J. I., E. G. Reinhardt, A. Raban, and M. R. Pozza, 2004, Marine magnetic survey of a submerged Roman Harbour, Caesarea Maritima, Israel: International Journal of Nautical Archaeology, **33**, 122–136.

Bozdağ, E., J. Trampert, and J. Tromp, 2011, Misfit functions for full waveform inversion based on instantaneous phase and envelope measurements: Geophysical Journal International, **185**, 845–870.

Bracewell, R. N., and R. N. Bracewell, 1986, The Fourier transform and its applications: McGraw-Hill New York.

Brouwer, J., R. Ghose, K. Helbig, and V. Nijhof, 1997, The improvement of geotechnical subsurface models through the application of S-wave reflection seismic exploration: 3rd EEGS Meeting, European Association of Geoscientists & Engineers, cp–95–00027.

Bunks, C., F. M. Saleck, S. Zaleski, and G. Chavent, 1995, Multiscale seismic waveform inversion: Geophysics, **60**, 1457–1473.

Cai, A., and C. A. Zelt, 2019, Data weighted full-waveform inversion with adaptive moment estimation for near-surface seismic refraction data: SEG Technical Program Expanded Abstracts 2019, Society of Exploration Geophysicists, 2858–2862.

Cheng, F., D. Draganov, J. Xia, Y. Hu, and J. Liu, 2018, Q-estimation using seismic interferometry from vertical well data: Journal of Applied Geophysics, **159**, 16–22.

Consoli, R. H., 2013, World history encyclopedia: Ostia, www.worldhistory.org/ostia, accessed 3 March 2022.

Dai, W., T. Fei, Y. Luo, and G. T. Schuster, 2011, Super-virtual interferometric diffractions as guide stars: SEG Technical Program Expanded Abstracts 2011, Society of Exploration Geophysicists, 3819–3823.

Dogan, M., and S. Papamarinopoulos, 2003, Geoelectric prospection of a city wall by multi-electrode resistivity image survey at the prehistoric site of Asea (southern Greece): Archaeological Prospection, **10**, 241–248.

Dokter, E., D. Köhn, D. Wilken, D. D. Nil, and W. Rabbel, 2017, Full waveform inversion of SH- and Love-wave data in near-surface prospecting: Geophysical Prospecting, **65**, 216–236.

Dong, S., R. He, and G. T. Schuster, 2006, Interferometric predcition and least squares subtraction of surface waves: SEG Technical Program Expanded Abstracts 2006, Society of Exploration Geophysicists, 2783–2786.

Draganov, D., R. Ghose, K. Heller, and E. Ruigrok, 2012a, Monitoring changes in velocity and Q using non-physical arrivals in seismic interferometry: Geophysical Journal International, **192**, 699–709.

Draganov, D., K. Heller, and R. Ghose, 2012b, Monitoring CO2 storage using ghost reflections retrieved from seismic interferometry: International Journal of Greenhouse Gas Control, **11**, S35–S46.

Draganov, D., K. Wapenaar, and J. Thorbecke, 2006, Seismic interferometry: Reconstructing the earth's reflection response: Geophysics, **71**, SI61–SI70.

Eckart, C., and G. Young, 1936, The approximation of one matrix by another of lower rank: Psychometrika, **1**, 211–218.

Fichtner, A., B. L. N. Kennett, H. Igel, and H.-P. Bunge, 2008, Theoretical background for continental- and global-scale full-waveform inversion in the time-frequency domain: Geophysical Journal International, **175**, 665–685.

Fichtner, A., and J. Trampert, 2011, Resolution analysis in full waveform inversion: Geophysical Journal International, **187**, 1604–1624.

Fomel, S., 2007, Shaping regularization in geophysical-estimation problems: Geophysics, **72**, R29–R36.

———, 2009, Adaptive multiple subtraction using regularized nonstationary regression: Geophysics, **74**, V25–V33.

Forbriger, T., L. Groos, and M. Schäfer, 2014, Line-source simulation for shallow-seismic data. Part 1: theoretical background: Geophysical Journal International, **198**, 1387–1404.

GeoScan, 2022, Electrical resistivity, https://www.geoscan.ca/methods/electrical-resistance/, accessed 15 may 2022.

Ghose, R., 2002, High-frequency shear wave reflections from shallow subsoil layers using a vibrator source: Sweep cross-correlation versus deconvolution with groundforce derivative: SEG Technical Program Expanded Abstracts 2002, Society of Exploration Geophysicists, 1408–1411.

———, 2003, High-frequency shear-wave reflections to monitor lateral variations in soil, supplementing downhole geotechnical tests: *in* J. Saveur, ed., Reclaiming the underground space: Swets & Zeitlinger, 827–833.

———, 2012, A microelectromechanical system digital 3C array seismic cone penetrometer: Geophysics, **77**, WA99–WA107.

Ghose, R., J. Brouwer, and V. Nijhof, 1996, A portable S-wave vibrator for high-resolution imaging of the shallow subsurface: 58th EAEG Meeting, EAGE Publications BV, cp–48–00132.

Ghose, R., J. Carvalho, and A. Loureiro, 2013, Signature of fault zone deformation in near-surface soil visible in shear wave seismic reflections: Geophysical Research Letters, **40**, 1074–1078.

Ghose, R., and J. Goudswaard, 2004, Integrating S-wave seismic-reflection data and cone penetration test data using a multiangle multiscale approach: Geophysics, **69**, 440–459.

Ghose, R., J. Liu, D. Draganov, D. Ngan-Tillard, M. Warnaar, J. Brackenhoff, J. van den Berg, and H. Stoger, 2020, Ultra-shallow shear-wave reflections locating near-surface buried structures in the unexcavated southern Fringe of the ancient Ostia, Rome, *in* H. Kamermans, L. Bouke van der Meer, eds., Designating Place: archaeological perspectives on built environments in Ostia and Pompeii: Archaeological Studies Leiden University (ASLU) 50, 51–62.

Ghose, R., V. Nijhof, J. Brouwer, Y. Matsubara, Y. Kaida, and T. Takahashi, 1998, Shallow to very shallow, high-resolution reflection seismic using a portable vibrator system: Geophysics, **63**, 1295–1309.

Gibson, T. H., 1986, Magnetic prospection on prehistoric sites in Western Canada: Geophysics, **51**, 553–560.

Goodman, D., and Y. Nishimura, 1993, A ground-radar view of Japanese burial mounds: Antiquity, **67**, 349–354.

Groos, L., M. Schäfer, T. Forbriger, and T. Bohlen, 2017, Application of a complete workflow for 2D elastic full-waveform inversion to recorded shallow-seismic Rayleigh waves: Geophysics, **82**, R109–R117.

Guitton, A., and D. J. Verschuur, 2004, Adaptive subtraction of multiples using the L1-norm: Geophysical Prospecting, **52**, 27–38.

Halliday, D. F., A. Curtis, J. O. A. Robertsson, and D.-J. van Manen, 2007, Interferometric surface-wave isolation and removal: Geophysics, **72**, A69–A73.

Hasbrouck, W. P., 1991, Four shallow-depth, shear-wave feasibility studies: Geophysics, **56**, 1875–1885.

Jongerius, P., and K. Helbig, 1988, Onshore high-resolution seismic profiling applied to sedimentology: GEOPHYSICS, **53**, 1276–1283.

Kallweit, R. S., and L. C. Wood, 1982, The limits of resolution of zero-phase wavelets: Geophysics, **47**, 1035–1046.

Kamei, R., T. Miyoshi, R. G. Pratt, M. Takanashi, and S. Masaya, 2015, Application of waveform tomography to a crooked-line 2D land seismic data set: Geophysics, **80**, B115–B129.

Kaslilar, A., U. Harmankaya, K. Wapenaar, and D. Draganov, 2013, Estimating the location of a tunnel using correlation and inversion of Rayleigh wave scattering: Geophysical Research Letters, **40**, 6084–6088.

Kimman, W. P., and J. Trampert, 2010, Approximations in seismic interferometry and their effects on surface waves: Geophysical Journal International, **182**, 461–476.

King, S., and A. Curtis, 2012, Suppressing nonphysical reflections in Green's function estimates using source-receiver interferometry: Geophysics, **77**, Q15–Q25.

Klem-Musatov, K., 1994, Theory of Seismic Diffractions: Society of Exploration Geophysicists.

Komatitsch, D., and R. Martin, 2007, An unsplit convolutional perfectly matched layer improved at grazing incidence for the seismic wave equation: Geophysics, **72**, SM155–SM167.

Konstantaki, L., D. Draganov, R. Ghose, and T. Heimovaara, 2015a, Seismic interferometry as a tool for improved imaging of the heterogeneities in the body of a landfill: Journal of Applied Geophysics, **122**, 28–39.

Konstantaki, L. A., R. Ghose, D. Draganov, G. Diaferia, and T. Heimovaara, 2015b, Characterization of a heterogeneous landfill using seismic and electrical resistivity data: Geophysics, **80**, EN13–EN25.

Krawczyk, C. M., U. Polom, and T. Beilecke, 2013, Shear-wave reflection seismics as a valuable tool for near-surface urban applications: The Leading Edge, **32**, 256–263.

Köhn, D., T. Meier, M. Fehr, D. D. Nil, and M. Auras, 2016, Application of 2D elastic Rayleigh waveform inversion to ultrasonic laboratory and field data: Near Surface Geophysics, **14**, 461–467.

Köhn, D., D. Wilken, D. D. Nil, T. Wunderlich, W. Rabbel, L. Werther, J. Schmidt, C. Zielhofer, and S. Linzen, 2019, Comparison of time-domain SH waveform inversion strategies based on sequential low and bandpass filtered data for improved resolution in near-surface prospecting: Journal of Applied Geophysics, **160**, 69–83.

Lailly, P., 1983, The seismic inverse problem as a sequence of before stack migrations, *in*: Bednar, J. B., Robinson, E. and Weglein, A., Eds., Conference on inverse scattering – theory and application: SIAM, Philadelphia, 206–220.

Lambers, L., J. W. E. Fassbinder, K. Lambers, and Q. Bourgeois, 2017, The iron-age burial mounds of Epe-Nierson, the Netherlands: results from magnetometry in the range of ± 1.0 nT: 12th International Conference of Archaeological Prospection, 132–134.

Lambot, S., E. Slob, D. Chavarro, M. Lubczynski, and H. Vereecken, 2008, Measuring soil surface water content in irrigated areas of southern tunisia using full-waveform inversion of proximal GPR data: Near Surface Geophysics, **6**, 403–410.

Landa, E., S. Fomel, and T. Moser, 2006, Path-integral seismic imaging: Geophysical Prospecting, **54**, 491–503.

Landa, E., and S. Keydar, 1998, Seismic monitoring of diffraction images for detection of local heterogeneities: Geophysics, **63**, 1093–1100.

Lellouch, A., and M. Reshef, 2017, Shallow diffraction imaging in an SH-wave crosshole configuration: Geophysics, **82**, S9–S18.

Li, J., 2020, Illustration of seismic exploration, http://jlucsim.cn/, accessed 15 may 2022.

Liu, J., Q. Bourgeois, R. Ghose, and D. Draganov, 2019, Detection of near-surface heterogeneities at archaeological sites using seismic diffractions: First Break, **37**, 93–97.

Liu, J., D. Draganov, and R. Ghose, 2018, Seismic interferometry facilitating the imaging of shallow shear-wave reflections hidden beneath surface waves: Near Surface Geophysics, **16**, 372–382.

Liu, J., D. Draganov, R. Ghose, and Q. Bourgeois, 2021, Near-surface diffractor detection at archaeological sites based on an interferometric workflow: Geophysics, **86**, WA1–

WA11.
Liu, J., R. Ghose, and D. Draganov, 2022, Characterizing near-surface structures at the ostia archaeological site based on instantaneous-phase coherency inversion: Geophysics, 1–50.
Luo, J., R.-S. Wu, and F. Gao, 2018, Time-domain full waveform inversion using instantaneous phase information with damping: Journal of Geophysics and Engineering, **15**, 1032–1041.
Mao, J., J. Sheng, and G. Hilburn, 2019, Phase only reflection full-waveform inversion for high resolution model update: SEG Technical Program Expanded Abstracts 2019, Society of Exploration Geophysicists, 1305–1309.
Maurer, H., S. A. Greenhalgh, E. Manukyan, S. Marelli, and A. G. Green, 2012, Receiver-coupling effects in seismic waveform inversions: Geophysics, **77**, R57–R63.
McMechan, G. A., and M. J. Yedlin, 1981, Analysis of dispersive waves by wave field transformation: Geophysics, **46**, 869–874.
Mecking, R., D. Köhn, M. Meinecke, and W. Rabbel, 2021, Cavity detection by SH-wave full-waveform inversion — A reflection-focused approach: Geophysics, **86**, no. 3, WA123–WA137.
Mikesell, D., K. van Wijk, A. Calvert, and M. Haney, 2009, The virtual refraction: Useful spurious energy in seismic interferometry: Geophysics, **74**, A13–A17.
Miller, R. D., and D. W. Steeples, 1994, Applications of shallow high-resolution seismic reflection to various environmental problems: Journal of Applied Geophysics, **31**, 65–72.
Mora, P., 1987, Nonlinear two-dimensional elastic inversion of multioffset seismic data: Geophysics, **52**, 1211–1228.
Nakata, N., R. Snieder, T. Tsuji, K. Larner, and T. Matsuoka, 2011, Shear wave imaging from traffic noise using seismic interferometry by cross-coherence: Geophysics, **76**, SA97–SA106.
Neidell, N. S., and M. T. Taner, 1971, Semblance and other coherency measures for multichannel data: Geophysics, **36**, 482–497.
Ngan-Tillard, D., D. Draganov, M. Warnaar, J. Liu, J. Brackenhoff, J. van den Berg, R. Ghose, A. Veltmeijer, and H. Stöger, 2020, Exploring with GPR the frigidarium of the byzantine baths in Ostia Antica after excavation, backfilling and floor re-tiling, *in* H. Kamermans, L. Bouke van der Meer, eds., Designating Place: archaeological perspectives on built environments in Ostia and Pompeii: Archaeological Studies Leiden University (ASLU) 50, 41–50.
Nguyen, T. D., and K. T. Tran, 2018, Site characterization with 3D elastic full-waveform tomography: Geophysics, **83**, no. 5, R389–R400.
Nocedal, J., and S. Wright, 2006, Numerical optimization: Springer Science & Business Media.
Pan, Y., L. Gao, and T. Bohlen, 2019, High-resolution characterization of near-surface structures by surface-wave inversions: From dispersion curve to full waveform: Surveys in Geophysics, **40**, 167–195.
Peter, R., 2017, Representation of earth's invisible magnetic field, https://www.nasa.gov/mission_pages/sunearth/news/gallery/earths-magneticfieldlines-dipole.html, accessed 15 may 2022.

Peterie, S. L., R. D. Miller, J. Ivanov, and S. D. Sloan, 2020, Shallow tunnel detection using SH-wave diffraction imaging: Geophysics, **85**, EN29–EN37.

Place, J., D. Draganov, A. Malehmir, C. Juhlin, and C. Wijns, 2019, Crosscoherence-based interferometry for the retrieval of first arrivals and subsequent tomographic imaging of differential weathering: Geophysics, **84**, Q37–Q48.

Plessix, R.-E., 2006, A review of the adjoint-state method for computing the gradient of a functional with geophysical applications: Geophysical Journal International, **167**, 495–503.

Pugin, A. J. M., T. H. Larson, S. L. Sargent, J. H. McBride, and C. E. Bexfield, 2004, Near-surface mapping using SH-wave and P-wave seismic land-streamer data acquisition in Illinois, U.S.: The Leading Edge, **23**, 677–682.

Pullan, S. E., J. A. Hunter, and K. G. Neave, 1990, Shallow shear-wave reflection tests: SEG Technical Program Expanded Abstracts 1990, Society of Exploration Geophysicists, 380–382.

Ravaut, C., S. Operto, L. Improta, J. Virieux, A. Herrero, and P. Dell'Aversana, 2004, Multiscale imaging of complex structures from multifold wide-aperture seismic data by frequency-domain full-waveform tomography: application to a thrust belt: Geophysical Journal International, **159**, 1032–1056.

Robertsson, J. O. A., 1996, A numerical free-surface condition for elastic/viscoelastic finite-difference modeling in the presence of topography: Geophysics, **61**, 1921–1934.

Sambridge, M., 1999, Geophysical inversion with a neighbourhood algorithm—I. searching a parameter space: Geophysical Journal International, **138**, 479–494.

Schimmel, M., and H. Paulssen, 1997, Noise reduction and detection of weak, coherent signals through phase-weighted stacks: Geophysical Journal International, **130**, 497–505.

Schimmel, M., E. Stutzmann, and J. Gallart, 2010, Using instantaneous phase coherence for signal extraction from ambient noise data at a local to a global scale: Geophysical Journal International, **184**, 494–506.

Schuster, G. T., 2009, Seismic Interferometry: Cambridge University Press.

Schäfer, M., L. Groos, T. Forbriger, and T. Bohlen, 2014, Line-source simulation for shallow-seismic data. Part 2: full-waveform inversion—a synthetic 2-D case study: Geophysical Journal International, **198**, 1405–1418.

Shapiro, N. M., 2005, High-resolution surface-wave tomography from ambient seismic noise: Science, **307**, 1615–1618.

Shtivelman, V., and S. Keydar, 2005, Imaging shallow subsurface inhomogeneities by 3D multipath diffraction summation: First Break, **23**, 39–42.

Shtivelman, V., S. Keydar, and M. Mikenberg, 2009, Imaging near-surface inhomogeneities using weighted multipath summation: Near Surface Geophysics, **7**, 171–177.

Slob, E., D. Draganov, and K. Wapenaar, 2007, Interferometric electromagnetic Green's functions representations using propagation invariants: Geophysical Journal International, **169**, 60–80.

Smith, C., 2014, Encyclopedia of global archaeology: Springer Reference.

Snieder, R., 2004, Extracting the Green's function from the correlation of coda waves: A derivation based on stationary phase: Physical Review E, **69**, 046610.

Solano, C. A. P., D. Donno, and H. Chauris, 2014, Alternative waveform inversion for sur-

face wave analysis in 2-D media: Geophysical Journal International, **198**, 1359–1372.
Steeples, D. W., and R. D. Miller, 1988, Seismic reflection methods applied to engineering, environmental, and ground-water problems: 1st EEGS Symposium on the Application of Geophysics to Engineering and Environmental Problems, European Association of Geoscientists & Engineers, 1–30.
Sternberg, R. S., 1987, Archaeomagnetism and magnetic anomalies in the American Southwest: Geophysics, **52**, 368–371.
Stockwell, J., and J. K. Cohen, 2002, The new SU user's manual: Center for Wave Phenomena, Colorado School of Mines, Golden, USA.
Taner, M. T., and F. Koehler, 1969, Velocity spectra-digital computer derivation applications of velocity functions: Geophysics, **34**, 859–881.
Tarantola, A., 1984, Inversion of seismic reflection data in the acoustic approximation: Geophysics, **49**, 1259–1266.
TerraDat, 2022, Electrical resistivity tomography, https://www.terradat.co.uk/survey-methods/resistivity-tomography/, accessed 15 may 2022.
Thorbecke, J. W., and D. Draganov, 2011, Finite-difference modeling experiments for seismic interferometry: Geophysics, **76**, H1–H18.
Tran, K. T., M. McVay, M. Faraone, and D. Horhota, 2013, Sinkhole detection using 2D full seismic waveform tomography: Geophysics, **78**, R175–R183.
Tran, K. T., and J. Sperry, 2018, Application of 2D full-waveform tomography on land-streamer data for assessment of roadway subsidence: Geophysics, **83**, EN1–EN11.
Trinks, I., and P. Karlsson, 2007, Ground penetrating radar and magnetometer archaeological prospection at zaltbommel 2007.
Tromp, J., C. Tape, and Q. Liu, 2004, Seismic tomography, adjoint methods, time reversal and banana-doughnut kernels: Geophysical Journal International, **160**, 195–216.
van Dalen, K. N., K. Wapenaar, and D. F. Halliday, 2013, Surface wave retrieval in layered media using seismic interferometry by multidimensional deconvolution: Geophysical Journal International, **196**, 230–242.
Vickers, R. S., and L. T. Dolphin, 1975, A communication on an archaeological radar experiment at Chaco Canyon, New Mexico: MASCA newsletter, **11**, 3–3.
Vigh, D., K. Jiao, D. Watts, and D. Sun, 2014, Elastic full-waveform inversion application using multicomponent measurements of seismic data collection: Geophysics, **79**, R63–R77.
Virieux, J., 1984, SH-wave propagation in heterogeneous media: velocity-stress finite-difference method: Exploration Geophysics, **15**, 265–265.
Virieux, J., and S. Operto, 2009, An overview of full-waveform inversion in exploration geophysics: Geophysics, **74**, WCC1–WCC26.
Walters, S., R. Miller, J. Xia, J. Ivanov, D. Steeples, and C. Zeng, 2009, Detecting tunnels and underground facilities using diffracted P-waves: 22nd EEGS Symposium on the Application of Geophysics to Engineering and Environmental Problems, European Association of Geoscientists & Engineers, 937–942.
Wapenaar, K., D. Draganov, and J. O. A. Robertsson, eds., 2008, Seismic interferometry: History and present status: Society of Exploration Geophysicists.
Wapenaar, K., and J. Fokkema, 2006, Green's function representations for seismic interferometry: Geophysics, **71**, SI33–SI46.

Wathelet, M., 2008, An improved neighborhood algorithm: Parameter conditions and dynamic scaling: Geophysical Research Letters, **35**, L09301.

Wathelet, M., J.-L. Chatelain, C. Cornou, G. D. Giulio, B. Guillier, M. Ohrnberger, and A. Savvaidis, 2020, Geopsy: A user-friendly open-source tool set for ambient vibration processing: Seismological Research Letters, **91**, 1878–1889.

Wynn, J. C., 1986, Archaeological prospection: An introduction to the Special Issue: Geophysics, **51**, 533–537.

Xia, J., R. D. Miller, and C. B. Park, 1999, Estimation of near-surface shear-wave velocity by inversion of Rayleigh waves: Geophysics, **64**, 691–700.

Yilmaz, O., 2001, Seismic Data Analysis: Society of Exploration Geophysicists.

Yuan, Y. O., E. Bozdağ, C. Ciardelli, F. Gao, and F. J. Simons, 2020, The exponentiated phase measurement, and objective-function hybridization for adjoint waveform tomography: Geophysical Journal International, **221**, 1145–1164.

Yuan, Y. O., F. J. Simons, and E. Bozdağ, 2015, Multiscale adjoint waveform tomography for surface and body waves: Geophysics, **80**, R281–R302.

ACKNOWLEDGEMENTS

This thesis is impossible without the direct and indirect contributions from many people during the past five years. I am very grateful to take this chance to acknowledge them.

First and foremost, I am very lucky to have **Ranajit Ghose** and **Deyan Draganov** as my promotors to guide me through the past years. Thank you very much for accepting me to be your student, to learn from you, to make errors, and to improve. I am very grateful to you for all the efforts and time you have put in helping me, especially in helping me come up with new research ideas, answering my questions, giving me almost spontaneous comments on my works, and guiding me through publishing my first English journal paper, etc. After these years, I can see a lot of improvement in myself and I feel more independent and confident than before.

I still remember when I first came to Ranajit's office for the first meeting, I was impressed by his very decent English accent. At that time my English was not good, but I could understand every word he talked to me. He was very kind. Many discussion with him in a friendly and relaxing atmosphere continued for the next five years. Ranajit is very passionate about science and new ideas. He always encouraged me to come up with new ideas and carry out research works that could have an useful and significant impact. In the beginning, that appeared a little hard for me. But under his tremendous and patient guidance, I could begin to ask myself similar questions when I prepared the manuscript for the next paper: what it is new and what useful contribution I could make. This mindset is very precious for me and I believe that I will benefit a lot from it in my future career.

I also recall when I first come to Deyan's office, we had our first talk. I spoke fast and made a lot of pronunciation mistakes (which I realized later). It was very hard for him to understand. But he was very patient during the talk. When we got familiar with each other, he would correct me the wrong words I pronounced and help me pronounce them correctly. Deyan encouraged me to talk slowly so that people could understand me better. Besides, he also offered me tips on how to improve my English. Because of his encouragement and trust in me, my spoken English has improved a lot. Deyan is an expert in seismic interferometry. He was very open to sharing his knowledge with me and encouraged me to create new things. During each talk that we had, he always explained me the complex theory in simple words. I still remember his vivid explanation of the principle of seismic interferometry for the first time to me. Cross-correlation is one of the necessary processing steps in seismic interferometry. To explain how cross-correlation works, he put two hands on the screen and moved his hands in different directions. When two hands overlapped, that meant that the lag in the cross-correlation is zero and the value of cross-correlation of two signals is at its maximum. Through each similar scientific talk with him, he made me feel that scientific stuff is quite interesting and each scientific theory can possibly be explained in such simple terms.

My very special gratitude also goes to **Kees Wapenaar**, for accepting me to study in

this one of the most prestigious Geophysics groups in the world. I am very proud to be a part of this section and will cherish these happy and wonderful memories. In this section, I was surrounded by many excellent scientists. **Guy**, thanks for giving me the chance to join your class as a teaching assistant. From these activities, I began to enjoy sharing knowledge with others. **Jan**, I have made heavy use of the software you developed. By reading your codes, I learnt about the practical aspects of many seismic processing steps. Thanks also go to **Evert Slob**, **Wim Mulder** and other excellent researchers in our section.

I am proud to have **Kees Wapenaar, Wolfgang Rabbel, Läslo Evers, Eric Verschuur, Wim Mulder and Quentin Bourgeois** for being in the committee of my Ph.D. thesis. Thanks for your efforts to kindly read and improve my thesis. I quite enjoyed the field work with **Dominique, Joeri, Martijn, and Jens**, thank you for helping me acquire almost all the field data used in this thesis. After one of the field works in Rome, we took a tour around the gorgeous Rome center, went to the beaches in Ostia. These amazing moments are still vivid to me after these years. I am also grateful to the China Scholarship Council (CSC) for supporting me financially in my Ph.D. project.

Next it is time for me to thank my friends and colleagues. **Karim**, my closest neighbor in the office, thanks for sharing snacks with me on many afternoons. I quite enjoyed each coffee break that we had. **Atsushi**, we had many nice talks about cultural similarities between China and Japan. I also thank you for giving me your waterproof coat, that kept me warm, especially when I was doing fieldwork in the rainy Netherlands. **Juan**, I enjoyed every fieldwork with you. Thanks for your specially designed TUD T-shirt for me, which I like most. **Max**, you are the most knowledgeable people I met, every casual talk with you made me learn something new. **Florencia**, you make our big office full of laughter and have a relaxing atmosphere. **Musab**, your great sense of humor made each talk with you enjoyable. **Nicolas**, I was very impressed by your Python skills, and I enjoyed the teaching-assistant activities that we had together. **Joeri**, you are the most amazing guy that I came to know during my stay in Delft; you showed me the possibility of having a colorful life and doing excellent research at the same time. **Johno**, a very special thanks go to you for translating my summary into Dutch! **Professor Zhou**, thanks for always keeping up with me with the latest job news in China. **Xu**, I had many nice talks with you regarding all topics, especially your experience in the USA. Thank you also to help me set up the screen, which sped up my final thesis writing. **Junhai**, you are one of the best friends I made on this new continent, thanks to you for those numerous invitations by you and **Liyuan**, which made me feel at home. I learned a lot from talks with **Lele**, thanks for sharing with me the knowledge about how a journal paper gets published. **Jingming**, I was very happy when Ranajit told me that you were the next Chinese buddy to join our group. I would also like to thank **Amin**, **Billy**, **Bingkun**, **Faezeh**, **Feng Cheng**, **Jinyu**, **Youwei**, **Yang**, **Shohei**, **Yusuke**, **Santosh**, **Rahul**, etc. Besides, my friends who are now working on other continents, **Jihai**, **Hang**, **Xiansong**, **Munirdin**, **Sheng Wang**, **Xiaogen**, **Zuming**, etc., keeping in touch with you always made me relax. I also appreciate the unfailing assistance of **Lydia**, **Marlijn**, **Nancy** and **Ralf**. Thanks must also go to **Guus** and **Joost** for helping me to access and use our cluster nodes.

I am very lucky to meet my girlfriend **Mingjuan** in the first English course I took at the university. Mingjuan, I quite enjoy your company and your endless love for me in

these years. I cannot wait to go back to China, settle down, and spend the rest of my life with you!

Last but not the least, everything was possible because of my awesome family. I am very grateful to my mother and father for supporting me to go abroad. This was not an easy decision for my mother. During each video talk that we had, my mother would always say that she regretted that she allowed me to go to a place so far away from her. I am very grateful to my sisters for taking good care of my parents, which made this thesis finally possible.

First draft, 07-02-2021, snow
Den Haag, The Netherlands.

CURRICULUM VITÆ

Jianhuan LIU

11-1990	Born in Jiangxi Province, China.

EDUCATION

2016–2022	Ph.D. in Applied Geophysics Delft University of Technology, Delft, the Netherlands.
2013–2016	M.Sc. in Solid Geophysics University of Chinese Academy of Sciences, Beijing, China.
2009-2013	B.Sc. in Exploration Geophysics Jilin University, Changchun, China.

SCHLORSHIP

2016–2020	China Scholarship Council (CSC) scholarship

MEMBERSHIPS

- European Association of Geoscientists and Engineers (EAGE)
- Society of Exploration Geophysicists (SEG)

LIST OF PUBLICATIONS

ARTICLES

1. **Liu, J**, Draganov, D, and Ghose, R, 2022a, Reducing near-surface artifacts from the crossline direction by full-waveform inversion of interferometric surface waves: In revision, Geophysics.
2. **Liu, J**, Ghose, R, and Draganov, D, 2022b, Characterizing near-surface structures at archaeological site of Ostia based on instantaneous-phase coherency inversion: Geophysics, 87(4), 1–50.
3. Tohti, M, **Liu, J***, Xiao, W, Wang, Y and Di, Q, 2022c, Full-waveform inversion of SH/Love waves based on instantaneous-phase coherency: In revision, Near Surface Geophysics.
4. **Liu, J**, Draganov, D, Ghose, R and Bourgeois, Q, 2021, Near-surface diffractor detection at archaeological sites based on an interferometric workflow: Geophysics, 86(3): WB1–WB11.
5. **Liu, J**, Bourgeois, Q, Ghose, R and Draganov, D, 2019, Detection of near-surface heterogeneities at archaeological sites using seismic diffractions: First Break, 37(9): 93-97.
6. Cheng, F, Draganov, D, Xia, J, Hu, Y, **Liu, J**, 2018, Q-estimation using seismic interferometry from vertical well data: Journal of Applied Geophysics, 159: 16–22.
7. **Liu, J**, Draganov, D and Ghose, R, 2018, Seismic interferometry facilitating the imaging of shallow shear-wave reflections hidden beneath surface waves: Near Surface Geophysics, 16(3): 372–382.

BOOK CHAPTERS

1. Ghose, R, **Liu, J**, Draganov, D, Ngan-Tillard, D, Warnaar, M, *et al.*, 2020, Ultra-shallow shear-wave reflections locating near-surface buried structures in the unexcavated southern Fringe of the ancient Ostia, Rome, *in* H. Kamermans, L. Bouke van der Meer, eds., Designating Place: archaeological perspectives on built environments in Ostia and Pompeii: Archaeological Studies Leiden University (ASLU) 50, 51–62.
2. Ngan-Tillard, D, Draganov, D, Warnaar, M, **Liu, J**, Brackenhoff, J, *et al.*, 2020, Exploring with GPR the frigidarium of the byzantine baths in Ostia Antica after excavation, backfilling and floor re-tiling, *in* H. Kamermans, L. Bouke van der Meer, eds., Designating Place: archaeological perspectives on built environments in Ostia and Pompeii, Archaeological Studies Leiden University (ASLU) 50, 41–50.

CONFERENCE ABSTRACTS

1. **Liu, J**, Bourgeois, Q, Ghose, R and Draganov, D, 2019, Detection of near-surface heterogeneities at archaeological sites using seismic diffractions: 25th European Meeting of Environmental and Engineering Geophysics, EAGE, Den Haag, The Netherlands.
2. **Liu, J**, Ghose, R and Draganov, D, 2018, Seismic interferometry facilitating the imaging of shallow seismic reflectors hidden beneath surface waves: 88th Annual International Meeting, SEG, California, USA.
3. **Liu, J**, Ghose, R and Draganov, D, 2017, Revealing Very Shallow Structures in a Heterogeneous Dyke through Interferometric Subtraction of Surface Waves: 23th European Meeting of Environmental and Engineering Geophysics, EAGE, Malmö, Sweden.